Investigating a spectral approach to understanding wave and sediment dynamics on muddy tidal flats

MSc Thesis

Conor Hunter

TU Delft

MSc Thesis

Investigating a spectral approach to understanding wave and sediment dynamics on muddy tidal flats

by

Conor Hunter

in partial fulfilment of the requirements for the degree of,

Master of Science in Civil Engineering,

at the Delft University of Technology,

to be defended publicly on Friday October 24, 2025 at 13:45 PM.

Student Number:	5133580
Responsible Supervisor:	Dr.ir. B.C. van Prooijen (TU Delft)
Second Supervisor:	Dr. M.F.S. Tissier (TU Delft)
Track:	Hydraulic Engineering
Faculty:	Civil Engineering and Geosciences, TU Delft

Cover: ADV frame on the tidal flat at Gat van Borsele, 15th of May 2025 (Taken by Author).

TU Delft

Preface

Completing this thesis wraps up a diverse and enjoyable academic journey of 6 years at TU Delft. From the very beginning I was eager to learn more about the interface of land and water. Somewhat disappointed by the lack of the latter during the Bachelor, I was saved by the Master's hydraulic engineering track. It was challenging yet inspiring to understand, model and design for our coastlines, estuaries and rivers. Specifically delta's became a subject of passion, which is reflected in this thesis.
It was a great opportunity to conduct field measurements in the Western Scheldt estuary. Seeing these systems in real life and learning how to monitor them was a pleasure which brought much of the theory to life. Preparing all the instruments in the lab was sometimes tedious but always exciting. The practical puzzle of designing and executing a measurement campaign was hands down a highlight of this project, and hopefully something I can do more in the future.

The research itself was rather explorative in nature. As supervisors, *Bram* and *Marion* were open minded and encouraged me to follow my curiosity. At times this was perhaps overwhelming, yet rewarding once I properly framed the investigation. Looking at the effect of waves on tidal flats was a perfect match in their expertise. Our fun discussions directed me amidst a range of topics, eventually landing at spectral analysis and how it can further the understanding of wave-sediment dynamics on tidal flats. The interdisciplinary nature of the project was inspiring and made me aware of its potential in research. Testing and translating methods from other fields to our own can spark novel discoveries. Despite the small steps taken in this thesis, I remain curious to see what the sandy and tidal flat toolboxes will learn from each other in the future.

Hereby I would like to thank *Bram* and *Marion* for their guidance and trust throughout this project; it was a pleasure to work with you. Our conversations gave me fundamental and applied understanding, as well as practical skills to contribute successfully to research in this field. The tidal flats research group was another great source of inspiration and feedback. Dear thanks to *Roy* and *Marthe* for inviting me to your group's helpful discussions.
The fieldwork would have never been possible without the help of *Bram*, *Jennifer*, *Arie*, *Pieter*, *Deepika*, *Jianwei* and *Chantal*. Huge thanks to all of you for your help during the various stages of the field campaign. Thanks to *Roy* for explaining the STMS calibration process, and thank you to *Jennifer* for helping speed up its process despite the many hours it took. Thank you to Marlies for sharing and explaining your valuable code to process the sensor data. Finally I would like to thank *Hein*, my mum and dad (*Michele* and *Martin*), my sister *Niamh*, *de Atlas* and my amazing friends who gave me unwavering energy, love and motivation. It made a huge difference and I am enormously grateful to all of you.

As this chapter ends, another begins. I am glad to be continuing in academia with a PhD at NIOZ in Yerseke. Many thanks to *Roy* for bringing this interesting opportunity to my attention. Diving deeper into tidal flats, the lessons learnt during this thesis have been a great preparation for the next adventure. To wrap up, here are a number of personal lessons which will bring me further, in no particular order:

1. Measure twice, cut once: Program your sensors carefully before deployment.
2. Value good datasets, especially when taken in the field.
3. Acknowledge being a time optimist. Plan accordingly.
4. Write everything down. Do so sooner rather than later.

Conor Hunter
October 2025

Abstract

Tidal flats are complex coastal environments where tides, waves, and sediment dynamics interact to shape morphology and sustain ecological functions. Understanding these interactions is essential for managing estuarine systems such as the Western Scheldt, where port activities, sea level rise, flood protection and ecological conservation increasingly compete for space. Although previous studies have highlighted the importance of waves in mobilising fine sediments, many have relied on monochromatic representations of wave fields. These approaches reduce irregular wave fields to a single characteristic height and period, which conceals the influence of long waves and multi-modal spectra. This thesis reviews the potential of a spectral approach to improve the understanding of wave and sediment dynamics on muddy tidal flats by explicitly considering the full wave spectrum and its cross-shore transformation.

The research investigates whether a spectral approach can provide a better interpretation of wave-driven sediment dynamics than a monochromatic description. Field measurements were conducted on the Gat van Borsele tidal flat in the Western Scheldt during a month-long campaign in spring 2025. Three instrument frames were deployed along a cross-shore transect, each equipped with acoustic Doppler velocimeters (ADV), suspended sediment sensors (STMS), and pressure sensors. These instruments recorded 3D velocities, suspended sediment concentrations (SSC), and surface elevations to capture the evolution of both short and long wave components under varying water levels, tidal currents, and wind forcing. The resulting dataset allowed the construction of wave spectra and the analysis of corresponding near-bed orbital velocities, bed shear stresses, and sediment responses.

Short waves, defined within frequencies $f = [0.1 - 1.5]Hz$, were found to dominate surface elevation variance and to behave largely linearly, confirming that local wind-generated waves account for most of the tidal flat's wave energy. The mild wind conditions were unable to generate depth-limited waves which are typically identified on tidal flats. Instead the effect of wind direction and fetch was clearly observed, where more onshore winds drove larger short waves. Long waves, defined as $f = [0.003 - 0.1]Hz$, were generally less energetic but contributed a significant portion of near-bed velocity variance, particularly at large water depths which attenuate short wave velocities. Large long waves could also be identified which originated outside of the local wave field. These are suspected to be formed by seiches or container vessels passing through the navigation channel. These more pronounced long waves reached orbital velocities similar to the short wave field, highlighting their capacity to influence sediment dynamics.

The SSC analysis revealed strongest responses to wave forcing within shallow water. Suspended sediment concentrations did not respond strongly to changes in wave driven bed shear stress. Instead, peaks in SSC were observed within a suspected turbid fringe which travelled up and down the tidal flat within shallow water between the middle and low measurement frames. At the high measurement frame, SSC had minimal response which contradicted the largest wave driven bed shear stresses at that location. Observing time series of SSC and long wave velocities reveals fluctuations of SSC similar to the long wave time scale. Yet this would require a co-spectral analysis to be confirmed.

The study concludes that a spectral approach enhances understanding of wave and sediment dynamics on muddy tidal flats by distinguishing between short and long wave processes that would otherwise be obscured. Under calm wave climates such as those observed during the measurement period, a monochromatic approach remains adequate. However, during more energetic events or at sites influenced by seiches, vessel traffic, or infra-gravity waves, the spectral approach holds great potential to correctly interpret cross-shore sediment transport by waves. Future research should therefore target more exposed or navigationally influenced flats to capture the full variability of wave-driven processes. Here it is critical to measure for a sufficient burst duration as to fully capture the potential long waves. By applying spectral analyses in such settings, this work contributes to a more complete understanding of estuarine morphodynamics and supports sustainable management of tidal flat systems.

Contents

1

Introduction

Aerial photograph of the Western Scheldt navigation channel, surrounded by emerging tidal flats (de Vet, 2020).

1.1. Research Context

According to Amos (1995) and Friedrichs (2011), tidal flats can be defined as ”low bed slope environments, consisting of sediments in the absence of abundant tidal marsh or mangroves, and which are exposed subaerially between lowest and highest astronomical tide”. Tidal flats are valuable systems which are shaped by a unique set of ecological, hydrodynamic and morphodynamic processes. Each are interlinked, whilst also increasingly being forced by natural and anthropogenic perturbations, such as sea level rise and human interventions. The Western Scheldt is a prime example of this, as it is a highly engineered estuary due to its maritime stakeholders and strict flood safety requirements (de Vet, 2020). The combination of rising sea levels, channel dredging and engineered flood defences pressures tidal flats, threatening them with coastal squeeze, increased tidal ranges and drowning. Meanwhile its tidal flats are protected nature reserves that are part of flightpaths for a myriad of migratory birds (Mu & Wilcove, 2020). The tidal flats are rich in benthic communities, and can be fringed by

vegetated salt marshes that provide various ecosystem services (Herman et al., 2001).
Natural and anthropogenic effects have large consequences for the tidal flat ecosystem through biogeomorphic feedbacks. Changes in tidal flat morphology affect the prevalence of plant communities across salt marshes in the Western Scheldt. (Feng et al., 2025). Historical data also suggests that these feedbacks can induce sudden shifts between salt marsh and bare flat states, with drastic consequences for the ecosystem and its management (Wang & Temmerman, 2013).

To steward these complex systems into a sustainable future, it is critical to obtain proper understanding of the interactions between hydro- and morphodynamics. Knowledge of these interactions can drive the development of effective management strategies whilst improving theoretical understanding. Tides, local waves and winds force tidal flats under varying conditions, each inducing a response in morphological development. The bathymetry of the tidal flat in turn impacts the incoming hydrodynamic forcing. The resulting interplay results in complex behaviour that is highly variable in space and time.

1.2. Research Problem

The Western Scheldt estuary, like many meso and macro tidal systems, is forced by dominating tidal currents flowing through meandering flood and ebb channels. However across tidal flats, where water depths and currents are smaller, wave induced forcing becomes more relevant. The impact of local waves is generally said to drive an offshore transport, eroding tidal flats and leading to a more concave profile (Friedrichs, 2011; Green & Coco, 2014; Le Hir et al., 2000). Transport by local waves is influenced by an interplay between fetch, flat bathymetry and tidal water levels due to their combined effect on orbital velocities and bed shear stresses. When orbital velocities reach the bed, shear stresses are generated and sediment is suspended in the water column, leading to transport (Green & Coco, 2014). Across tidal flats, these wave-induced bed shear stresses have been found to contribute significantly to the hydrodynamic forcing of the bed (Green, 2011; Green et al., 1997).

When considering the effect of waves on tidal flats, or on any shoreline, it is important to understand the variety of waves that exist . Figure 1.1 illustrates the range of possible waves according to their period or wave length (Holthuijsen, 2007). Wind generated waves are the most common and well studied waves which reach our shorelines. Commonly characterized by periods of $T = 0.25 - 30\ s$, their orbital velocities drive cross-shore sediment transport which continuously shapes the shore face.

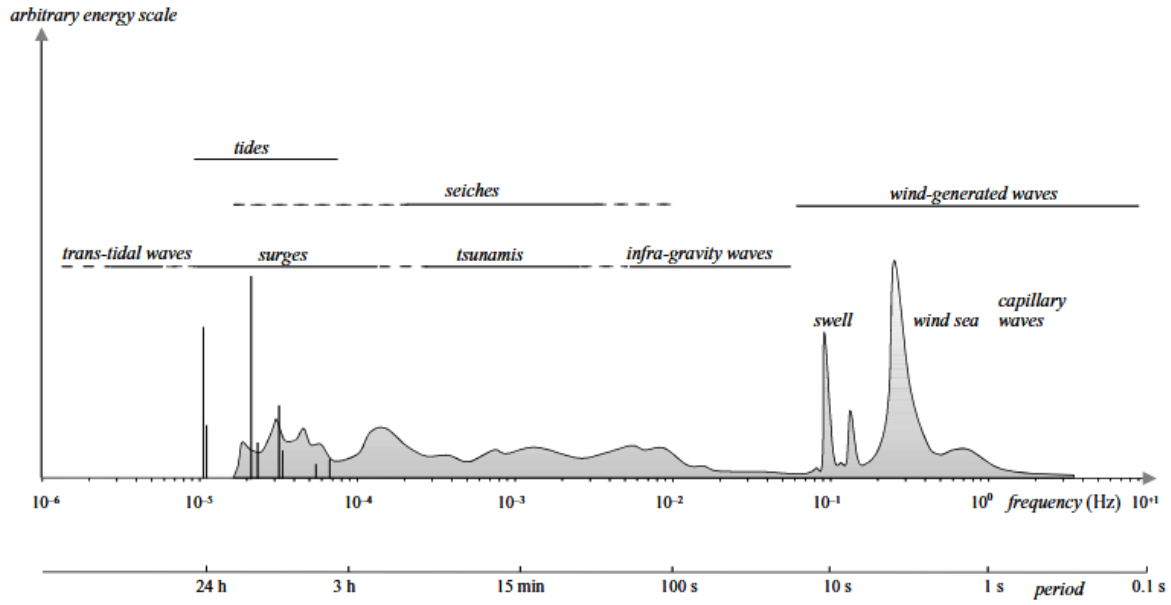

Figure 1.1: Types of surface waves and their energy, organised by frequency and period (Holthuijsen, 2007)

Longer waves can however also contribute to cross-shore sediment transport. Infra-gravity waves ($T = 20 - 200s$) have been extensively studied on sandy coastlines. Generated by non-linear energy

transfers of the sea-swell waves ($T = 2 - 20s$), they can generate significant near bed velocities and transport large portions of the cross-shore sediment flux (de Bakker et al., 2016). Infra-gravity waves are less prevalent in estuaries, however seiches (Seo et al., 2024) and vessel waves (Schoellhamer, 1996) are both examples of long waves which can drive sediment suspension and transport in estuaries.

Despite this range in frequencies within the wave field, many studies opt to use a monochromatic approach when describing waves on tidal flats. Measured irregular wave fields are reduced to a single characteristic wave, represented by a significant wave height H_s and peak period T_p (or mean period T_{m02}, T_{m01}). This masks the presence of long waves, as well as any bimodal nature of the wave field. In sandy systems this is often unacceptable, as many coasts experience bimodal sea states with distinct swell ($T = 2 - 20s$) and wind waves ($T = 0.5 - 5s$) reaching the shore. For tidal flats however, a monochromatic description can be acceptable. Their often sheltered nature makes it rare for sea swell waves to reach them. Local wind waves are therefore most common, resulting in a unimodal state which can accurately be reduced to a single characteristic wave.

The monochromatic approach breaks down for wave fields with significant long wave energy. In these cases, the unique frequencies of infra-gravity waves, seiches and vessel waves are not properly considered alongside the local wind waves. This limits the description of wave dynamics across tidal flats, in turn limiting the understanding of wave driven sediment transport and eventual tidal flat morphology. Figure 1.2 provides a simplified schematic, highlighting in what situations a monochromatic approach is suitable. Finally, bi- or multi-modality can also apply to the directional wave field. Waves and transport stemming from distinct directions will also be misinterpreted using a monochromatic definition.

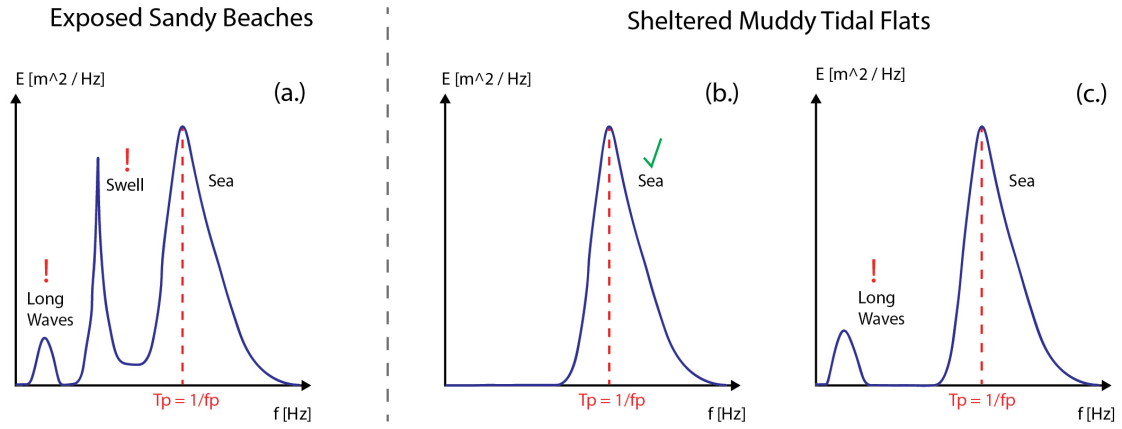

Figure 1.2: Simplified schematic of wave fields and the suitability of a monochromatic approach. Panel (a.): Monochromatic descriptions fail to capture the multi-modality of the wave spectra at exposed sandy beaches. Panels (b.) and (c.): Monochromatic descriptions can be suitable on muddy tidal flats, as long as the wave field only consists of local wind sea. If long waves are present, these will not be captured accurately.

1.3. Research Objective and Research Questions

Sandy environments frequently consider distinct frequency bands to account for incoming wind, swell and long wave components. By considering the transformation of these frequency components in the wave field it is possible to determine how these waves force the bed. The resulting cross-shore transport is highly complex, however various methods have been developed in attempt to describe it. The analytical approach by Bowen (1980) is a prime early example which is still used today (Tas et al., 2020). His formulation considers the effect of on- and offshore transport terms across the wave spectrum by decomposing the velocity signal into a mean flow, short wave motion and long wave motion. Field approaches are also used by considering the co-spectra of measured velocities and suspended sediment concentrations (de Bakker et al., 2016). This uncovers which frequencies in the wave field lead to sediment suspension, also giving insights into the direction of the resulting flux.

Defining a spectral approach for understanding tidal flat wave and sediment dynamics

Taking inspiration from the methods common in sandy systems, a **spectral approach** is proposed in this study to understand tidal flat wave and sediment dynamics. In the context of this research, a spectral approach refers to the consideration of the full wave spectrum and its effect on sediment dynamics. Instead of reducing the measured wave field to a single characteristic wave, the spectral approach considers the transformation of distinct short and long wave frequencies across the tidal flat.

Research Objective

This thesis strives to further the understanding of wave dynamics across tidal flat bathymetries. Advancing monochromatic descriptions often used in past studies, the proposed spectral approach considers transformations of the full wave spectrum. As waves transform, so do their orbital velocities. By comparing the range of orbital motions to observed fluctuations in sediment concentrations, this study attempts to interpret the effect of the full wave field on tidal flat cross-shore sediment transport.

Research Questions

It is critical to assess whether the proposed spectral approach actually improves understanding of wave and sediment dynamics. Considering its important role in sandy environments, as well as the range of long waves which can occur in estuaries, this this thesis hypothesises that a spectral approach can lead to more detailed understanding. However, there are cases in which a monochromatic definition is satisfactory. Therefore, this thesis attempts to answer the following research question:

Research Question

Can a spectral approach provide a better interpretation of wave driven sediment dynamics on muddy tidal flats?

To properly investigate the interplay between wave and sediment dynamics on muddy tidal flats, the following two sub questions were drafted. These explore wave transformations in detail through a spectral approach, coupling this to wave orbital velocities, bed shear stresses and suspended sediment concentrations (SSC). Answering these questions will help understand how wave dynamics, sediment transport and morphology interact across spectral components, highlighting how this interaction develops along the cross shore.

Sub Question 1

How do wave transformations take place across spectral components in the wave field on a muddy tidal flat under varying water levels, tidal currents and wind forcing?

Sub Question 2

How do the different spectral components present in the wave field contribute to the near bed orbital velocities and bed shear stresses, and how do these suspend sediments?

1.4. Research Scope

The higher aim of this research is to contribute to the understanding of wave driven morphodynamics on tidal flats. Ultimately this can help improve management strategies and the sustainable stewardship of tidal flat ecosystems amidst natural and anthropogenic perturbations. Despite this, the study is limited by not considering the often annual timescales at which morphodynamic feedbacks take place

(Friedrichs, 2011). Instead an attempt is made to broaden the understanding of wave and sediment dynamics through a month long field campaign. The campaign considers how wave dynamics are affected by current morphology, and how these waves suspend and transport sediment during the measurement period.

There are many forms of tidal systems and tidal flats. Each is characterized by a unique collection of tidal, wave and wind forcing that drives patterns of sediment transport. Furthermore, they exhibit unique sediment compositions and have varying vegetation and benthos that alter the bed properties. This study considers the interplay between wave dynamics and tidal flat morphology along a bare and muddy tidal flat in the macro-tidal Western Scheldt estuary (see figure 1.3). The research focusses on this interaction for a single cross-shore transect, ignoring the effects of larger creek-flat morphology. The study has been conducted through the use of field measurements, taken at the Gat van Borsele tidal flat during a period of one month in the spring of 2025.

1.5. Structure

This thesis is structured as follows. Chapter 2 introduces the Western Scheldt as field site and presents the required theoretical background to understand wave and sediment dynamics on its tidal flats. Chapter 3 presents the applied method, starting with the field campaign and following with the approach to answering each sub question. Chapters 4 and 5 illustrate the results from sub questions 1 and 2 respectively. Chapter 6 contains the discussion and finally chapter 7 states the conclusion.

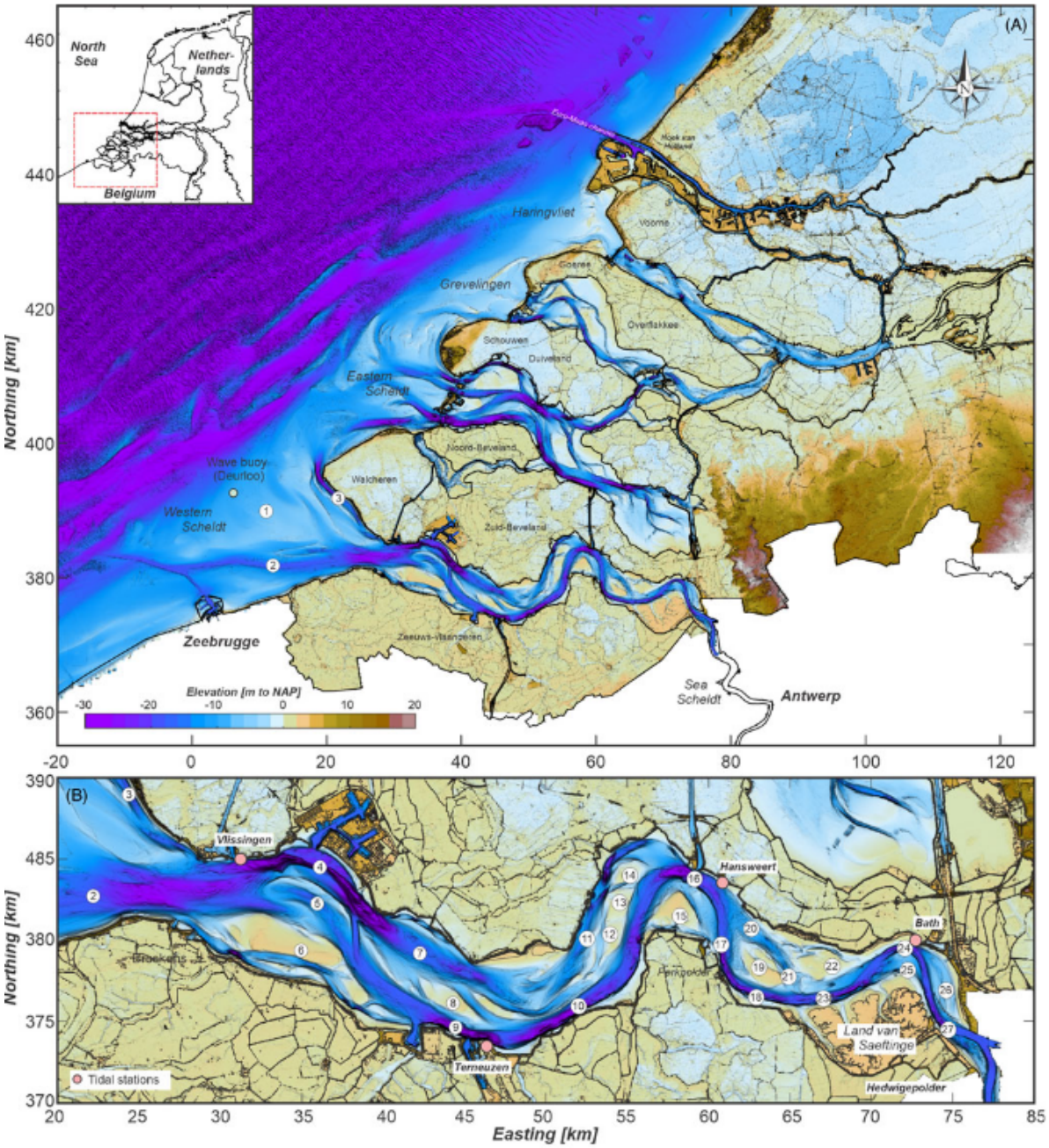

1. Vlakte van de Raan	6. Hooge Platen	12. Rug van Baarland	17. Zuidergat	23. Overloop van Valkenisse
2. Wielingen	7. Everingen	13. Plaat van Ossenisse West	18. Bocht v. Walsoorden	24. Nauw van Bath
3. Oostgat	8. Middelplaat	14. Molenplaat	19. Plaat van Walsoorden	25. Plaat van Saeftinge
4. Honte	9. Pas van Terneuzen	15. Plaat van Ossenisse	20. Schaar van Waarde	26. Ballastplaat
5. Spijkerplaat	10. Gat van Ossenisse	16. Put van Hansweert	21. Schaar van Valkenisse	27. Pas van Rilland
	11. Middelgat		22. Platen van Valkenisse	

Figure 1.3: Panel A: Overview of the (former) estuaries in the south west delta of the Netherlands. Bathymetry (taken in 2021) is given in meters with respect to NAP. The Western Scheldt estuary is the last remaining open estuary in the Netherlands. Panel B: Detailed map of the Western Scheldt, with highlighted tidal stations, tidal flats and shoals. (Elias et al., 2023)

2

Theoretical Background

Aerial photograph of the Zuidgors tidal flat during low tide in the Western Scheldt estuary (de Vet, 2020).

This chapter first introduces the Western Scheldt as study site, presenting the typical tides, waves, winds and sediment which characterize it. Then considering the tidal flats present in the estuary, important connections are presented between wave dynamics, sediment transport and tidal flat morphodynamics. These elaborate how waves transform across tidal flats, how waves suspend and transport sediment on tidal flats, and finally how this in turn shapes tidal flat morphologies. The literature review ends with the identified research gap that this study attempts to address.

2.1. The Western Scheldt Estuary

The Western Scheldt is a tidal estuary which connects the Scheldt river to the North Sea. The system is the only open estuary left in the Netherlands, exhibiting a unique landscape of dynamic tidal shoals, mud flats and salt marshes. These habitats are characterized by tidal cycles of emergence and submergence, relatively small waves, brackish waters and fine sediments. The flat ecosystem is home to rich communities of benthos, and are important for the flight paths of migratory birds (Mu & Wilcove, 2020).

The estuary exhibits a multichannel system of braiding ebb and flood channels. The flood channels are relatively straight and shallow, whilst the ebb channels are often deeper and meandering. The latter also constitute an important shipping route, connecting the ports of Gent, Terneuzen, Vlissingen and Antwerp (Swinkels et al., 2009). The meandering ebb channels are routinely deepened and dredged to accommodate the ever growing flux of vessels. Dredged sediments are then distributed over tidal flats and shoals, as well as non-navigation channels (de Vet, 2020). Due to its connection to the North Sea, the banks of the estuary are highly engineered with levees and other flood defence structures. Figure 2.1 gives an overview of the Western Scheldt bathymetry and the engineered navigation channel. The

figure clearly shows the deep meandering channels, with the shallow intertidal areas consisting of shoals and fringing mudflats. A number of them have been marked for future reference, as previous campaigns have found useful results for interpreting conditions on tidal flats in the Western Scheldt.

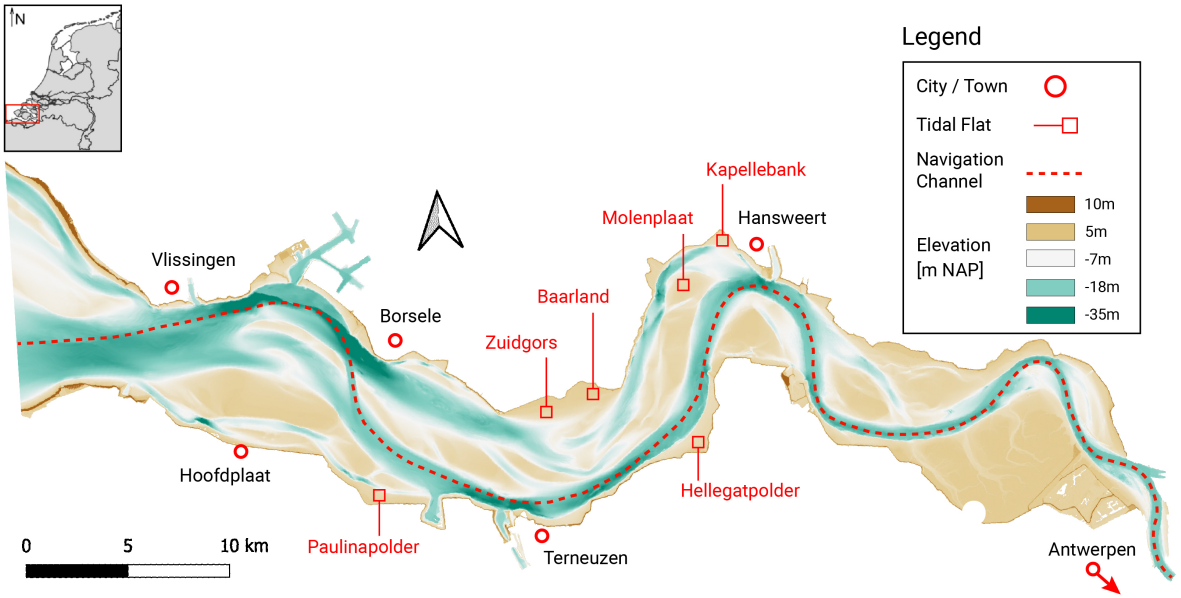

Figure 2.1: Overview of the Western Scheldt bathymetry with relevant places, intertidal areas and the navigation channel marked in red. Bathymetry data (20m x 20m grid; Measured in 2022) taken from Rijkswaterstaat (2025); navigation channel taken from de Vet (2020).

2.1.1. Tides and Currents

The Western Scheldt is a meso to macro tidal system. It has a tidal range of nearly 4 meters at the estuary mouth, increasing to around 5 meters at the port of Antwerp. The tides are semi-diurnal, generally exhibiting two high and two low tides per day. Tidal currents are largest in the deeper ebb and flood channels, reaching up to 1.8 m/s. These magnitudes reduce significantly across the shallow shoals and tidal flats. Figure 2.2 by Leuven et al. (2018) gives an overview of the peak current velocities in the Western Scheldt.

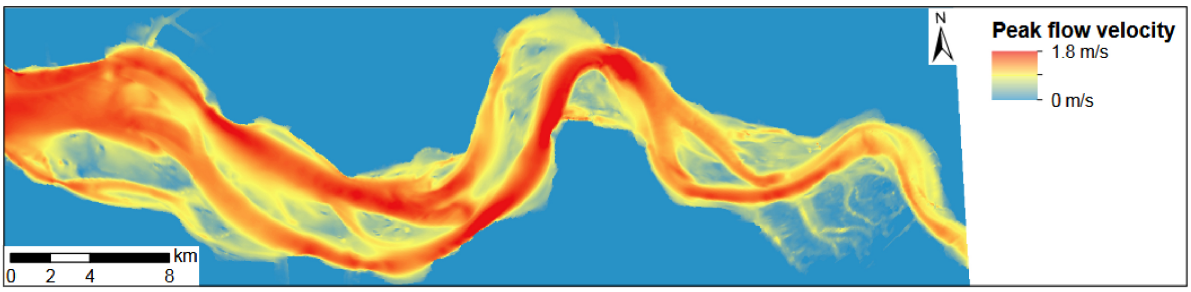

Figure 2.2: Map of peak flow velocities in the Western Scheldt [m/s] Taken from Leuven et al. (2018), who used the SCALWEST hydrodynamic model of Rijkswaterstaat with 2009 bathymetry.

Considering flood and ebb currents seperately, NeVla model results by Van Dijk et al. (2019) provide additional context. These highlight the ebb dominance of the deeper channels. Meanwhile the higher and flatter inter-tidal areas were found to be typically flood dominant.

The system as a whole is tidally dominated due to the lack of large waves and consistently small river discharge. Tides are therefore also the main contributor to the sediment supply in the estuary (Callaghan et al., 2010). Unlike riverine contributions, tidal sediment supply is not seasonal. Therefore there is little to no seasonal variability in sediment supply to the estuary.

2.1.2. Sediment and Ecotopes

The Western Scheldt has a highly heterogeneous distribution of bed material which is related to the various hydrodynamic regimes present in the estuary. Coarser sandy material is found in the more energetic deeper channels, whilst fine cohesive sediments are present on the sheltered and shallow tidal flats. Figure 2.3 shows the (top layer) bed composition mapped by Elias et al. (2023), showing the percentage sand concentration of this layer throughout the estuary. While the deeper channels approximately contain 80-100% sand, the northern intertidal areas mostly have fractions between 60-80% (Elias et al., 2023).

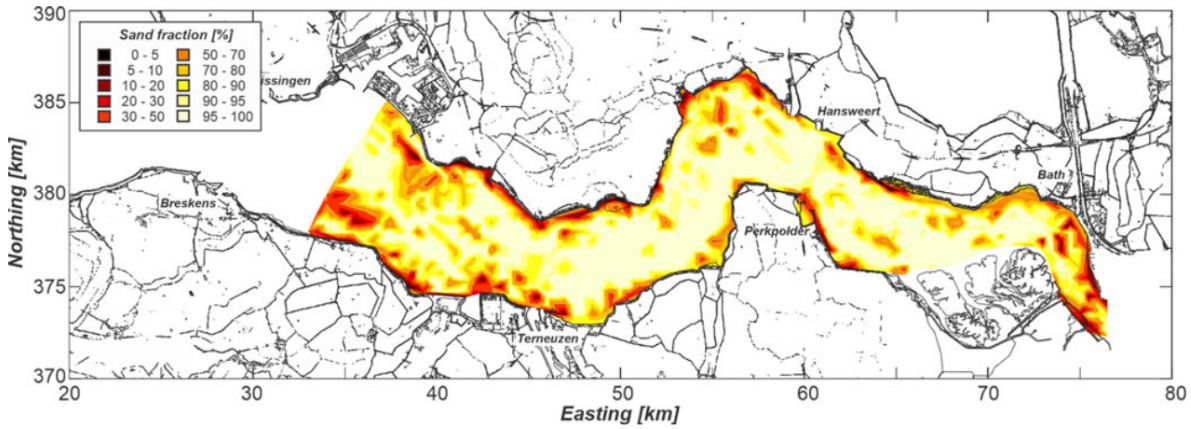

Figure 2.3: Map of percentage sand fraction for the top bed layer in the Western Scheldt (Elias et al., 2023).

The composition of biotic (benthos, vegetation) and abiotic (sediment, hydro- and morphodynamic) conditions defines a range of distinct ecoptopes across the inter-tidal areas of the estuary. These are presented in figure 2.4 and distinguished based upon sediment, vegetation and morphodynamic conditions (Leuven et al., 2018). The low dynamic muddy zones in red are of interest to this study. These represent (bare) muddy tidal flats and shoals.

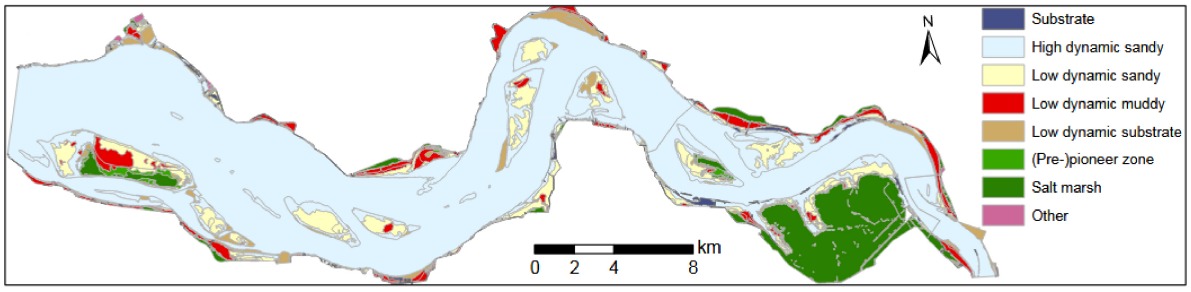

Figure 2.4: Intertidal ecotopes in the Western Scheldt. The analysis presents distinct categories of tidal flats, shoals and salt marshes depending on their environmental conditions (Leuven et al., 2018).

Samples from Herman et al. (2001) on the Molenplaat shoal found median sediment grain sizes ranging between $77\mu m$ and $174\mu m$. The samples contained significant quantities of mud ($< 63\mu m$), ranging from 4-43%. Other samples, taken by Callaghan et al. (2010) on four tidal flats, found median sediment grain diameters of $77\mu m$ at Zuidgors, $57\mu m$ at Baarland, $97\mu m$ at Paulinapolder and $135\mu m$ at Hellegatpolder.

Median grain sizes give a quick and easy indication of the sediment present on muddy tidal flats. Despite this, it is important to consider the heterogeneity of bed material compositions. The morphology of estuarine systems is influenced though bimodal sediment distributions with distinct yet interacting sand and mud regimes (Colina Alonso, 2024; van Ledden, 2003). Furthermore, these low energy and intertidal areas house a variety of benthic communities which can have unique effects on sediment erodibility (Herman et al., 2001).

2.2. Tidal Flats in the Western Scheldt

As shown in figure 2.4, there are a wide range of muddy tidal flats in the Western Scheldt. The majority of these are tidal-dominant, exhibiting convexly shaped profiles that are steadily growing over time (de Vet, 2020; Hanssen et al., 2024; Maan et al., 2018). The flats are fronted by a steep slope towards the tidal channel, which is formed by the strong alongshore tidal current (Hanssen et al., 2024; Maan et al., 2018). This front ends around the MLW line, where the tidal flat begins. From here the alongshore flow reduces in magnitude, and cross-shore currents and waves start to force the bathymetry. Figure 2.5 gives a schematic overview of a typical tidal flat in the Western Scheldt fringed by a salt marsh.
This profile has however not always been typical. Over time, the tidal flats in the Western Scheldt have grown and become steeper. Analysis by de Vet (2020) in figure 2.6 illustrates this development for the Zuidgors tidal flat between 1992 and 2017. The convex-up development and steep ridge formation confirms tidal dominance in the estuary.

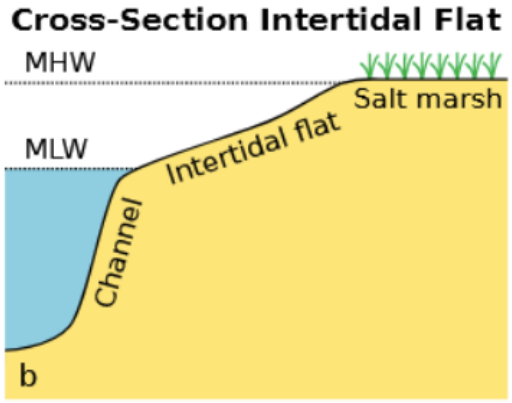

Figure 2.5: Sketch of a typical tidal flat cross section in the Western Scheldt. Starting most offshore with a deep sub-tidal channel with a steep slope, followed by an intertidal mudflat with a mild slope, finally fringed by a salt marsh (de Vet, 2020).

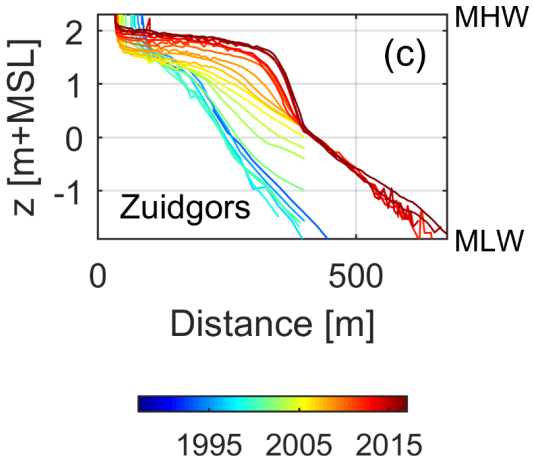

Figure 2.6: Cross shore elevation transects on the Zuidgors tidal flat constructed using data from 1992 to 2017 (de Vet, 2020).

2.2.1. Tidal Flat Morphodynamics

Observing the typical profile and development of tidal flats in the Western Scheldt, it is important to understand the physical processes that shape them. The morphology of tidal flats can be described by the profile shape, bed slope and sediment composition. These characteristics are a function of external forcing by local waves, tides and sediment supply. The hydrodynamic forcing is in turn a function of morphology, creating a morphodynamic feedback loop. Figure 2.7 illustrates this interaction in a schematic flowchart by Friedrichs (2011).
Tidal flats can exhibit varying morphologies depending on the hydrodynamic climate and sediment composition. Exposed flats are characterized by a high energy environment, forming steeper slopes with a relatively large sand content. Sheltered flats are often low energy environments with few waves but the presence of tides. This favours the deposition of muddy sediments and the formation of flat slopes. Figure 2.8 illustrates this rule of thumb for exposed and sheltered flats (Friedrichs, 2011).
Tidal flats in the Western Scheldt are commonly characterised by a mild slope and muddy sediments as in the sheltered typology. Despite this, many are bordered by a steep subtidal channel, which may be more alike the exposed typology. In reality there are many unique configurations, always consisting of wave and tidal energy together with a mixture of both sandy and muddy sediments.

When considering the development of tidal flats over a typical annual cycle, there are distinct seasonal regimes. Summer periods commonly accrete the flat with consistent flood dominant tides. Meanwhile the winter period is characterised by frequent storms with erosive waves (Friedrichs, 2011). Although debated in current research, the concept of a dynamic equilibrium is often presented. This is used to describe the cyclical feedback between morphology and hydrodynamic forcing, ultimately maintaining an oscillating yet stable state (Friedrichs, 2011).

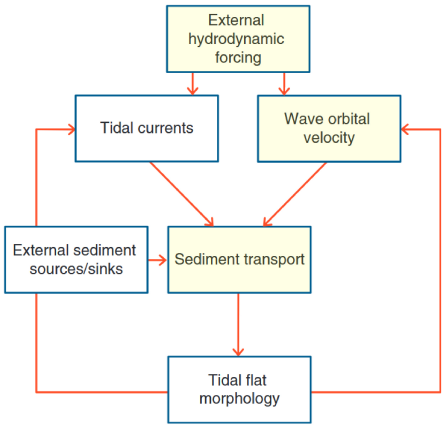

Figure 2.7: Schematic overview of the tidal flat morphological feedback loop. Panels highlighted in yellow are explicitly considered in this thesis. (Friedrichs, 2011).

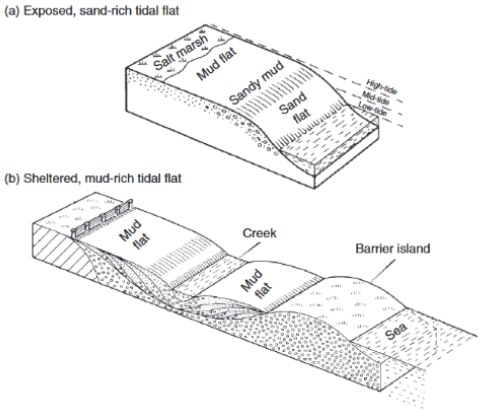

Figure 2.8: Overview of exposed and sheltered tidal flat typologies (Friedrichs, 2011).

Scoping the morphodynamic feedback loop

In the context of this study, the full morphodynamic feedback loop is not considered. The annual timescales at which it takes place are outside of the research scope. Instead this thesis examines the effect of the entire wave field (External hydrodynamic forcing) on tidal flats. Looking at how waves generate orbital velocities and how these relate to sediment suspension and transport. The effect of tidal currents on sediment transport is not directly considered. However, the study does investigate the effect of tidal currents and water depth on wave transformations.

2.2.2. Tidal Currents on Tidal Flats

Tides can suspend sediments with the shear stress of their current on the bed, as well as transport them across the flat. Generally speaking, tidal currents are said to accrete the tidal flat due to a range of barotropic mechanisms (Friedrichs, 2011; Green & Coco, 2014; Le Hir et al., 2000). Since tidal currents are oscillatory in nature, Lagrangian and Eulerian asymmetries are what drive net sediment transport. In the case of tidal flats this is often onshore directed, leading to the accretion of sediments on the flat during constant tidal cycles.

The classification by Gatto et al. (2017) groups these processes into a velocity asymmetry, temporal lag and spatial lag. The first is created by a residual velocity and differences in peak flood and ebb magnitudes, where tidal flats are inherently flood-dominant due to their bathymetry. Temporal lags describe the delayed response in suspended sediment concentration to varying flow velocities. Longer flood slack-water allows more sediments to settle on the flat despite the lags in sediment response to forcing. Finally, spatial lags describe the impact of cross-shore variations in bed level, water depth and velocities. Since bed levels increase, water levels and velocities decrease resulting in a landward transport.

Various studies have collected tidal flow velocities on tidal flats in the Western Scheldt. Observations by de Vet (2020) in figure 2.9 from the winter of 2016 at Zuidgors confirm flood dominant velocities near the low water line, with peaks ranging between 0.5 and 1.5 m/s. Meanwhile ebb velocities remain highly constant and are smaller at 0.5 m/s.

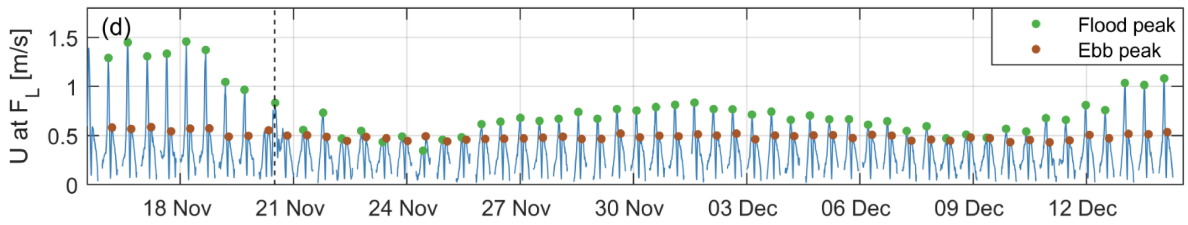

Figure 2.9: Measured tidal current velocities during November and December of 2016. Taken near mean low water on the Zuidgors tidal flat (de Vet, 2020).

2.2.3. Local Wind Waves on Tidal Flats

Although tidal influence dominates many aspects of the estuary, locally generated wind waves play an important role. In shallow areas where tidal currents are smaller, wave induced forcing becomes more significant (Friedrichs, 2011). This is true for many of the tidal flats and shoals within the Western Scheldt where water depths are shallow and alongshore tidal currents are attenuated.
Contrary to tides, waves erode tidal flats by suspending sediments with their generated orbital velocities (Friedrichs, 2011; Green & Coco, 2014; Green et al., 1997; Le Hir et al., 2000). The seaward transport of sediment by waves is commonly (yet only partially) explained by considering how waves keep sediments in suspension, obstructing the settling process. Ultimately this blocks the onshore transport from tidal asymmetries (temporal lags in particular) and tends to induces net offshore transport (Green & Coco, 2014).

Most tidal flats are subjected to episodes of local waves generated by the wind, which are a fraction in height of the tidal range. Depending on the fetch and wind speed, these waves usually have periods ranging between $T = 0.5 - 5s$ (Green & Coco, 2014). The duration of the wind is often not a limiting factor, as estuarine fetches ($\approx 1km$) are small enough for waves to fully develop in short timespans. Typically, wave heights are seen to increase with the square root of the fetch length under a given wind speed. Whereas for a fixed fetch length, wave heights increase linearly with wind speed (Le Hir et al., 2000).
The Western Scheldt is characterized by a predominantly south western wind. This generally makes the northern banks of the estuary most exposed to wind and thus waves. Figure 2.10 by Callaghan et al. (2010) shows the wind climate for stations at Hoofdplaat, Terneuzen and Hansweert from 1987 till 2008 using KNMI data. The typical wind speeds range from 5 to 8 m/s, yet extremes can be crucial. During the erosive 2016 winter storm measured by de Vet (2020), hourly mean wind speeds reached up to 22 m/s.

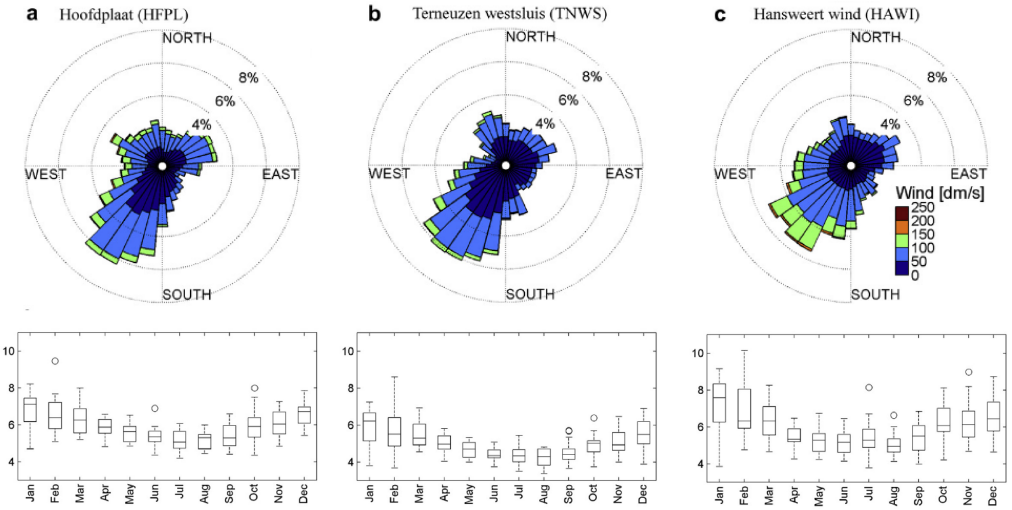

Figure 2.10: Wind roses and monthly bar plots using KNMI data from 1987 to 2008 at Hoofdplaat, Terneuzen and Hansweert. Adapted from Callaghan et al. (2010).

Figure 2.11 shows the associated wave heights during the storm measured by de Vet (2020). The campaign found small waves with significant wave heights mostly between $H_s = 0.05 - 0.20$ meters near the mean low water line of the Zuidgors tidal flat. Yet during the climax of the storm, the large wind speeds ($22m/s$) generated wave heights of $H_s = 0.6$ [m]. These were accompanied by a 20cm drop in bed level which highlights the erosive impact of waves during storm events.
An earlier field campaign on the bare flat at Zuidgors from Callaghan et al. (2010) found mean significant wave heights of $\overline{H_s} = 0.14m$ during calm conditions ($u_{wind} < 7m/s$), and $\overline{H_s} = 0.23m$ during windy conditions ($u_{wind} > 7m/s$). The waves during calm and windy conditions were both found to generate larger time averaged bed shear stresses ($\overline{\tau}_w$) compared to currents ($\overline{\tau}_c$). Despite their small magnitude, the study showcases how waves can dominate bed forcing and thus sediment suspension on tidal flats in the Western Scheldt.

Field campaigns in other estuaries have found complementary results. In the Tamaki estuary in New Zealand, Green (2011) found that waves as small as $H < 0.20m$ (with periods of $T = 1.0 - 1.8s$) were able to effectively suspend fine sediments across a muddy tidal flat. The additional shear stress generated by wave orbital velocities can amplify the existing stress from currents. Measurements taken on the Wiroa island mudflat (New Zealand) even found that the additional stress from waves was critical in suspending sediments otherwise not entrained by solely tidal currents (Green et al., 1997).

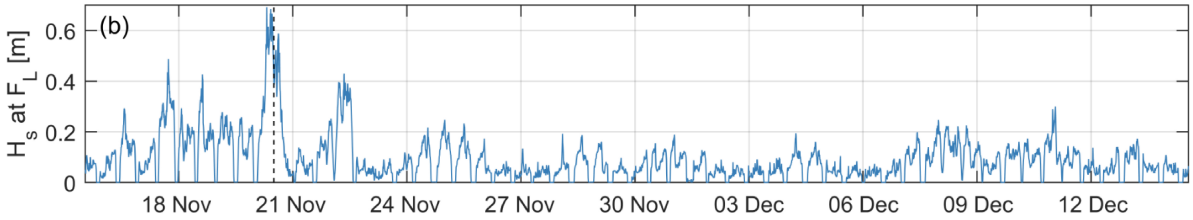

Figure 2.11: Measured significant wave heights during November and December of 2016. Taken near mean low water on the Zuidgors tidal flat (de Vet, 2020).

2.2.4. Effect of Tides and Waves on Tidal Flat Profiles

Figure 2.12 by Colina Alonso (2024) provides a visual reference illustrating various processes driven by tidal currents and wave orbital velocities on tidal flat environments. Shear stresses from wave orbital motions and tidal currents suspend sediments, and can drive both bed and suspended sediment transport which can lead to erosion. The successful settling of sediments leads to accretion and growth of the tidal flat profile. Although biotic processes and sand-mud interactions can contribute significantly to the sediment dynamics on tidal flats, these will not be assessed in detail in this thesis.

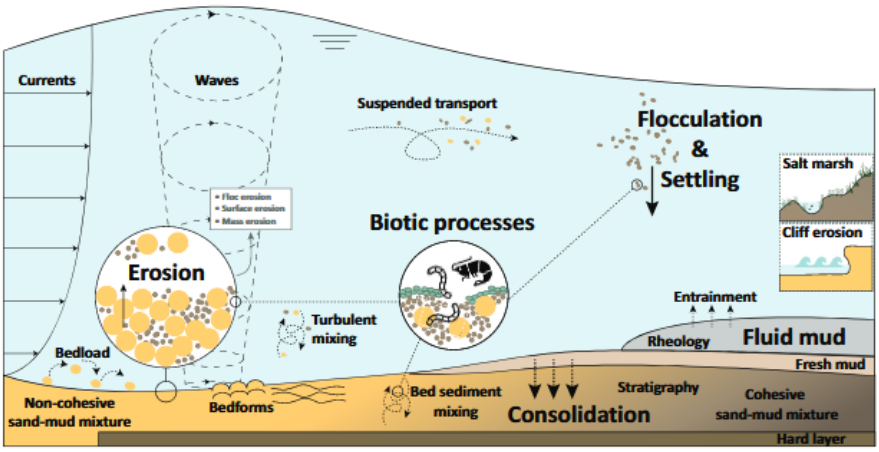

Figure 2.12: Visual summary of current, wave and sediment dynamic processes that can occur on tidal flats (Colina Alonso, 2024).

Generally speaking, tidal currents generate onshore transport through time lags and a flood velocity asymmetry which accretes tidal flats. As shown in panel (b) of figure 2.13, tidal currents reduce in magnitude as water depths decrease. This Lagrangian asymmetry leads to onshore sediment transport.
Waves do not advect sediments directly, yet their orbital velocities do (re)suspend them and obstruct the settling process. Orbital velocities reach the bed more effectively at smaller water depths. Assuming a fixed wave height across the entire flat, panel (c) describes an offshore transport of sediments due to the cross-shore gradient in wave orbital velocities.
This assumption however ignores the effect of shoaling, frictional dissipation, fetch variations and other cross-shore wave dynamics which may significantly impact the magnitude of wave orbital velocities and thus sediment transport across a tidal flat.

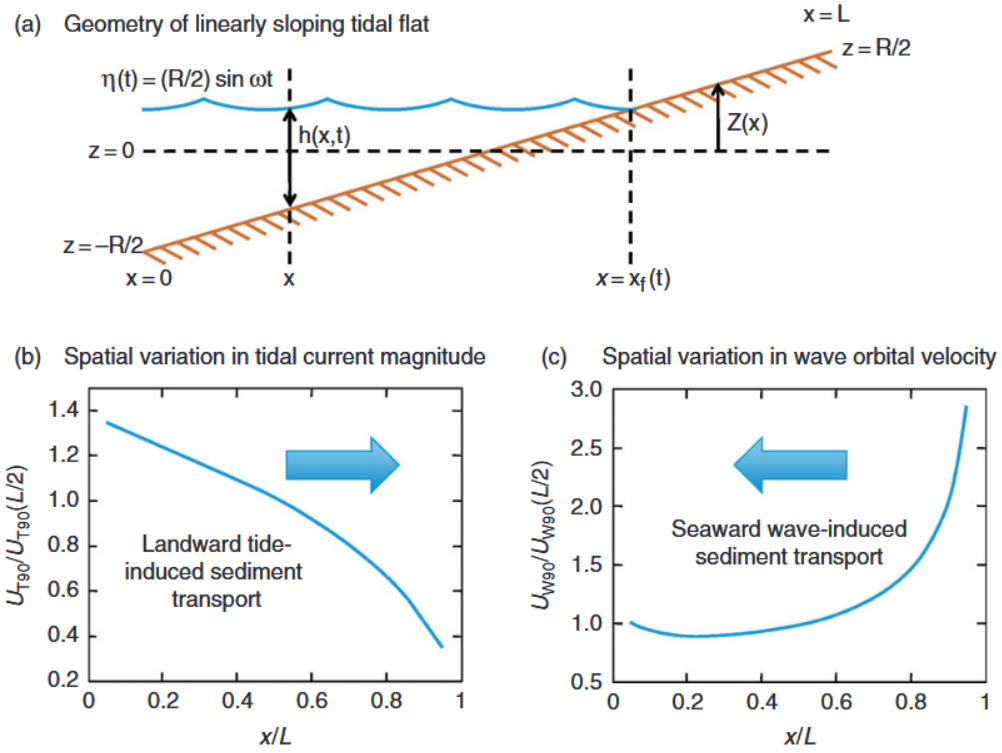

Figure 2.13: Schematic representation of tidal and wave orbital velocities along a linearly sloping tidal flat ($x/L = 0$ representing the most seaward point, $x/L = 1$ the most landward). The y-axes give the ratio of 90th percentile velocities relative to their magnitude at the middle of the profile ($L/2$). Tides are assumed to be sinusoidal; wave heights are assumed to be constant across the entire cross-shore profile (Friedrichs, 2011).

Dynamic Equilibrium and the role of Waves

Numerous studies reviewed in Friedrichs (2011) connect the effect of tidally-induced energy gradients and accretionary conditions to convex-up tidal flat profiles (like the typical Western Scheldt flat profile shown in figure 2.5). The same analysis links wave driven energy gradients and erosive conditions to concave-up profiles. They propose these contrasting conditions as extremes between which tidal flats develop under a seasonally varying dynamic equilibrium.
The erosive property of wave forcing has been attributed to ensuring morphological stability of tidal flats in the long term (Le Hir et al., 2000). The interaction of accreting barotropic tidal processes and erosive waves balance flat morphology, maintaining a dynamic equilibrium (Gatto et al., 2017). This phenomenon has also been identified on the Westkapelle tidal flat in the Western Scheldt. Small waves ($H = 0.05 - 0.1m$) were found to keep the flat morphology in a dynamic equilibrium through negative feedback loops with flat bathymetry (Maan et al., 2018). The study attributed this to two processes. Across the sub-tidal zone, the impact of small waves increased with rising elevation due to decreasing water depths. On the intertidal zone, wave impact increased due to shoaling as bed slopes increase (Maan et al., 2018).

2.3. Wave driven Sediment Transport

Waves effect sediment transport on tidal flats in multiple ways. Both bedload and suspended load transport are induced by wave propagation, however suspended load is most relevant for tidal flats due to the prevalence of fine sediments. Wave orbital velocities generate bed shear stresses, which lead to the (re)suspension of sediments into the water column. Once suspended, wave and/or tidal currents can drive onshore or offshore transport until the fluid shear stresses are small enough for the sediments to settle again under gravity.
Theoretical formulations of sediment transport are often difficult to apply in the field, therefore many studies make use of proxies to describe sediment transport through other variables which can be measured. This section will briefly present the current theoretical and proxy formulations used for wave-driven suspended sediment transport.

2.3.1. Suspended Sediment Transport

Suspended sediment transport is defined by the integral over the water depth of the product between horizontal flow velocity $U(t)$ [m/s] and concentration $C(t)$ [g/L] (Green & Coco, 2014). Each term can be decomposed into a tidal and wave component as shown in equations 2.1 and 2.2.

$$U(t) = U_t(t) + U_w(t) \tag{2.1}$$

$$C(t) = C_t(t) + C_w(t) \tag{2.2}$$

Both $U_t(t)$ and $U_w(t)$ are vectors, while $C_t(t)$ and $C_w(t)$ are scalar magnitudes. Therefore when averaging over the timescale of multiple waves (represented by overbars), $\overline{U_w(t)} = 0$ whereas $\overline{C_w(t)} \neq 0$. Equation 2.3 represents the total time averaged suspended sediment transport. The term $\overline{U_w(t)C_w(t)}$ describes wave driven transport, also explained as the variation of SSC at the timescale of wave orbital motions. Meanwhile $\overline{U_t(t)}\,\overline{C_t(t)} + \overline{U_t(t)}\,\overline{C_w(t)}$ represents the tide driven suspended sediment transport. This is commonly explained as the horizontal advection of sediments suspended by tides and waves (Green & Coco, 2014).

$$\overline{U(t)C(t)} = \overline{U_t(t)}\,\overline{C_t(t)} + \overline{U_t(t)}\,\overline{C_w(t)} + \overline{U_w(t)C_w(t)} \tag{2.3}$$

The above formulation has successfully been used in sandy environments. de Bakker et al. (2016) computes the wave driven transport from distinct infra-gravity and sea swell frequency bands, comparing how the two contribute to the total transport. Meanwhile in tidal flat environments, Green et al. (1997) finds that the wave driven component is 10-15% of the total when waves actively suspend sediments. The transport was found to be in the direction of wave crest propagation, thus with the wind. This enlarged onshore transport at flood and reduced offshore transport at ebb. Interestingly, Green et al. (1997) also found a consistently offshore transport of a few percent of the mean flux at a meandering low frequency timescale. This result appears to suggest an offshore long wave transport of fine sediments, which is of interest for the case of a spectral approach. Despite these findings, other studies listed in Green and Coco (2014) describe a wave transport counter to the current direction. Research is therefore not conclusive regarding the direction of wave driven suspended sediment transport on tidal flats.

2.3.2. Wave induced sediment (Re)Suspension

In many studies the common approach is to assess the influence of waves on sediment suspension, not sediment transport. Suspended sediment transport is difficult to attribute on tidal flats due to the combination of tides, waves and wind forcing. Furthermore, sediment can be supplied from other areas of the estuary due to wider channel flat bathymetries.

Many studies use wave orbital velocities and bed shear stresses to describe the suspension of sediment on tidal flats. This is done by measuring current and orbital velocities close to the bed, whilst also measuring the SSC. Relations in the velocities and SSC measurements can indicate suspension patterns (Green, 2011; Green et al., 1997; Q. Zhu et al., 2019). According to Green and Coco (2014),

patterns in peak wave orbital velocity U_w and wave driven bed shear stress τ_w are followed by similar patterns in sediment suspension.
The results from Green (2011) are of particular interest, since they found that SSC responded more clearly to wave driven orbital velocities than the total current. This finding enforces and confirms the relevance of wave driven sediment transport on tidal flats.
In the same study by Green (2011), a strong positive relation was found between wave orbital acceleration and SSC of fine silt ($10 - 20\mu m$). As acceleration is dependent on wave period, this too could be linked to the suspension of fine sediments on the flat. This was discovered due to the site exhibiting a smooth bed regime, making the wave friction factor (f_w) dependent on wave period (via the wave Reynolds number) and not on relative roughness (as shown earlier).

Suspension-based descriptions do however have limitations, as SSC can result from a number of processes in the entire estuary. The actual transport of suspended sediments can also not be determined from sole concentration measurements. Sediments can be advected by tidal currents or supplied by river discharge, making it hard to confidently attribute causal factors. Therefore local changes in SSC can not certainly be attributed to local variations in wave forces.

2.3.3. Orbital Velocities and Bed Shear Stress

The horizontal component of the orbital velocity is most critical for driving a shear stress. The maximum, horizontal, over the wave orbital velocity can be described using linear wave theory as shown in equation 2.4 (Green & Coco, 2014). Wave height H [m], wave period T [s] and water depth h [m] are the controlling parameters. Wave number k

$$U_w = \omega A_w = \frac{\pi H}{T sinh(kh)} \tag{2.4}$$

U_w can also be expressed in terms of the maximum wave semi-orbital excursion A_w, which is given in equation 2.5.

$$A_w = \frac{H}{2 sinh(kh)} \tag{2.5}$$

The resulting (wave cycle averaged) bed shear stresses created by wave orbital velocities can be described using the quadratic friction law. This is shown in equation 2.6 (van Rijn, 1993).

$$\tau_w = \frac{1}{4}\rho f_w U_w^2 \tag{2.6}$$

Wave driven bed shear stress is dependent on the wave friction factor f_w, which has three expressions depending on the hydraulic regime of the wave boundary layer (laminar, turbulent smooth, turbulent rough) as defined by Soulsby (1997). These are presented in equation 2.7 Where $Re_w = \frac{UwAw}{\nu}$ is the wave Reynolds number, with $\nu = 1.2e^{-}6$ being the kinematic viscosity of seawater. The relative roughness is given by $r = \frac{Aw}{k_s}$, where $k_s = 2.5d_{50}$ is the Nikuradse roughness and d_{50} represents the median grain size of the bed.

$$f_w = \begin{cases} 2Re_w^{-0.5}, Re_w \leq 10^5 & \text{laminar} \\ 0.0521Re_w^{-0.187}, Re_w > 10^5 & \text{smooth turbulent} \\ 0.237r^{-0.52} & \text{rough turbulent} \end{cases} \tag{2.7}$$

Wave-current interactions and combined bed shear stresses

Wave and current bed shear stresses interact non-linearly, as found by Soulsby et al. (1993). The following expressions show how wave (τ_w) and current, also called mean (τ_m), induced stresses can superimpose to a total combined bed shear stress. This approach is common for tidal flats due to the combined wave and tide regime. Specifically the root-mean-squared value, as shown in equation 2.8, is to be considered for erosion (suspension) of sediment since it is effected by the total bed shear stress over the entire wave cycle. The maximum combined bed shear stress, given in equation 2.10, is however relevant when considering an erosion threshold like in the Partheniades formulation (Q. Zhu et al., 2019).

$$\tau_{cw,rms} = \sqrt{\tau_m^2 + \frac{1}{2}\tau_w^2} \tag{2.8}$$

$$\tau_m = \tau_c \left[1 + 1.2 \left(\frac{\tau_w}{\tau_c + \tau_w} \right)^{3.2} \right] \tag{2.9}$$

$$\tau_{cw,max} = \sqrt{(\tau_m + \tau_w |cos(\phi_{cw})|)^2 + (\tau_w |sin(\phi_{cw})|)^2} \tag{2.10}$$

Despite the critical role of wave-current superposition, this thesis is restricted to wave driven bed shear stresses only.

2.4. Wave dynamics on tidal flats

While wind speed and fetch length determines the magnitude of waves at formation, it is the water depth that limits the wave height in shallow waters. Analysis by Le Hir et al. (2000) found wave heights on tidal flats to be depth limited by bottom friction. Considering the conservation of energy for a monochromatic wave traveling over a uniform slope with bottom friction, equation 2.11 was obtained. Their formulation finds the depth limited wave height to be dependent on the wave friction factor f_w [-] as well as the bed slope β [-].

$$\left(\frac{H}{h} \right)_{lim} = \frac{15\pi}{4} \frac{\beta}{f_w} \tag{2.11}$$

Small ratios of f_w/β result in negligible dissipation, where waves maintain their wave height (or even shoal) till breaking. Meanwhile large f_w/β ratios dissipate wave heights through bottom friction. On the Brouage mudflat (France), a limit of $H_{rms} = 0.15h$ was identified. The 2016 winter field campaign on Zuidgors by de Vet (2020) found a similar relation, where significant wave heights were limited by $H_s = 0.5h$ ($H_{rms} = 0.35h$ assuming $H_{rms} = H_s/\sqrt{2}$).

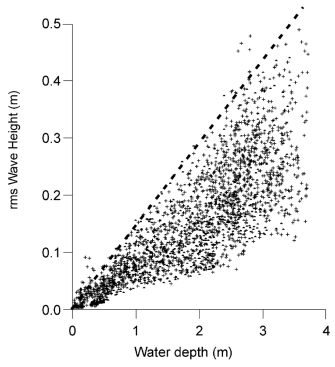

Figure 2.14: Field measurements of H_{rms} $[m]$ across depth h $[m]$ at the Brouage mud flat (Le Hir et al., 2000).

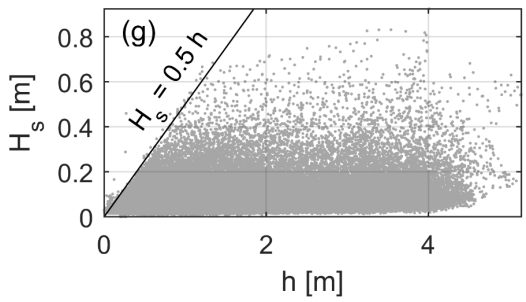

Figure 2.15: Field measurements of H_s across water depth h $[m]$ at the Zuidgors tidal flat (de Vet, 2020).

2.4.1. Long Waves on Tidal Flats

Infra-gravity waves ($T = 20 - 200s$) have been extensively studied on sandy coastlines. Generated by non-linear energy transfers of the sea-swell waves ($T = 2 - 20s$), their effect on sand suspension and cross-shore flux is found to be highly variable in direction and magnitude. de Bakker et al. (2016) attributes this variation to a number of factors, with beach slope playing a significant role. More mildly sloping beaches experience a larger portion of infragravity wave energy (de Bakker et al., 2015). In turn, this can result in large cross-shore sediment fluxes. Field measurements from a mildly sloping beach on Ameland found that infra-gravity wave driven sediment transport made up to 60% of the total cross-shore flux during energetic conditions (de Bakker et al., 2016).

The mild slopes of tidal flats suggest that infra-gravity waves could be important in these environments. However, the sheltered nature of estuaries which contain tidal flats often inhibits sea swell waves from entering the basin. Instead, tidal flats commonly experience smaller and more irregular wind waves ($T = 0.5 - 5s$). These are generated locally by the wind across the fetch inside the estuary (Green & Coco, 2014). Considering this difference in wave climate, there may not be enough energetic sea swell waves for infra-gravity waves to form on tidal flats compared to sandy coasts.
Apart from infra-gravity waves, there are other types of long waves which reach the shores of tidal flats. Estuaries can be forced by seiches which resonate in the form of a partially standing wave. Their height and period are strongly dependent on the basin shape and depth, with typical heights in the range of centimeters and periods ranging from minutes to hours (Guillou & Chapalain, 2024). Their influence on sediment suspension and transport is not well defined. Some studies have made initial attempts to frame seiche induced sediment dynamics. Field measurements from the microtidal Masan Bay found seiches unable to suspend sediments from the bed, yet able to advect already suspended sediments, keeping them in suspension for longer (Seo et al., 2024).
Finally, vessel waves are also to be expected considering the busy navigation channel in the Western Scheldt. These long waves vary depending on the vessel size and the speed at which it travels. Their impact on sediment suspension and transport can be significant, with studies highlighting their role in the erosion of estuarine shoals (Rapaglia et al., 2015). In a microtidal estuary in Florida, the suspension of sediment by vessels was estimated to be an order of magnitude larger than that of wind generated waves (Schoellhamer, 1996).

2.5. Describing Wave and Sediment Dynamics in Sandy Systems

Co-spectral approaches can be used to extract exact frequencies from wave fields which drive sediment suspension. This method is commonly used in sandy environments such as the study by de Bakker et al. (2016). Here co-spectra were constructed using velocity and SSC signals at a gently sloping beach in Ameland. The method highlighted how infra-gravity frequencies modulated the sea swell waves, generating spikes in sediment suspension. Furthermore, the analysis was capable of indicating the direction of the suspended sediment flux by considering the velocity directions. Figure 2.16 gives an example of this approach. The co-spectral density of u and SSC shows predominant suspension due to infra-gravity waves, with sea swell waves inducing little transport.

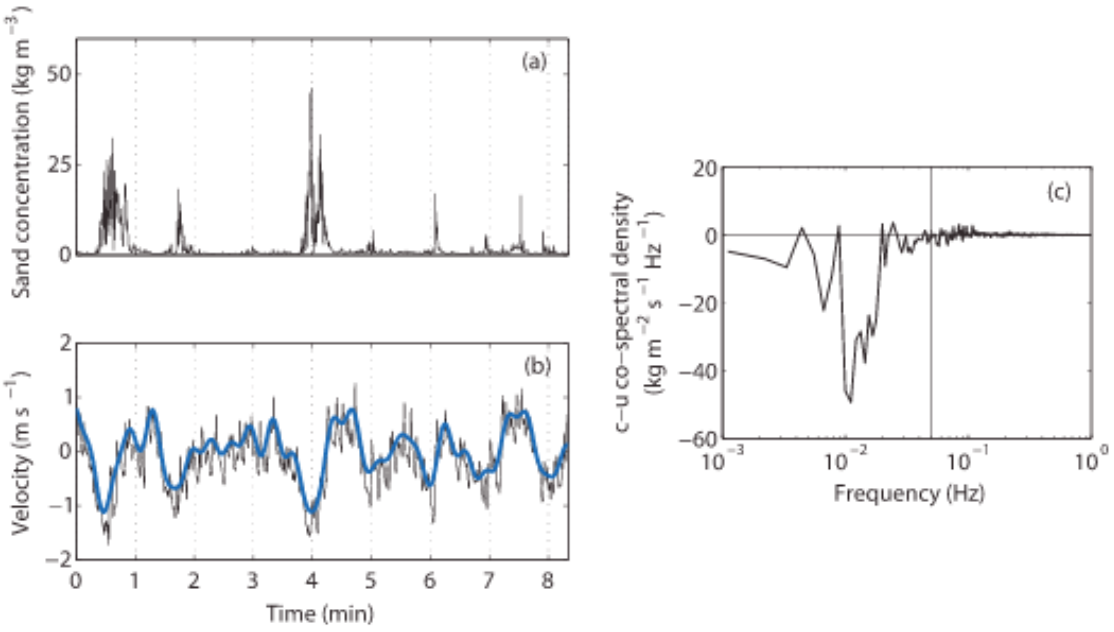

Figure 2.16: Velocity and SSC time series during an energetic high tide at Ameland, with co-spectral density of u and SSC. Predominant suspension for negative u_{IG}, with little suspension due to sea swell de Bakker et al. (2016).

Bosboom and Stive (2023) also describes how the interaction between long and short waves drives unique sediment transport processes due to their phase relations. Long waves drive offshore transport until the surf zone due to their bound nature and phase difference with the incoming short waves that tend to stir the bed. After releasing in the surf zone, these long waves are in phase with the short waves and drive an onshore transport. Meanwhile short waves are often found to drive a consistently onshore transport. The study by de Bakker et al. (2016) enriches this description, as it developed a conceptual model for sand-suspension mechanisms due to interactions between short and infragravity waves. Using field measurements on a gently sloping beach at Ameland, the sand suspension mechanisms were found to depend on the correlation r_0 between short and long waves, as well as their relative wave heights H_{IG}/H_{SW}. Figure 2.17 illustrates the conceptual model developed during the study, showing how transport is first offshore directed, then onshore and finally re-directing off shore in the inner surf zone.

These patterns in sediment transport across long and short waves can be modelled using the energetics approach developed by Bowen (1980). This method makes use of velocity moments as a proxy for suspended sediment transport, and is often applied in sandy coastlines. This is because the energetics approach has been developed for non-cohesive sediments. In a field study by Tas et al. (2020), the energetics approach was utilised to quantify cross shore sediment transport along a sandy chenier in Demak, Indonesia. Collected velocity measurements were decomposed into moments to construct mean current, short wave and long wave components, reviewing their individual contribution to sediment transport. The study showed that waves drive sediment transport directly though skewness and indirectly via stirring. The first always being in onshore direction, the latter depending on the direction of mean flow.
As tidal flats consist of fine, cohesive sediments, the applicability of the approach by Bowen (1980) is to be questioned. However, the principle of the method is inspiring for estuarine environments, as it enriches the description of wave driven sediment transport by considering various components and processes within the wave spectrum.

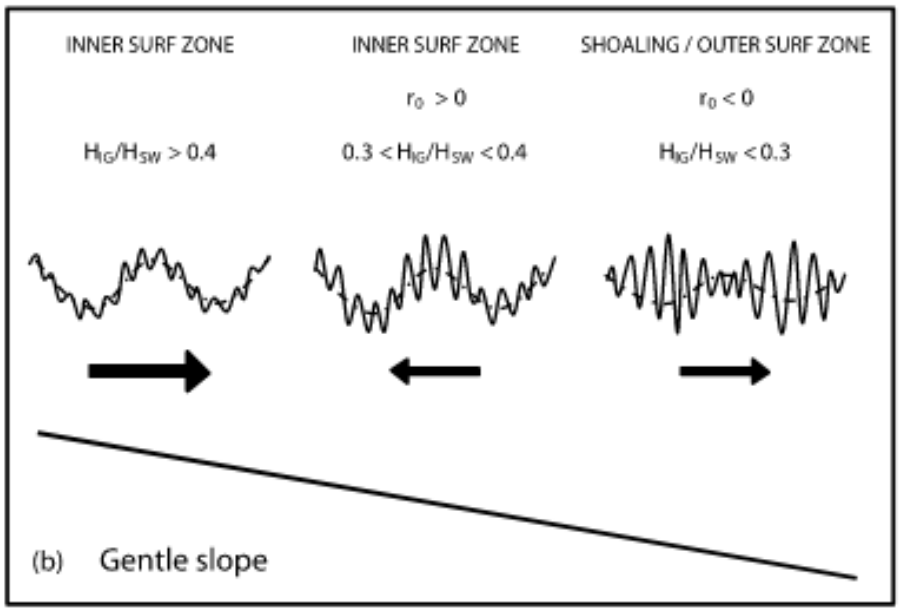

Figure 2.17: Model of sandy sediment transport on gently sloping beaches, showing how correlation r_0 and relative wave height H_{IG}/H_{SW} of infra-gravity waves and sea swell waves effects transport de Bakker et al. (2016).

2.6. Research Gap

Current research has demonstrated that waves play a critical role in suspending sediments on tidal flats, primarily through the generation of bed shear stresses linked to orbital velocities. Higher orbital velocities are associated with increased bed shear, often surpassing erosional thresholds and leading to sediment suspension. Waves have been found to effectively suspend sediments at various locations of tidal flats depending on the stage of the tidal cycle. At low tide, shallow waters allow wave orbital motions to penetrate to the bed near low water. At high tide, longer fetch can generate larger waves which break at the high water. The shear stresses generated by waves often interact with those generated by tidal currents, resulting in amplified stress levels that enhance sediment suspension. Other factors such as inundation time, wind speed and direction have also been identified to influence wave driven sediment suspension. Considering the morphodynamics of tidal flats, waves have been found to play a crucial role in maintaining dynamic equilibrium. This occurs through negative feedback loops, where waves induce more erosion as bed levels increase.

Despite these insights, several important aspects remain under explored. The widespread use of a monochromatic wave approach limits the ability to fully characterize the incoming wave climate. Long waves receive little attention, and spectral wave analyses, which are more common in sandy coastal environments, are rarely applied on tidal flats despite their potential to provide a more complete understanding of wave conditions. Finally, more can be done to understand how waves shape flat morphology and how morphology effects wave dynamics. Especially under the influence of tidal currents and modulated water levels.

This study aims to address these gaps by constructing wave spectra at multiple cross-shore locations to capture both short and long wave components. Stepping away from the monochromatic approach, greater detail can be found in wave transformations, assessing the transformation of various frequencies. By comparing wave spectra, velocity data, and suspended sediment concentrations across different stages of the tidal cycle, this research will assess the dynamic interactions between waves, sediment transport, and tidal flat morphology. Ultimately, the study seeks to develop a detailed understanding of wave and sediment dynamics on muddy tidal flats. This contributes towards a higher aim of understanding wave driven morphodynamics on tidal flats with more detail.

3

Research Method

This chapter describes the research methodology. First the overall approach is introduced, after which the in situ measurement campaign is presented, illustrating the process of site assessment, frame design and instrument programming. The chapter then continues with the data pre-processing steps and the STMS calibration process. Finally, the chapter describes the methods of analysis to answer each sub question as introduced in chapter 1.

This study has gathered hydrodynamic measurements and suspended sediment concentrations on the tidal flat at Gat van Borsele (GvB). ADV sensors have been deployed in tandem with STMS and pressure sensors to gather 3D flow velocities, SSC and pressure measurements. By analysing the local wave dynamics in relation to SSC, the study has strived to deepen the understanding of wave and sediment dynamics on tidal flats.

The high resolution sampling allows for detailed analysis across singular tides to determine the influence of waves on the bed under various water depths, tidal currents and wind conditions. Meanwhile the extensive burst period captures long waves in the spectrum, allowing for these to be considered alongside the local wind waves. Figure 3.1 provides a visual overview of the research method in chronological order. Ultimately the developed method strives to evaluate a spectral approach by answering the question: **"Can a spectral approach provide a better interpretation of wave driven sediment dynamics on muddy tidal flats?"**

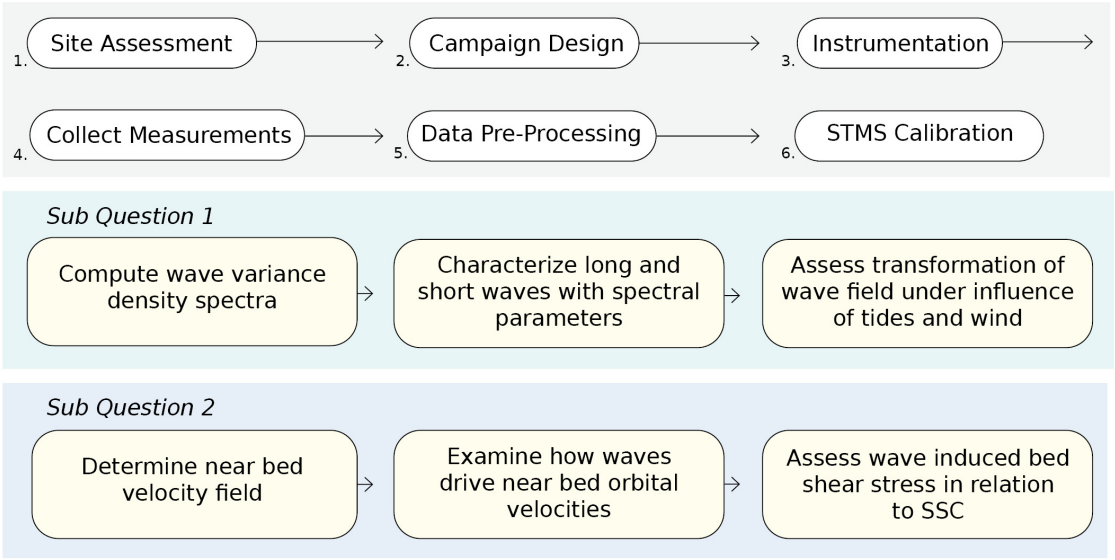

Figure 3.1: Overview of the utilised research method.

3.1. Site Assessment

Since the study aimed to investigate the interaction between wave and sediment dynamics of the full wave field, it was vital to select a tidal flat which would be relatively exposed to waves. Disregarding sea swell waves, which are only of influence at the estuary mouth, local waves are most relevant when considering tidal flat wave exposure. Local waves are generated by the wind conditions in the estuary, therefore potential locations were identified with respect to the dominant wind direction. In the case of the Western Scheldt, south-westerly winds are most common. Thus tidal flats were selected perpendicular to this direction for the highest potential exposure.
Apart from wave exposure, tidal flats were also selected based upon their expected sediment composition. Specifically looking for flats exhibiting fine and cohesive sediments such as mud and silt. The study sought to apply spectral analysis techniques to both hydrodynamic and SSC datasets. The value of which has generally been under-explored for the case of muddy tidal flats.

Considering both wave exposure and muddy sediments, a number of potential sites were selected as shown in panel (a.) of figure 3.2. The conditions were confirmed with a site reconnaissance, after which the tidal flat at Gat van Borsele was chosen. The flat satisfied both criteria, whilst also being easy to access without disturbing natural reserves.
The tidal flat has a width of approximately 800m at MLW and decreases in landward direction. The flat spans a length of approximately 450m from the dike to MLW, after which the bathymetry drops steeply from -2 to -8 m NAP. Despite the flat being enclosed by dikes on either side as shown in panel (c.), its orientation allows for waves from south-westerly winds to enter the flat effectively. The flat is relatively bare, with little presence of macro-benthos except for sparsely scattered oyster clusters near MLW. On the upper section of the flat there are extensive biofilms covering large portions of the surface. Panel (d.) in figure 3.2 was taken during frame retrieval at the GvB tidal flat, with clear biofilms in an undulating pattern on the upper flat.

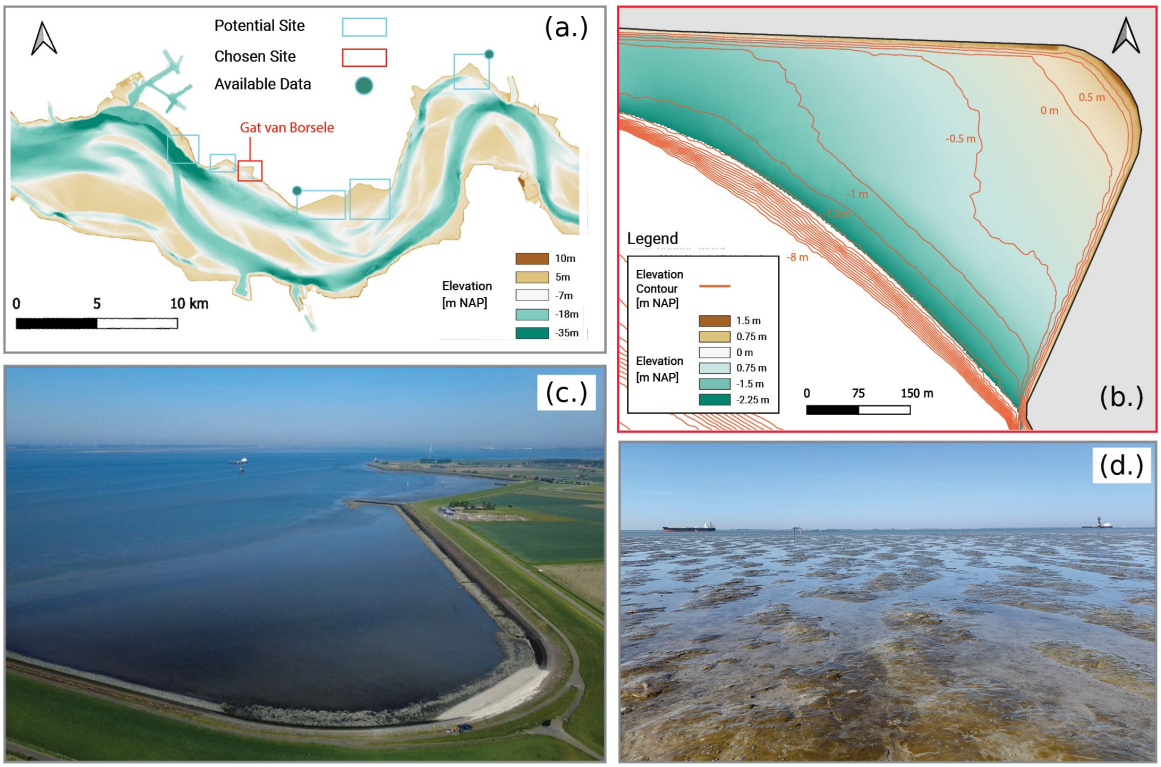

Figure 3.2: Potential and selected sites, with bathymetry map of the Gat van Borsele (GvB) tidal flat. Panel (a.): 2022 Bathymetry of Westerschelde from Rijkswaterstaat, with potential sites highlighted. Panel (b.): 2021 Lidar Bathymetry of the GvB tidal flat from Rijkswaterstaat, with 2018 depth contours. Panel (c.): Aerial photo of the GvB tidal flat, taken on 15/05/2025 by Jianwei Sun. Panel (d.): Photo of the bed at the GvB tidal flat, taken on 15/05/2025 by author.

3.2. Campaign Design

The field campaign took place using three measurement frames along a cross-shore transect in the centre of the tidal flat. The campaign measured one month of data at each frame, specifically from the 10th of April till the 10th of May. The chosen locations and duration allowed for cross-shore variations to be observed in both wave dynamics and sediment suspension across spring-neap tidal cycles.
To determine the optimal locations of the three measurement frames, a cross-shore transect was measured during the site reconnaissance with a GPS survey. This gave the elevation profile shown in the right panel of figure 3.3. The cross-shore profile has been plotted against a histogram of 2024 tidal elevations as shown in the left panel. This was constructed using astronomical tides determined at the Rijkswaterstaat measurement gauge in Gat van Borsele, positioned 1km from the considered tidal flat. The figure shows how the slope of the flat is steep till MLW, then flattens out and becomes more linear. The flat is completely inundated at high water, with even the most shoreward point lying 1.1m below MHW. The width was also profiled at MLW with GPS, revealing a relatively homogeneous profile with elevation variations of 10cm across the width of the flat.
The results from figure 3.3 were used to determine the optimal locations for the measurement frames. By locating the lowest frame correctly, it was intended to allow the ADV and STMS sensors to collect data during the most common low water level. This is preferable due to the expected high impact of waves during low water levels on the lower flat. The middle and high frames were positioned such that the distance between each frame is approximately equal.

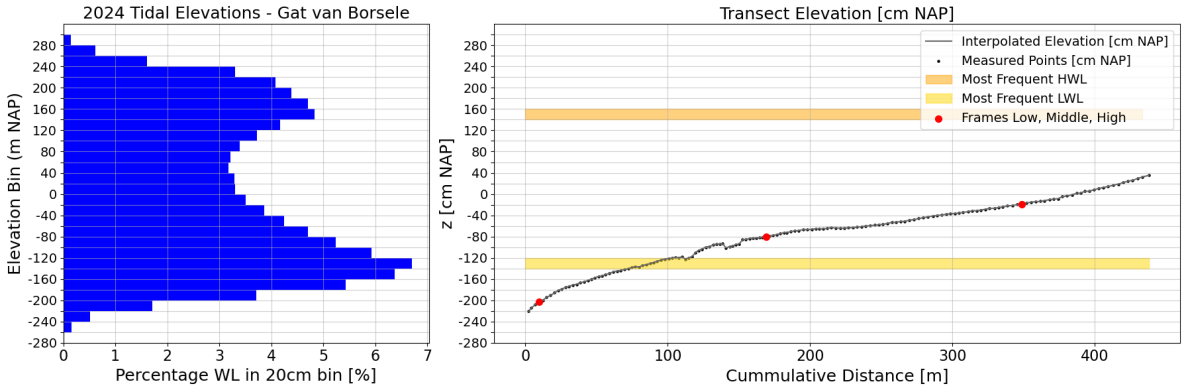

Figure 3.3: Left: Histogram of tidal surface elevations during 2024, taken at the Gat van Borsele measurement station of Rijkswaterstaat (Rijkswaterstaat, 2025). Right: Cross-shore elevation transect at the Gat van Borsele muflat, taken on 18/03/25. The most frequent low/high water level is given in yellow/orange. Intended measurement frame locations are shown in red.

3.3. Instrumentation

Observations were gathered at the low, middle and high transect locations using identical measurement frames. Each frame was equipped with an ADV (Acoustic Doppler Velocity meter, 300m Vector, Nortek AS, Norway) to measure 3D velocities and pressures. These were coupled with an STM-S (Seapoint Turbidity meter, Seapoint Sensors Inc., USA) to measure SSC signals.

Intermezzo: ADV and STMS sensors Explained

ADV sensors measure underwater velocity along 3 axes using accoustic signals and the Doppler effect. The instrument emits two closely spaced acoustic pulses, which reflect off suspended particles like sediment or plankton. By analysing the phase shift between the returned signals, it calculates the water's velocity (Nortek AS, 2018).
Turbidity meters, like STMS, determine the backscatter of light which is influenced by the number of suspended particles in the water column. By taking sediment samples at the sensor location, it is possible to calibrate the sensor such that the backscatter can be related to specific concentrations of the local sediment (Seapoint Sensors, Inc., 2013).

The ADV frames were designed such that tide induced turbulence is minimized around the measurement volumes. Since the tidal velocities far exceed the wave-driven, it was chosen to accept the smaller potential interferences in the direction of wave propagation. This resulted in the ADV frames being positioned perpendicular to the direction of wave propagation. The ADV probe heads were positioned pointing downwards, with the x-axis parallel to the cross-shore transect. The y-axis was perpendicular to this, measuring in the alongshore direction. The z-axis is positive upwards. Figure 3.4 provides a full schematic of the ADV frame design. The schematic illustrates the position and orientation of each instrument, as well as the frame size.

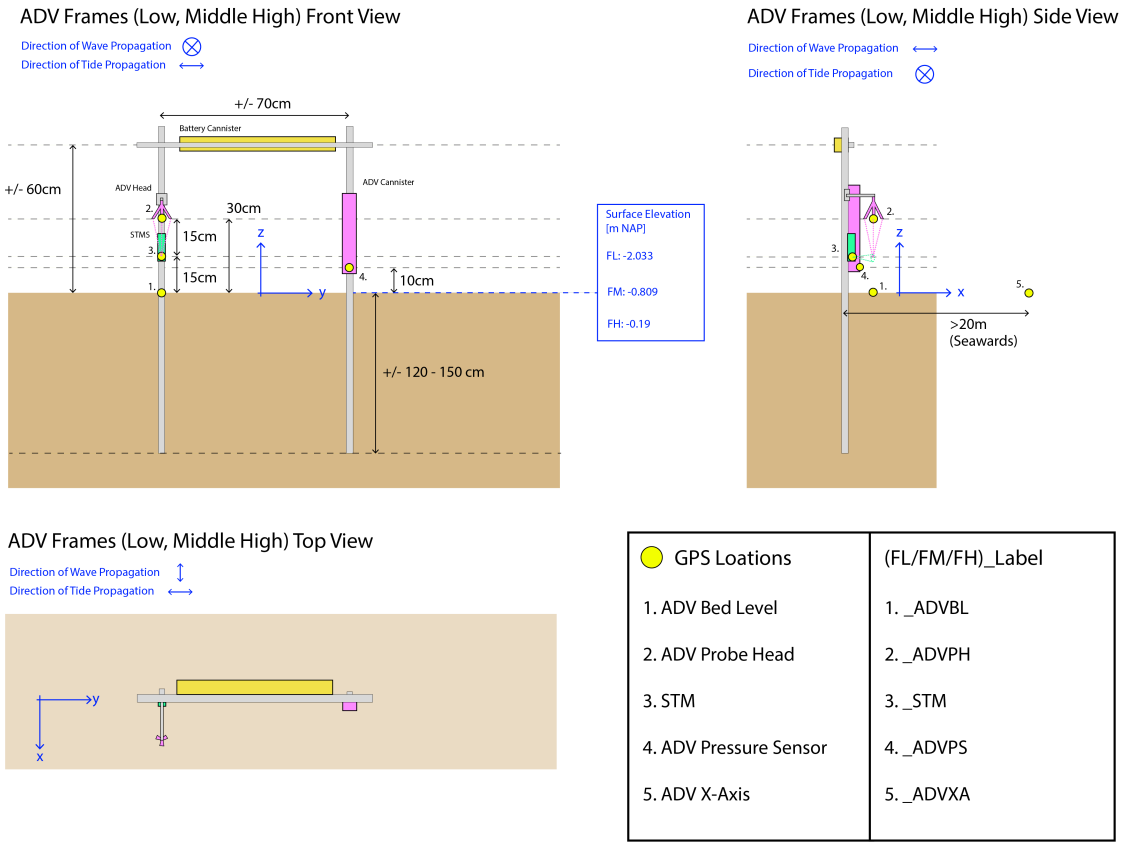

Figure 3.4: ADV-STMS frame schematic, giving front, side and top views of the frame design. Instruments and batteries are highlighted with relevant measurements and distances indicated.

The ADV heads were placed 30 cm from the bed, such that the sampling volume of 14.9mm was positioned 15cm above the bed. The vertical orientation allowed for a horizontal velocity range of 2.1 m/s and a vertical velocity range of 0.6 m/s. These ranges capture the range of flow velocities found at the Zuidgors tidal flat by de Vet (2020).
The ADV sensors were programmed to measure with a sampling frequency of 16Hz, for bursts of 20 minutes every 40 minutes (20 minutes on - 20 minutes off). These high resolution bursts can detect local waves in detail whist measuring for long enough to resolve long waves in the spectrum. These criteria were deemed critical to achieve the intended research method and capture the full wave field.
The STMS sensors were positioned at the same elevation, measuring at 15cm from the bed pointing towards the sampling volume. The pressure sensor was located at 10cm above the bed, and was positioned such that it measures at the same cross-shore location as the ADV-STMS pair. Table 3.1 provides an overview of all instrumentation and measured parameters.

Parameters	Instrument	Sampling Method	Sites
Waves (Pressure)	ADV Pressure Sensor	Pressure probe was 10cm above the bed. Sampling at 16Hz for 20 minute bursts every 40 minutes.	FL, FM, FH
3D Velocities	ADV Probe Head	Sampling volume (14.9mm) was 15cm above the bed. Sampling at 16Hz for 20 minute bursts every 40 minutes.	FL, FM, FH
SSC	STMS	STMS sensor was 15cm above the bed. Synced to ADV, Sampling at 16Hz for 20 minute bursts every 40 minutes.	FL, FM, FH
Sediment Sample	NA	Sampling 1L of surface sediment for STMS calibration.	FM

Table 3.1: Instrument inventory organized by parameter and sampling method

3.4. Final Frame Locations

Figure 3.5 shows the final frame locations along with three cross-shore transects which were measured during the reconnaissance, deployment and retrieval. The frames were placed near the intended locations without any creeks, bed forms or macrobenthos which may disturb the measurements. Table 3.2 gives an overview of the sensor elevations with respect to NAP and relative to the local bed level. Sensor displacement was checked for the middle frame by comparing GPS measurements during deployment and retrieval. This revealed acceptable displacements of the sensors, largest being 1cm.

Sensor / Location	Frame Low (FL)		Frame Middle (FM)		Frame High (FH)	
	Elevation [m NAP]	Relative [cm]	Elevation [m NAP]	Relative [cm]	Elevation [m NAP]	Relative [cm]
Bed Level	-1.931	NA	-0.810	NA	-0.202	NA
ADV Probe Head	-1.616	31.5	-0.508	30.2	0.094	29.6
ADV Sampling Vol.	-1.766	16.5	-0.658	15.2	-0.056	14.6
STMS	-1.772	15.9	-0.669	14.1	-0.061	14.1
Pressure Sensor	-1.833	9.8	-0.706	10.4	-0.109	9.3

Table 3.2: Sensor elevation data at deployment (10/04/2025). Elevation in m NAP; relative elevation in cm above bed.

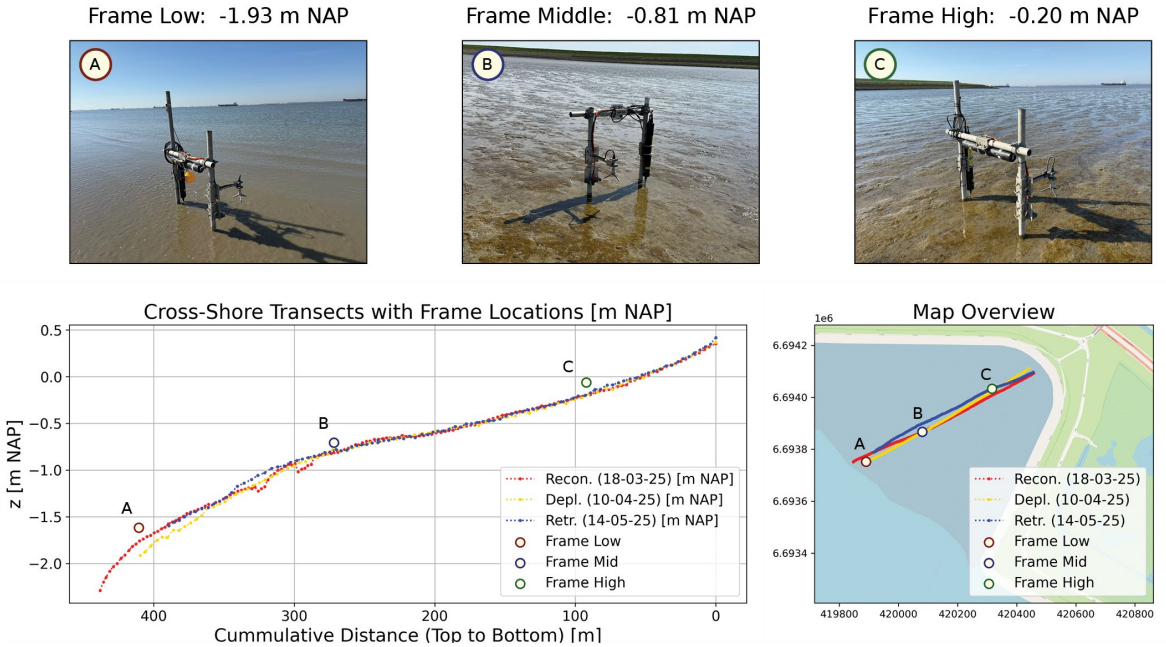

Figure 3.5: Overview of ADV-STMS frames on location. Top: Frames before retrieval at low, middle and high locations. Bottom Left: Cross-shore profiles with frame locations. Bottom Right: Map overview of frame locations along cross-shore transect.

To gain insight into the x-axis orientation of each ADV probe head, a line of three points was measured in the direction of the x-axis probe. The calculated angles of each x-axis with respect to true North. were 307.45, 303.39 and 304.15 degrees (Clockwise positive) for the low, middle and high frames respectively. Despite their small differences, they are generally oriented in the same direction which allows for consistency when comparing between the frame's wave and velocity measurements.

3.5. Data Pre-Processing and Despiking

The raw data from the measurement frames required a number of pre-processing steps, which are presented in the following section. The listed steps were undertaken to clean the datasets, and prepare them for analysis.

1. Correct pressure signal for atmospheric changes and compute hydrostatic water levels.
2. Quality Control:
    - Remove outliers considering poor ADV signal correlation, sensor measurement ranges and statistical outliers.
    - Remove measurements during sensor emergence.

3.5.1. Pressure signal correction

To correct the pressure measurements, the signal for each ADV was first set to zero. Since the ADVs began measuring just before deployment, these measurements were emerged and thus function as a baseline for the local atmospheric pressure.
Then, using hourly observations from the KNMI weather station in Vlissingen (15km from site), it was possible to compute the local variations in air pressure and subtract these from the original pressure signal. Finally the hydrostatic water level could be computed using the hydrostatic pressure equation, using the corrected pressure signal. Figure 3.6 provides an example of this process using the observations from FL. Note that the initial and final measurements (at zero) have been removed for the figure, since these were during deployment and retrieval of the frames.

$$\eta_{FL} = \frac{P_{FL} - P_{atm}}{\rho g} + z_{FL} \tag{3.1}$$

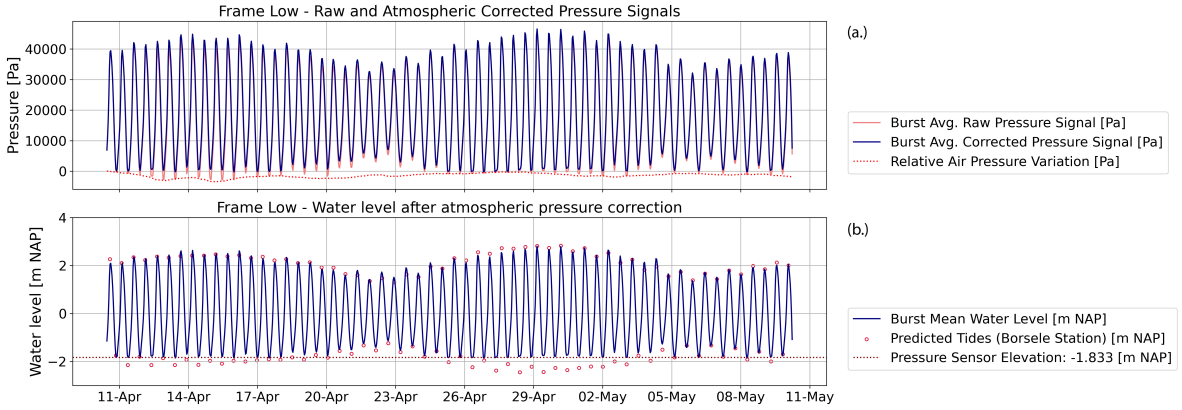

Figure 3.6: Top: Corrected and raw pressure signal for FL plotted with local air pressure variations. Bottom: Hydrostatic water level in meters NAP at FL

3.5.2. Quality Control: Removing Outliers

The raw data underwent a quality control process as illustrated in the flowchart in figure 3.7. First outliers were removed based upon three criteria for both pressure and 3D velocity measurements: 1. Fails minimum correlation threshold, 2. Lies outside programmed sensor range, 3. Consecutive values differ more than 3σ (velocities) or 4σ (pressure).

Measurements that failed these criteria were removed from the signals. Bursts with few NaN values (<5%) and small gaps (<8 consecutive NaNs) were interpolated. Bursts with more than 5% NaN values were not interpolated. Instead these gaps were filled with the burst mean. Bursts which consisted completely of outliers were discarded. Figure 3.8 shows the distribution of bursts considering the pressure and velocity values of each measurement frame. The low frame performed best, whilst the middle and high frames exhibited more outliers. This is likely due to the more frequent emergence of these ADV sensors.
Finally, the last sample of each burst was removed due to a recurring error in the ADV measurements. This resulted in bursts of N=19199 Samples.

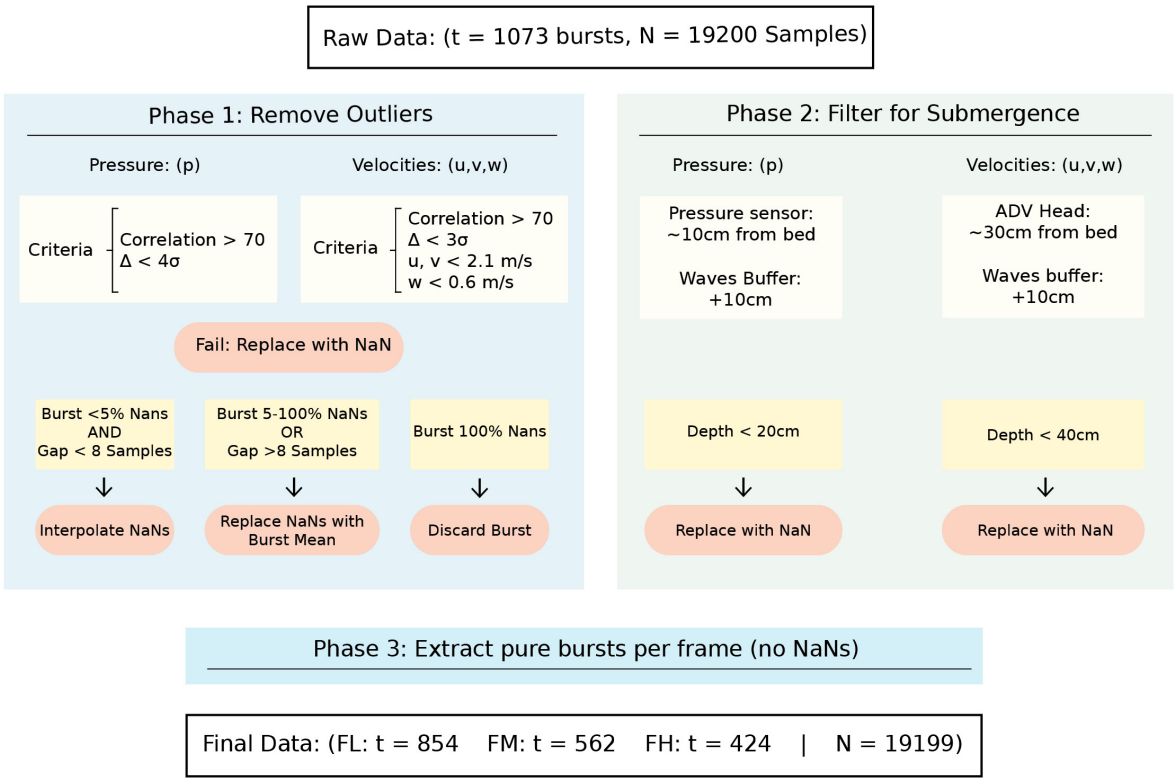

Figure 3.7: Quality Control procedure for measured pressure and velocities: First removing outliers, then filtering for emergence and lastly selecting pure bursts for analysis.

3.5.3. Quality Control: Filtering for Submergence

Emergence of the ADV probe head and pressure sensor is the most common reason for incorrect measurements. Despite outliers often occurring during emergence, the two steps have been separated to filter accurately and thoroughly. As shown in figure 3.7, the elevation of the pressure sensor and ADV head were considered individually. Considering the effect of waves an additional 10cm was added to the elevation threshold to ensure for complete submergence. The results of this filter are shown in the right side of figure 3.8, as expected emerged bursts increase with increasing frame elevation.

Measurements which failed these criteria were removed and not interpolated or substituted. Finally all bursts containing any NaN value were removed from the dataset. After filtering outliers and for submergence, 854 bursts were available for Frame Low, 562 bursts for Frame Middle and 424 bursts for Frame High. Figure 3.9 gives an overview of the filtered burst averaged tidal signal and 3D velocities for the low frame.

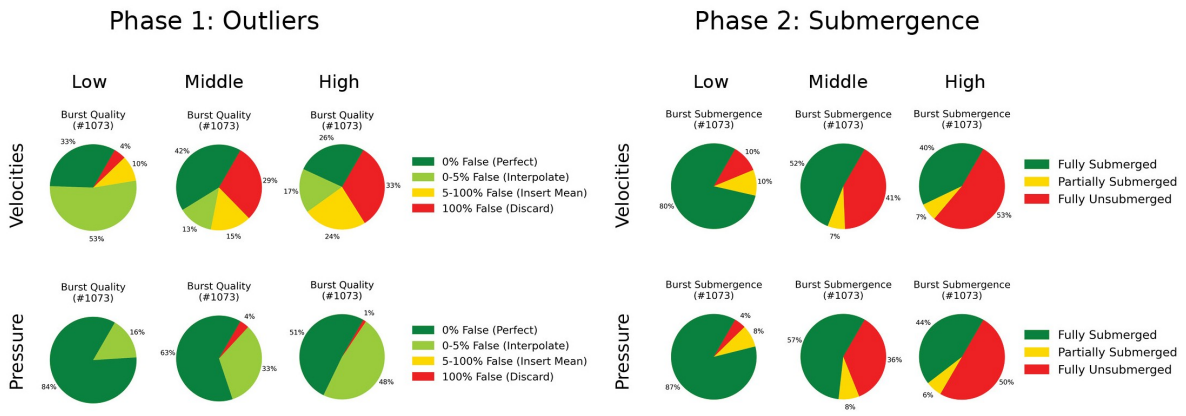

Figure 3.8: Results from the quality control procedure, categorising all 1073 bursts taken during deployment. Left: Pie charts of burst quality after filtering for outliers in pressure and velocity signals. Right: Pie charts of burst submergence.

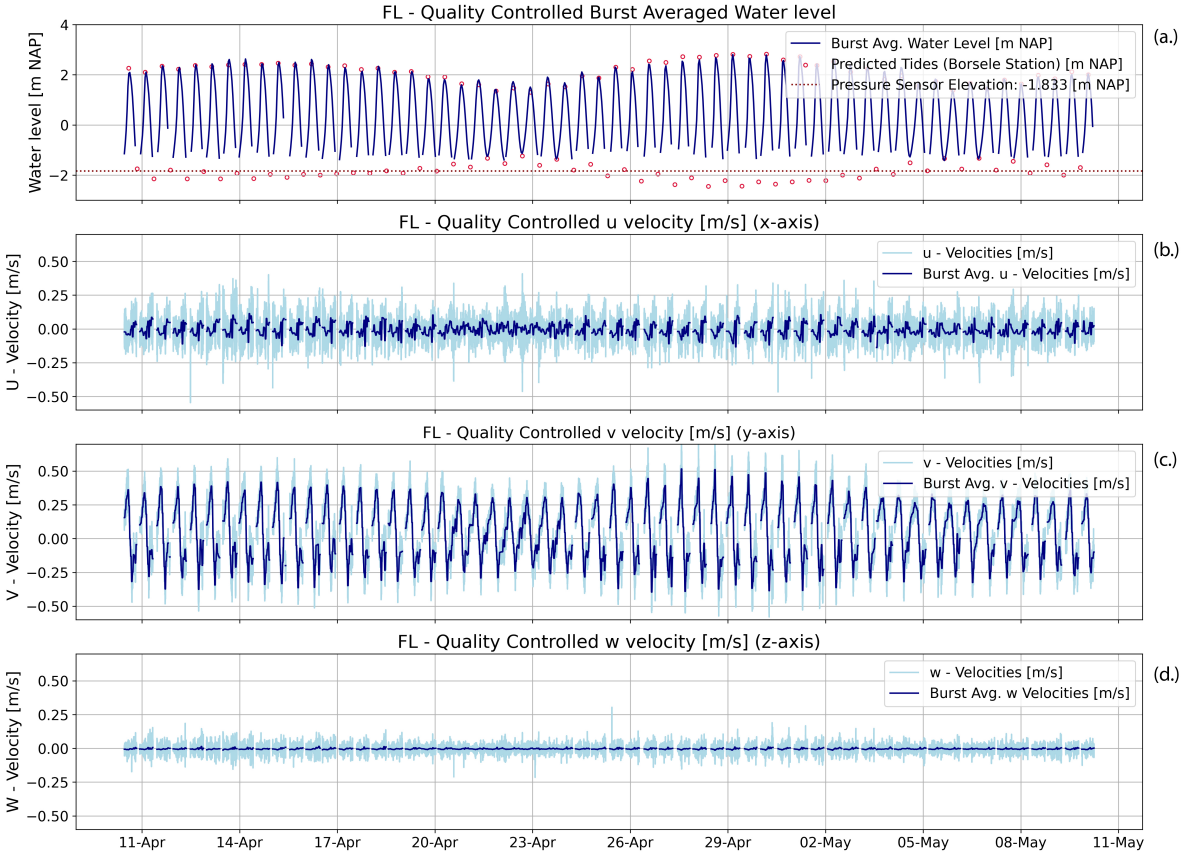

Figure 3.9: Quality Controlled Datasets at Frame Low. Panel (a.): Burst averaged hydrostatic water level. Panels (b, c, d): 3D velocities (u, v, w).

3.6. STMS Calibration

The STMS sensors were individually calibrated using a sediment sample taken at the locaction of the middle frame. A wet calibration was performed in a 40L bucket for the three STMS sensors simultaneously. The right image in figure 3.10 illustrates the calibration setup. The three STMS sensors were clamped at a fixed position whilst being submerged in the bucket. Each STMS was connected to the exact ADV sensor which was used in the field to ensure consistency. The use of an electric agitator ensured that the sediments were kept in suspension during the calibration.

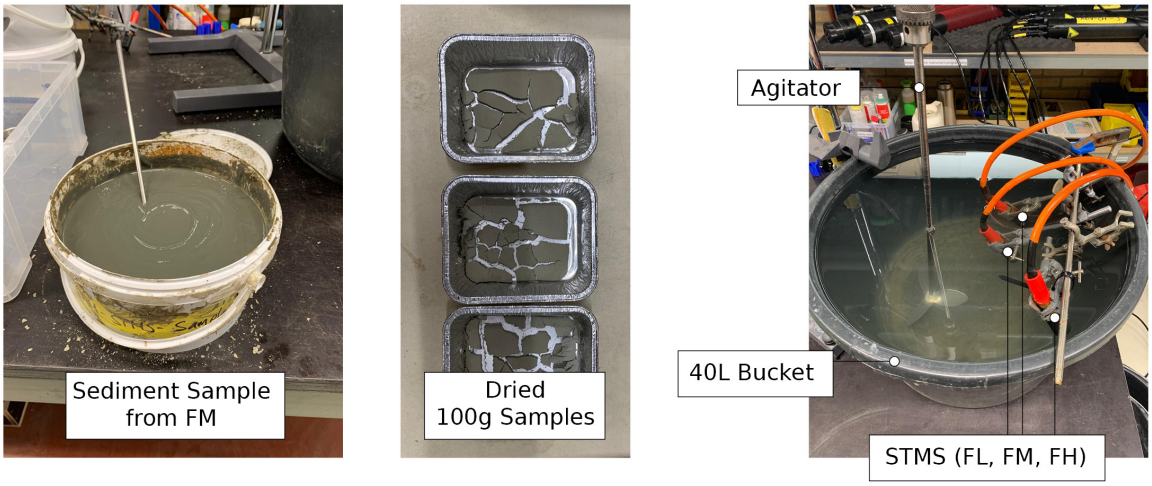

Figure 3.10: Left: Prepared sediment sample taken from the middle of the GvB tidal flat. Center: Three dried samples used to compute a conversion factor between wet and dry mass. Right: Calibration set-up, using a 40L bucket with an agitator to suspend sediments. The three STMS sensors were kept submerged using clamps.

The approach started by determining the wet to dry mass factor. By drying out three samples of 100 grams each, a factor was estimated of $F_{wet-to-dry} = 2.48$. Then by adding a known wet mass using the conversion factor, an upper limit concentration could be created within the 40L volume. Lower concentrations were achieved by replacing a fourth of the total (turbid) volume with clear water for each measurement point. Once the concentration reached below $c = 0.5g/L$, half of the volume was refreshed.

Intermezzo: The assumption of a wet STMS calibration

The critical assumption of the wet calibration method is that all added sediment is kept in a homogenous suspension throughout the calibration. Thus by removing a quarter of the turbid volume, the ”homogenous” concentration is reduced by the same factor. In reality not all sediments will be kept in suspension; the heavier sediments will settle to the bottom of the container, resulting in underestimated SSC values. However, this effect is deemed minimal due to the relatively high fraction of fine sediments in the sample. Therefore the method has been considered appropriate for calibration.

The calibration started with a concentration of $c = 12.91g/L$ and ended at $c = 0.023g/L$ with a total of 16 measurement points per STMS sensor. This was limited to $c = 5.45g/l$ and 13 points, since the sensors measured lower counts for concentrations above this limit. This turning point is characteristic of STMS sensors. Measurements above were discarded since they are not physically representative.

By reading the counts for each STMS sensor at each concentration of suspended sediment, it was possible to fit custom curves to each sensor such that the signals could be converted to SSCs. For the three sensors, a linear fit was performed up to 20000 counts. After this threshold, a quadratic polynomial was fit to the measurements. Figure 3.11 shows the calibration curves for frames low, middle and high. Considering the visual fit together with the r-squared values, they are expected to give an accurate transformation from counts to SSC.

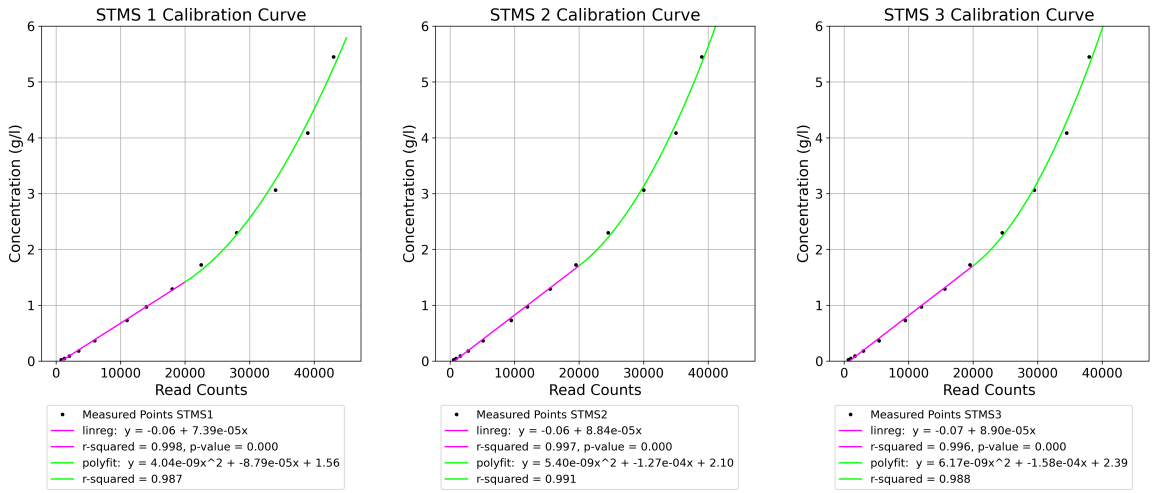

Figure 3.11: Calibration curves for the STMS sensors at the low, middle and high frames. Linear fit till 20000 counts, quadratic fit for > 20000 counts. Constructed using measurements from a wet calibration.

Observing the counts of each STMS sensor, they predominantly lie below 20000 counts with the exception of some outliers. Most observations have therefore been converted using the fitted linear relations. The resulting burst averaged SSC signals are shown in figure 3.12 for each frame. Concentrations lie between 0 and 0.6 g/L, with the tidal range clearly influencing mean concentrations in line with the spring-neap cycle. There is also a clear decrease in concentrations across the tidal flat, with higher concentrations consistently being observed at the low measurement frame.

Outliers were filtered using a similar approach to the pressure, where STMS count entries were removed if the difference between consecutive values exceeded 3σ. Then all converted SSC values were filtered for positive values, since small counts were otherwise converted to a non-physical negative concentration.

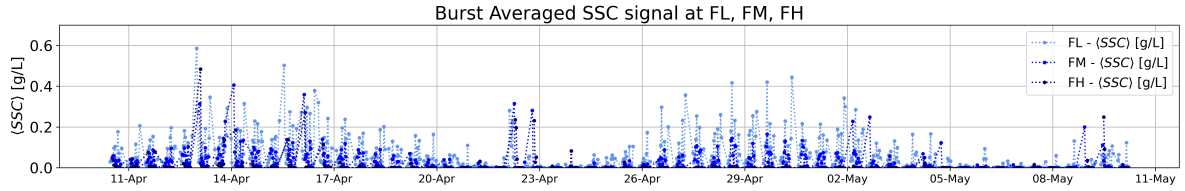

Figure 3.12: Processed SSC signals [g/L] for the low, middle and high measurement frames (FL, FM, FH). Signals were obtained using the calibration curves for each STMS sensor.

3.7. Assessing the tidal flat wave climate using wave spectral analysis (SQ1)

Using the obtained pressure measurements, it was possible to conduct a spectral analysis computing the surface elevation variance density spectra of each burst. With these, spectral parameters could be determined as well as the development of long and short waves across the flat under varying tides. Spectral parameters such as H_{m0} and T_p give a general overview of the incoming wave field, where additional depth was be gained through assessing the development of separate low and high frequency domains. Figure 3.13 illustrates the applied method, leading to an understanding of how components within the wave field transform across the tidal flat under influence of varying water levels, tidal currents and wind.

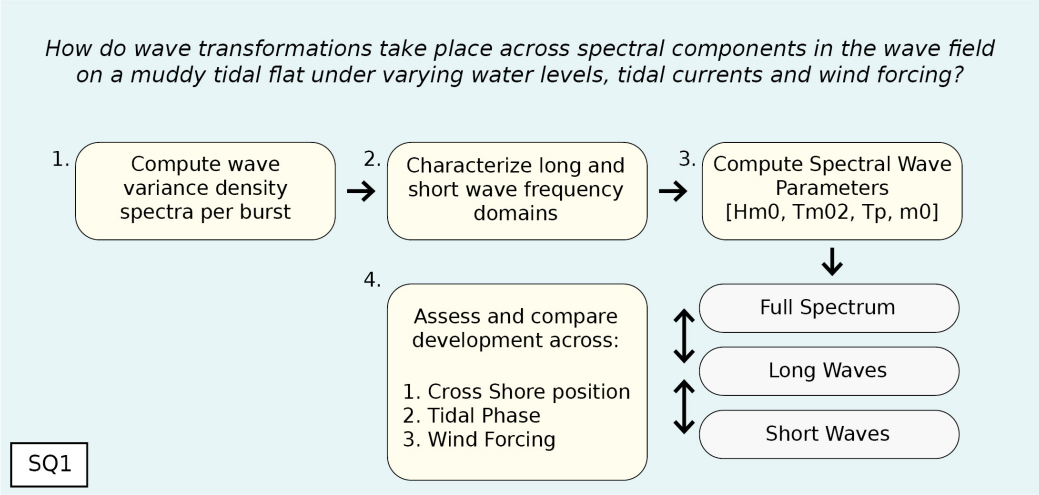

Figure 3.13: Flowchart presenting the utilised method to answer sub-question 1.

3.7.1. Surface Elevation Variance Density Spectra

Before computing the burst spectra, the corrected pressure time series $p(t)$ was converted to hydrostatic surface elevation $\eta(t)$, as per equation 3.1. Then each elevation time series was parabolically detrended and had its mean removed, preparing the bursts for spectral processing. Figure 3.14 illustrates the preprocessing steps undertaken for each elevation burst time series.
The surface elevation variance density spectra were computed using Fast Fourier Transforms FFTs. Equation 3.2 shows the Discrete Fourier Transform which transforms an equally spaced time series of samples $\eta(t)$ with length N [m] into their respective frequency components $A_\eta(f)$.

$$A_\eta(f) = \sum_{t=0}^{N-1} \eta(t) e^{-i2\pi ft/N} \tag{3.2}$$

After converting the obtained amplitudes to variance density $S_\eta(f)$ $[m^2/Hz]$, Welch averaging was applied to reduce the magnitude of error. Hamming windows were used with an overlap of 50%. This divided each burst time series into a number of equal overlapping blocks, computing $S_\eta(f)$ for each and compiling an average spectrum.

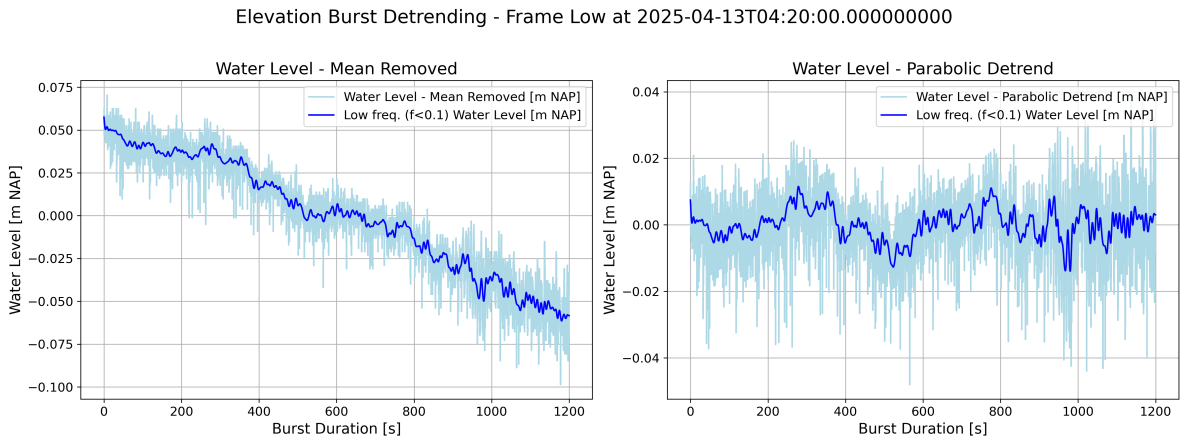

Figure 3.14: Example of undertaken preprocessing steps for elevation burst time series $\eta(t)$ [m]. Left: Elevation time series with mean signal removed. Right: Parabolically detrended time series.

Wave induced pressure is attenuated with depth (Holthuijsen, 2007), causing pressure sensors to underestimate observations. This effect is considerable for relatively short waves and large water depths. To compensate for this, an attenuation factor based upon linear wave theory can be applied as shown in equation 3.3, which considers both the wave number k [m^{-1}], mean water depth h [m] and sensor elevation with respect to the bed z_{sensor} [m].

$$S_w(f) = H(f)^2 = \left(\frac{cosh(kh)}{cosh(kz_{sensor})} \right)^2 \tag{3.3}$$

This retroactively amplifies wave induced pressure variations, restoring them in the surface elevation spectrum. To ensure only relevant wave band frequencies are restored, the factor is linearly tapered at higher frequencies. The tapering mask equals 1 until $f = 1.0Hz$, then linearly decreases to zero at $f = 1.5Hz$. This removes the variance from all frequencies above $f \geq 1.5Hz$, which mostly consist of unwanted noise in the spectrum. The mask also limits the value of S_w to a set maximum of 25, ensuring that energy in frequencies above that of the local wave field are not blown up (to infinity).
Figure 3.15 shows the attenuation factor before ($S_{w0}(f)$) and after ($S_w(f)$) tapering for a range of bursts at different average water depths. Larger water depths reach the cap of $S_w(f) = 25$ earlier at lower frequencies. Therefore the capped value, which does not follow linear wave theory, is applied across the widest range of frequencies at larger water depths during high tide.
As shown in equation 3.4, the corrected attenuation factor was applied to obtain the wave-corrected elevation variance spectrum: $S_{\eta,wave}(f)$ [m^2/Hz].

$$S_{\eta,wave}(f) = S_w(f) * S_\eta(f) \tag{3.4}$$

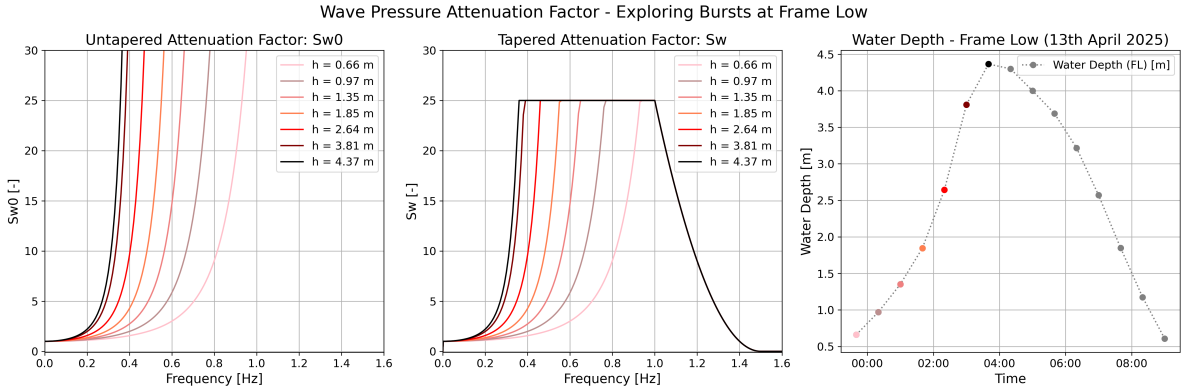

Figure 3.15: Pressure attenuation factor S_w with and without tapering for the full range of burst averaged water depths. Left: Raw attenuation factor $S_{w,0}$ explodes to infinity, making it unusable. Middle: Tapered Attenuation factor S_w is capped at 25 and tapers to zero for frequencies $f \geq 1.5Hz$. Right: Burst average water depths (h [m]) for a single tide on 13/04/2025.

3.7.2. Defining a bimodal frequency domain

Figure 3.16 plots the elevation variance spectra for all quality controlled, complete bursts per measurement frame. Observing the full spectra, distinct frequency bands could be identified which were divided by a low variance border at $f = 0.1Hz$. Therefore this was used to distinguish between low and high frequencies throughout the analysis.
The low frequency band contains thin peaks with large magnitudes, whilst the short wave domain is lower in magnitude but wider. These each show unique developments across the measurement frames. This together with the magnitude of the long wave domain confirms that a spectral approach holds potential to further understanding of wave and sediment dynamics on the GvB tidal flat.

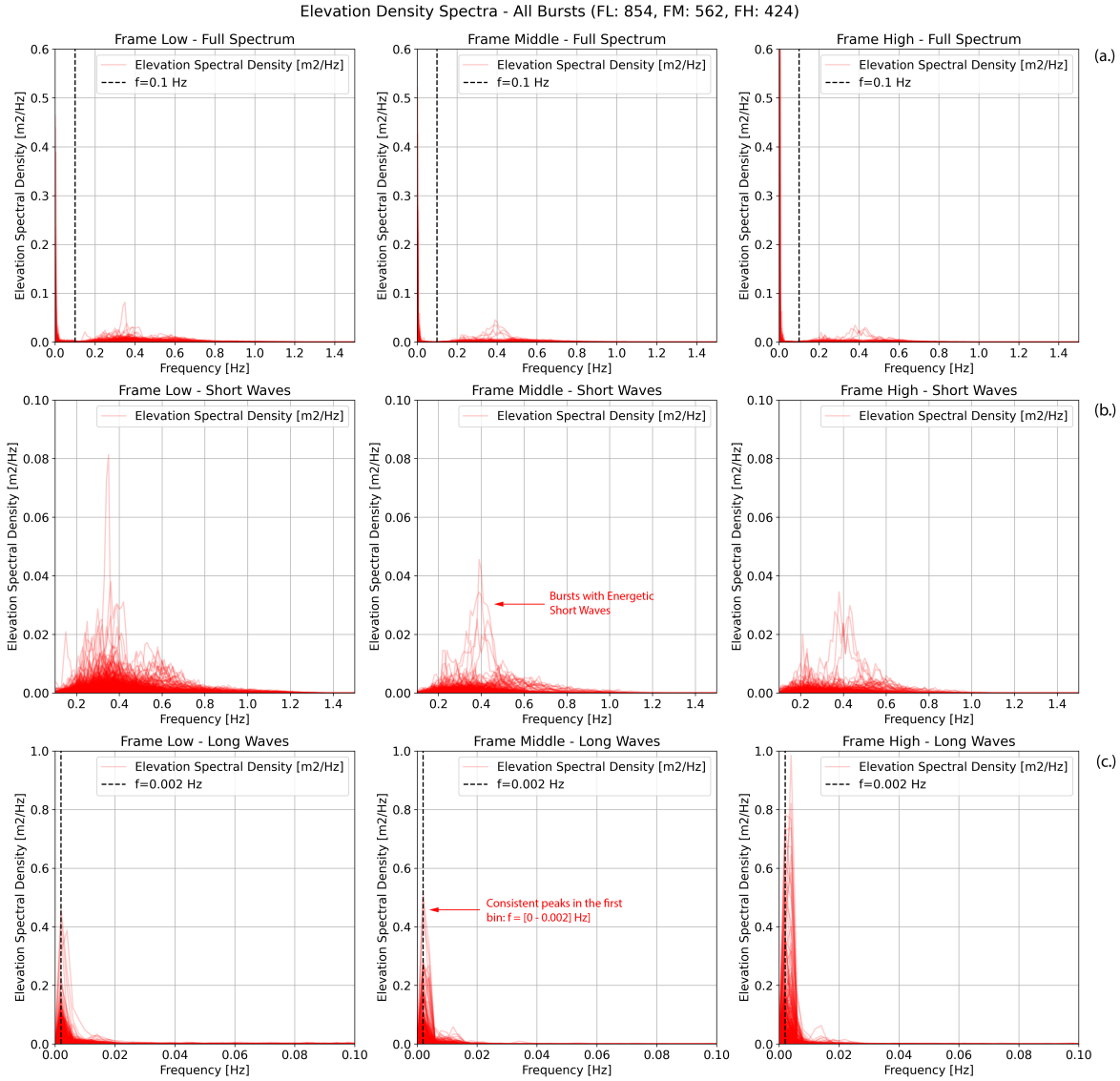

Figure 3.16: Overview of all elevation variance spectra per measurement frame (FL, FM, FH). Panel (a.): Full spectrum ($f = [0 - 1.5]Hz$). Panel (b.) Short wave band ($f \geq 0.1Hz$). Panel (c.) Long wave band ($f < 0.1Hz$).

To balance the reliability and resolution of the spectra, unique frequency resolutions were used for the low and high bands. For the low band ($f < 0.1Hz$), a higher resolution of $\Delta f = 0.002Hz$ was used to obtain more detail. The high band ($f \geq 0.1Hz$) was resolved with a resolution of $\Delta f = 0.01Hz$. Since the pressure was sampled with a sampling frequency of $16Hz$, the spectra were able to resolve components up to $8Hz$ considering the Nyquist frequency. However the applied attenuation factor removed all variance for $f > 1.5Hz$, making this the upper bound of the spectra.
Figure 3.17 presents a single surface elevation spectrum with unique frequency resolutions for the long and short wave bands. The (relatively energetic) burst was measured just after flow reversal at high tide, for the low measurement frame.

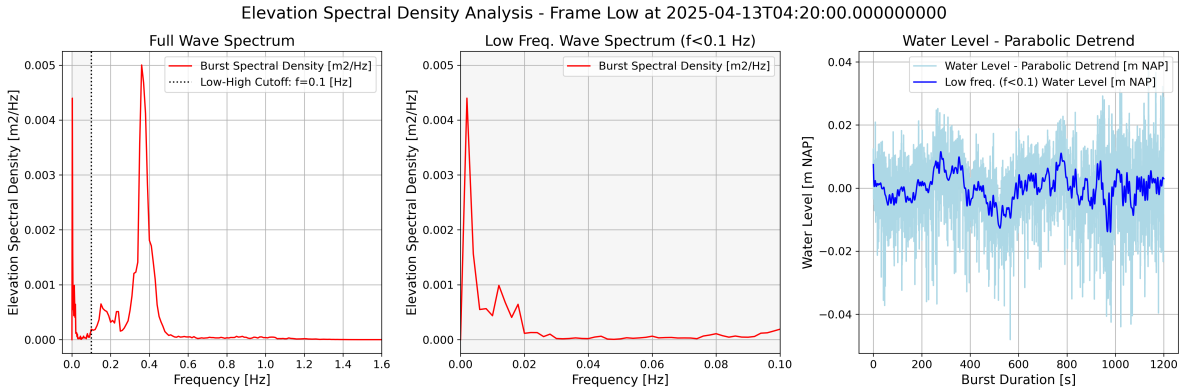

Figure 3.17: Left: Surface elevation variance spectrum for a 20 minute burst after high slack tide. Center: Surface elevation variance spectrum for the low frequencies (f<0.1Hz). Right: Surface elevation burst time series, with low frequency (f<0.1Hz) component highlighted in blue.

As shown in figures 3.16 and 3.17, the low frequency band spectra exhibited a consistent peak in the first bin ($f = [0 - 0.002]\ Hz$). This indicates an insufficient burst period. Variance from waves longer than the observed burst duration ($T = 20\ min$) was incorrectly allocated to the largest possible period in the spectrum.
To account for this, the first bin was discarded before further analysis. Effectively acting as a high-pass filter, this resulted in the low frequency domain being defined as $f_{low} = [0.003 - 0.1]\ Hz$. Interpreting this as a function of the burst period, it can be said that waves were only considered accurately captured if they were shorter than 28% of the burst period ($T < 5.6\ min$ for $T_{burst} = 20\ min$). Table 3.3 gives a summary of the final frequency ranges and resolutions used throughout the analysis for both elevation as well as velocity signals (sub-question 2).

Frequency Band	f_{low}	f_{high}	Δf	**Notation**
Full Spectrum	$0.003Hz$	$1.5Hz$	NA	m_0, H_{m0}, T_p, T_{m02}
Long Waves	$0.003Hz$	$0.1Hz$	$0.002Hz$	$m_{0,long}$, $H_{m0,long}$, $T_{p,long}$, $T_{m02,long}$
Short Waves	$0.1Hz$	$1.5Hz$	$0.01Hz$	$m_{0,short}$, $H_{m0,short}$, $T_{p,short}$, $T_{m02,short}$

Table 3.3: Summary of the defined bimodal frequency domain with unique long and short wave frequency resolutions (Δf). Full spectrum parameters are noted with no subscript, long and short wave parameters are presented with their respective subscript.

3.7.3. Spectral Wave Parameters

With the elevation variance density spectra computed, the significant wave height H_{m0} $[m]$ and mean zero-crossing period T_{m02} $[s]$ were determined using the spectral moments for each burst, as shown in equations 3.5, 3.6 and 3.7 (Holthuijsen, 2007). Peak period T_p was also examined, by selecting the burst frequency bin with highest variance density. These parameters provide a general overview of the observed wave field.

$$H_{m0} = 4\sqrt{m_0} \tag{3.5}$$

$$T_{m02} = \sqrt{\frac{m0}{m2}} \tag{3.6}$$

$$m_n = \int_{f_{low}}^{f_{high}} f^n S_{\eta,wave}(f) df \quad \text{for } n = ..., -3, -2, -1, 0, 1, 2, 3, ... \tag{3.7}$$

Since many bursts exhibited significant low frequency oscillations, both the low ($f < 0.1Hz$) and high ($f \geq 0.1Hz$) frequency bands of the spectra were examined individually. The evolution of spectral wave parameters was considered for both low and high frequencies across the measurement frames. Furthermore, the total burst variance (m_0) was examined by integrating the obtained spectra across the defined frequency ranges [$f_{low} - f_{high}$], then comparing the relative contribution by the low and high frequency domains ($m_{0,low}/m_0$ and $m_{0,high}/m_0$). This made it possible to highlight when and where short and long waves could be relevant for tidal flat morphodynamics.

Finally, to determine the linearity of the incoming wave field, the Ursell number was computed for a burst characteristic wave with significant wave height H_{m0} and mean zero-crossing period T_{m02}. This was also done for the short and long wave fields. Equation 3.8 illustrates the computation of the Ursell number, which can qualitatively be described as the ratio of the wave steepness to the relative water depth cubed. The higher the Ursell Number, the more non-linear behaviour can be expected of the wave field (Holthuijsen, 2007).

$$N_{Ursell} = \frac{H/L}{(d/L)^3} = \frac{HL^2}{d^3} = \frac{H_{m0}(2\pi)^2}{d^3k^2} \tag{3.8}$$

3.8. Examining wave orbital velocities and bed shear stress in relation to SSC (SQ2)

To describe the forcing that waves induce on the tidal flat, it is important to determine the wave orbital velocities that reach the bed. These interact with the tidal currents across the flat, generating patterns of bed shear stresses that suspend sediments. The relation between observed wave heights and near bed velocities was investigated by comparing the development of root mean squared 2D bed velocities u_{rms} [m/s] to that of H_{m0} [m]. Following the approach of sub-question 1, low and high frequency bands were analysed to determine the influence of long and short waves on near bed velocities.
Wave induced bed shear stresses τ_w [Pa] were computed with the variation of peak orbital velocities U_w [m/s] and wave friction factor f_w [$-$]. With this approach it was possible to understand how the incoming wave field stirred the bed, and how this is influenced by changing water depths, tidal currents and wind. Higher bed shear stresses are expected to induce larger SSC responses across the tidal flat. By comparing the development of wave driven bed shear stresses to the observed SSC signal [g/l], it was possible to infer to what extent waves were able to erode the bed and entrain sediments in the water column.

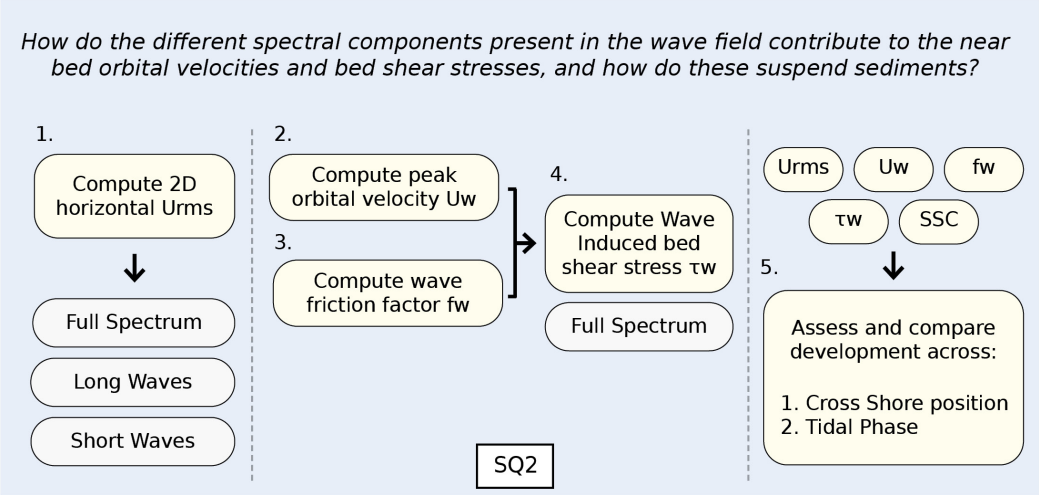

Figure 3.18: Flowchart presenting the utilised method to answer sub-question 2.

3.8.1. Near bed Horizontal Root-Mean-Squared Velocity

The horizontal root mean squared velocity describes the magnitude of flow velocity in the horizontal plane (u, v axes). The ADV measurement volumes were positioned at 15cm from the bed, giving a good indication of the velocities stirring the bed of the GvB tidal flat. Although south westerly waves were expected to mostly travel along the cross shore axis (u), it is important to consider waves from the full range of potential directions. Thus wave induced velocities were considered in both horizontal axes ($u(t)$ and $v(t)$).

To isolate the relation between observed wave heights and the wave driven horizontal velocities, both velocity signals were parabolically detrended and had their mean removed. Figure 3.19 provides an example of the time series pre-processing, considering the same burst as for the elevation example in sub-question 1 (Ebb tide just after slack).

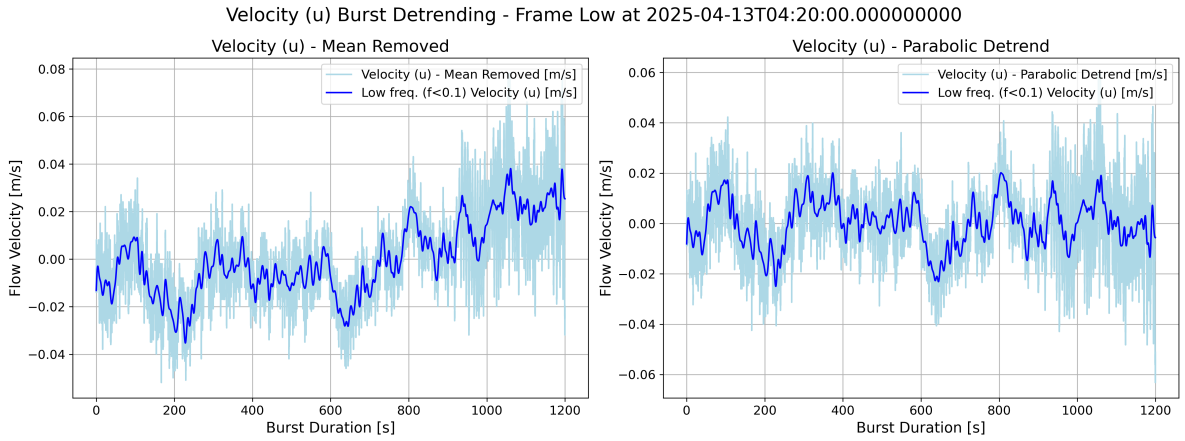

Figure 3.19: Example of undertaken processing steps for cross-shore velocity time series $u(t)$ $[m/s]$. Left: Cross-shore velocity time series with mean removed. Right: Parabolically detrended cross-shore velocity time series.

To ensure both elevation and velocities were considered across the same frequency range, a bandpass filter was applied to extract the frequencies between $f = [0.003 - 1.5]\ Hz$. Finally, to reach a suitable comparison between u_{rms} and the burst significant wave height H_{m0}, the burst averaged value was considered as shown by the angled brackets in equation 3.9.

$$u_{rms} = \sqrt{\langle u(t)^2 + v(t)^2 \rangle} \tag{3.9}$$

Long and short wave near bed velocities were extracted as well, applying bandpass filters according to the frequency bands defined in section 3.7.2. These were then inserted into equation 3.9 to obtain the 2D long and short wave u_{rms}.
As for the surface elevation, variance was be used to consider the relative contribution of the long and short wave components to the total 2D near bed velocity field. Ultimately this approach answers the question: ”How much of the observed velocity variance is explained by the low/high frequencies?”. This mirrors the approach of sub-question 1, making the comparison between surface elevation and velocity variance possible. Acknowledging that total variance (m_0) equals the average of the mean-removed squared signal (equation 3.10), the ratios of squared u_{rms} were determined as shown in equation 3.11.

$$m_0 = u_{rms}^2 \tag{3.10}$$

$$\textit{Short wave contribution: } \frac{u_{rms,short}^2}{u_{rms}^2} \qquad \textit{Long wave contribution: } \frac{u_{rms,long}^2}{u_{rms}^2} \tag{3.11}$$

3.8.2. Wave induced bed shear stress

By comparing the development of wave driven bed shear stresses to observed SSC signals, the approach quantified how long and short waves suspend sediments from the bed on the GvB tidal flat. This was done by comparing burst averaged SSC ($\langle SSC \rangle$) to the burst averaged wave driven bed shear stress. The (wave cycle averaged) wave induced bed shear stress τ_w [Pa] is influenced by the peak orbital bed excursion A_w [m], peak bed orbital velocity U_w [m/s] and wave friction factor f_w [-] as shown in equation 3.12 (van Rijn, 1993).

$$\tau_w = \frac{1}{4}\rho_w f_w U_w^2 \tag{3.12}$$

The peak bed orbital velocity U_w is different to the root-mean-squared velocity u_{rms}, as it defines a maximum orbital velocity induced by a single characteristic wave, and is computed based upon linear wave theory as shown in equation 3.13. In this approach the wave spectral parameters H_m0 and T_{m02} were used for wave height and period respectively of an irregular wave field, following the method of Q. Zhu et al. (2016). Using a burst characteristic wave for U_w, equation 3.12 now describes a burst averaged wave driven bed shear stress: $\langle \tau_w \rangle$.

$$U_w = \omega A_w = \frac{\pi H_{m0}}{T_{m02} sinh(kh)} \tag{3.13}$$

The ADV velocity observations were not used in this approach, as defining the peak orbital velocity within these records becomes complex. However, comparing the development of peak orbital velocity (based on pressure measurements) to the horizontal u_{rms} (based on velocity measurements) constitutes a convenient control to confirm consistent observations between pressure and ADV instruments.

4

Spectral Wave Climate Analysis

The following chapter presents the obtained results from the spectral wave climate analysis, using the method as described in chapter 3. First a general overview is presented, highlighting qualities of the observed full wave spectrum and SSC response during the selected south-west wind event. Then the short and long wave bands are characterised across their respective frequency bands with spectral wave parameters. Finally the observed wave field is examined in light of changing water depths, tidal currents and wind climate. These results are presented to answer the first sub-question: *How do wave transformations take place across spectral components in the wave field on a muddy tidal flat under varying water levels, tidal currents and wind forcing?*.

4.1. Time Window Selection

With the time series, spectra and burst parameters prepared, the window of analysis could be selected. Initially, the process started by considering wind observations from the KNMI meteorological station in Vlissingen (15km from the GvB tidal flat). Extracted wind speeds and direction are shown in figure 4.1.

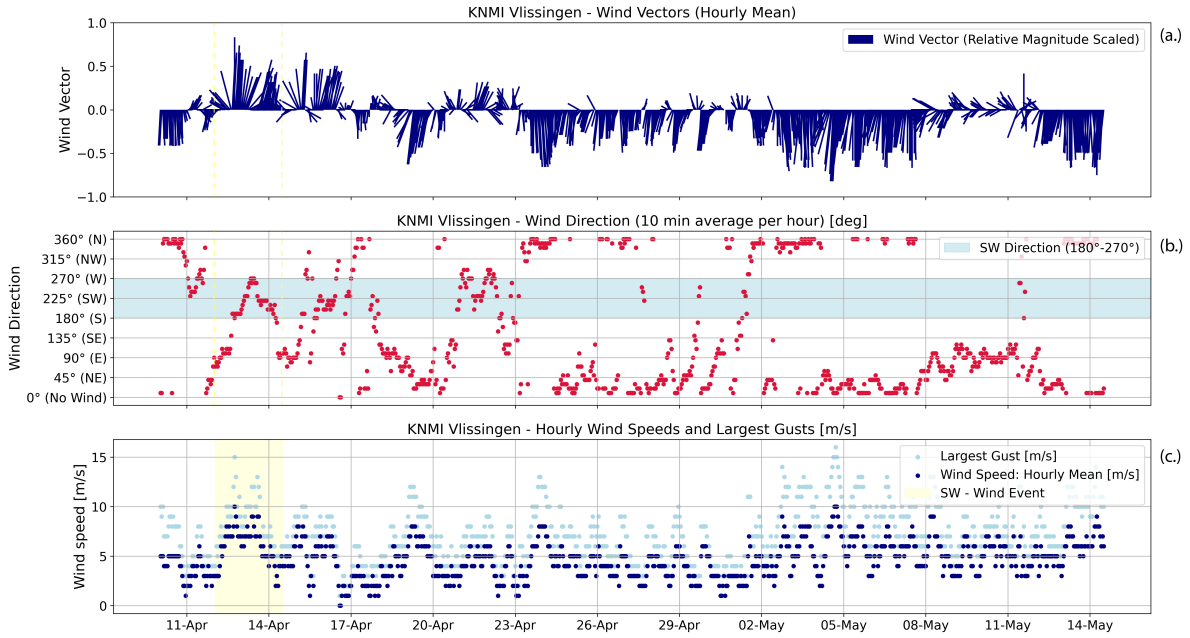

Figure 4.1: Wind analysis using hourly measurements from the KNMI Vlissingen meteorological station. (a.): Magnitude scaled hourly wind vectors (b): Hourly wind direction in degrees, South-West direction highlighted in light blue. (c.): Hourly wind speed (blue) and hourly largest gust (light blue) in m/s, with south-west wind event highlighted in yellow.

Using the observations presented in figure 4.1, it was possible to identify periods in which wind induced waves were expected to be most prevalent. Wind speeds and direction were considered, looking for moments with relatively high wind speeds from the south-west. These conditions were expected to generate the largest waves across the tidal flat.
South-westerly winds are rather uncommon, and wind speeds remain relatively stable around 2-6 m/s for the majority of April and then increase to 4-8 m/s in May. Despite this, there was a south-west wind event from the 12th (00:00 AM) till the 14th (12:00 PM) of April with wind speeds reaching 8-10 m/s. Satisfying both direction and magnitude, this period was selected for further analysis expecting the most energetic waves.

To confirm the effect of the identified south-west wind event, both the full spectrum significant wave height and burst averaged SSC signal are plotted in figure 4.2. The wind event is highlighted in yellow, and it is clear that the increased wind speeds in south-west direction led to larger waves on the GvB tidal flat. The SSC response is less obvious as it tends to follow the spring neap tidal cycle according to the magnitude of the tidal range. Despite this, the wind event does appear to contain a number of significant peaks in mean SSC across all three measurement frames, which is otherwise rarely observed.

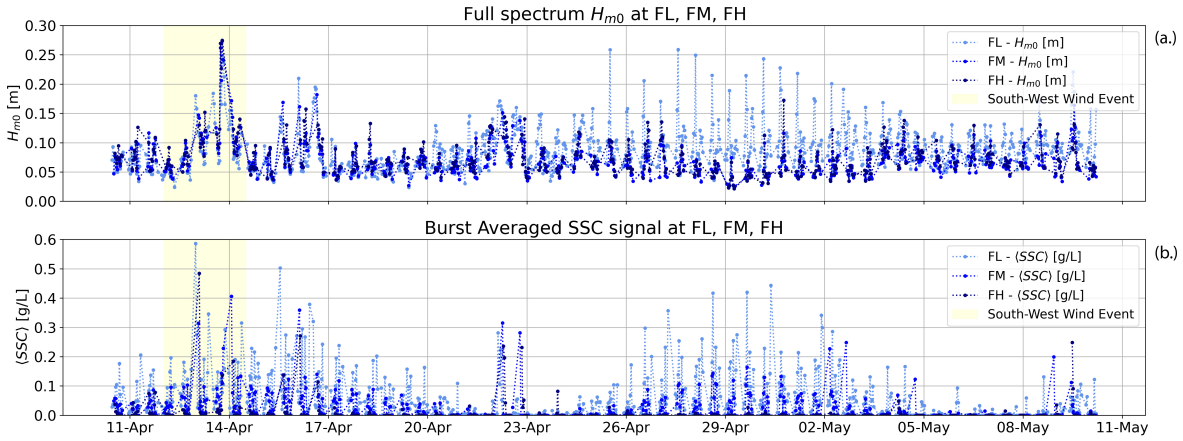

Figure 4.2: Full spectrum H_{m0} $[m]$ and burst averaged SSC $[g/L]$ during the 1 month measurement period. South-west wind event is highlighted in yellow from 00:00 12/04/25 till 12:00 14/04/2025.

The chosen wind event is highlighted in figure 4.3 which gives an overview of the processed tidal signals for each measurement frame. Here it can be seen that the wind event is present for five tidal cycles during spring tide. The selected tides generally exhibited a tidal range of -2.00 to +2.50 m NAP, however the lower tidal range was not explicitly captured due to the emergence of the pressure sensors. The study has focused on these five energetic tides to answer the three sub questions and conclude the main research objective.

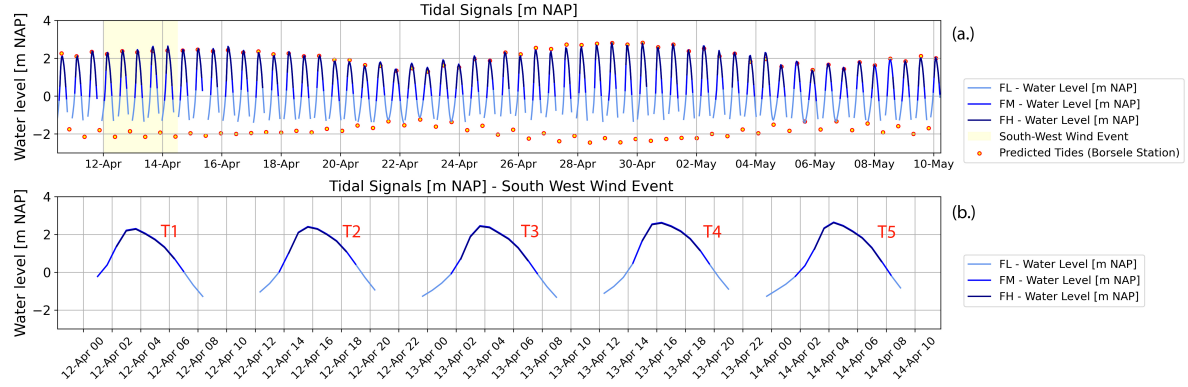

Figure 4.3: Burst averaged tidal elevation signals. (a.): Pre-processed tidal signals. Selected south-west wind event (00:00 AM 12/04/2025 - 12:00 PM 14/04/2025 UTC +2) is highlighted in yellow. (b.): 5 tides during the selected south-west wind event.

4.2. Full Spectrum Wave Observations and Mean SSC Response

Figure 4.4 characterizes the full wave spectrum with general hydrodynamic observations and presents the burst averaged SSC response during the selected south-west wind event. In panel (a.), the five spring tides exceed 4 meters water depth at FL, where waves are most prevalent on tides T3, T4 and T5. This is shown by the increase in H_{m0} which peaks at $H_{m0} = 0.27m$ during the start of ebb at tide T4. The mean SSC response also increases on tides T3, T4 and T5. However this is only shown during the beginning of flood and end of ebb. At high tide the SSC response is relatively small, and does not change depending on the presence of waves.

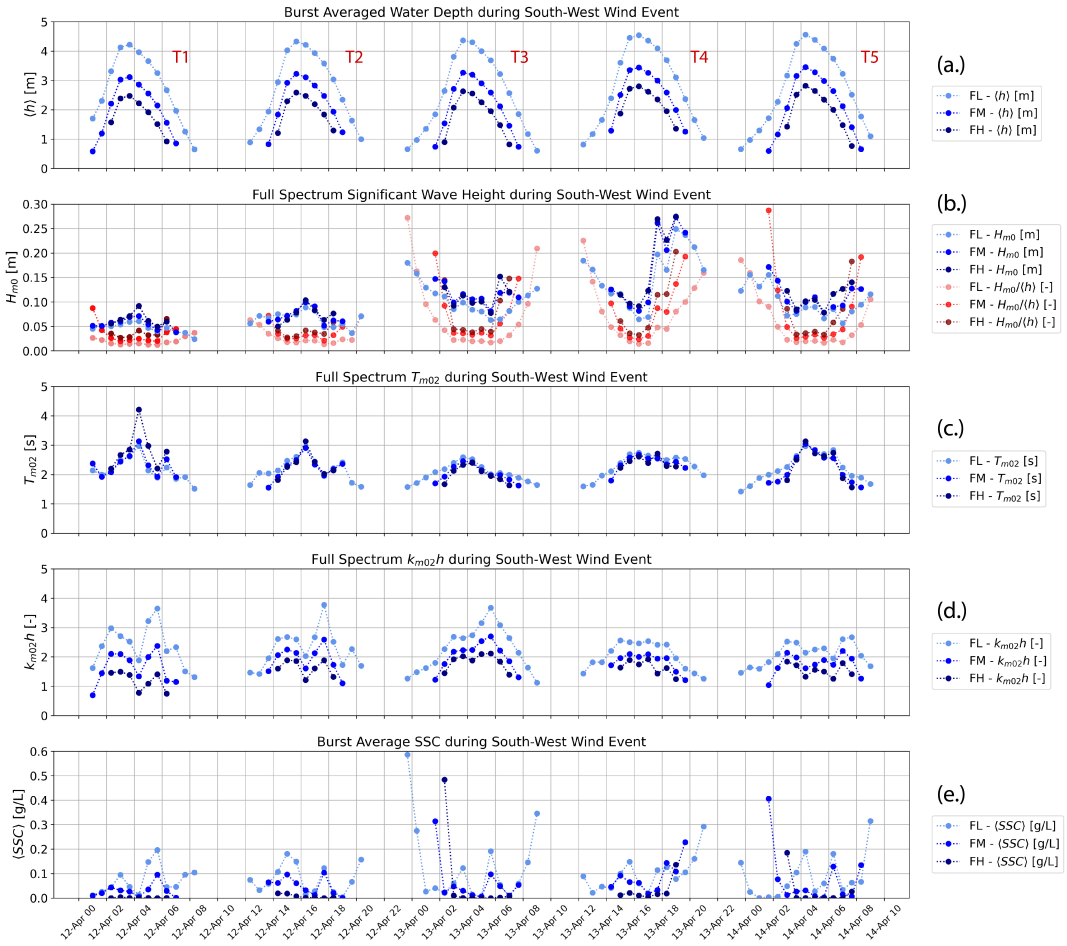

Figure 4.4: Full spectrum wave observations and burst averaged SSC response during the south-west wind event. Panel (a.): burst averaged water depth $\langle h \rangle$ $[m]$. Panel (b.): Full spectrum significant wave height H_{m0} $[m]$ and $H_{m0}/\langle h \rangle$ [-]. (c): Full spectrum mean zero down-crossing period T_{m02} $[s]$. Panel (d.): Full spectrum $k_{m02}h$ [-]. Panel (e.): Burst averaged suspended sediment concentration $\langle SSC \rangle$ $[g/L]$.

Significant wave heights appear relatively constant across the cross shore transect, with FL, FM and FH showing similar values at each stage of the tide. Looking with more detail at tides T3, T4, T5 the wave heights seem to show a slight shoreward increase between the measurement frames. Across tides T3, T4 and T5 the wave heights are largest for the smallest water depths, as shown by the convex shape of the H_{m0} plots in relation to the concave water depths.
Comparing the significant wave heights to water depths, it is obvious that the tidal range overshadows the magnitude of variations in wave heights. Furthermore the typical breaker limit of $H = 0.78h$ is never reached, indicating that depth limited breaking does not occur on the tidal flat (Holthuijsen, 2007). In panel (b.), the red trends of $H_{m0}/\langle h \rangle$ show how waves at each cross-shore location exist in different depth conditions. The same wave height will be in shallower water higher on the tidal flat. Thus the same waves may be able to exert more forcing on the bed at shallower water depths.

The full spectrum mean zero down-crossing period T_{m02} is shown in panel (c.). Generally this varies between 1.5 and 3 seconds, and tends to increase with water depth, peaking around high tide. There is little cross-shore variation, with all measurement frames exhibiting consistent values per water depth. To assess the degree to which wave orbital velocities reached the bed, $k_{m02}h$ was determined using T_{m02} in the dispersion relation. The results are shown in panel (d.), and mostly lie within the intermediate water range ($0.31 - \pi$). As water depths decrease, so does $k_{m02}h$, indicating that wave orbital velocities are more able to reach the bed.
The patterns in burst averaged SSC respond inversely to the trend in $k_{m02}h$, as more suspended sediments are measured for smaller water depths where waves are able to reach the bed more effectively. Wave heights alone do not show the same response in $\langle SSC \rangle$, exemplified by the low concentrations during the peak of $H_{m0} = 0.27m$ in tide T4.

The $\langle SSC \rangle$ signal closely follows the trends in $H_{m0}/\langle h \rangle$ across all measurement frames with peaks at the start of flood and end of ebb. This, together with the negative response of $\langle SSC \rangle$ to $k_{m02}h$ suggests that water depth strongly controls the degree to which waves are able to stir sediment. This is a defining quality of a turbid fringe, which is a commonly identified phenomenon in tidal flat systems (Green & Coco, 2014). The presence of which can be further investigated by exploring the development of bed orbital velocities and shear stresses on the GvB tidal flat.

4.3. Short Waves

Considering the spectra as shown in figure 3.16, local wind driven waves constitute the majority of the wave field. These short waves were selected by considering all frequencies $f = [0.1 - 1.5]Hz$ within the burst spectra. Panel (a.) of figure 4.5 examines the peak period of each burst. Very short waves are most energetic during the wind event, with most peak periods lying between $T_{p,short} = 2 - 4s$. The mean zero-crossing period $T_{m02,short}$ is naturally more steady, with panel (b.) showing values close to 2 seconds for all five tides. Interestingly, $T_{m02,short}$ appears to follow the tidal signal as water depths rise and fall.
The short wave depth regime was investigated by computing $k_{m02,short}h$ for each burst using $T_{m02,short}$ in the dispersion relation. This reveals that nearly all the short waves were within intermediate water, where orbital velocities are partially attenuated whilst still reaching the bed. Using $H_{m0,short}$ and $T_{m02,short}$ for each burst, the Ursell number was computed as shown in panel (d.). The extremely low values ($N_{ursell,short} \approx 1$) confirm the linear nature of the short wave field. This is to be expected for the relatively large water depths (1-4 meters) with waves of 2-4 seconds and wave heights of 5-20cm. The linear nature suggests that most short waves did not exhibit significant skewness or asymmetry, therefore these processes are unlikely to contribute significantly to sediment dynamics on the GvB tidal flat.

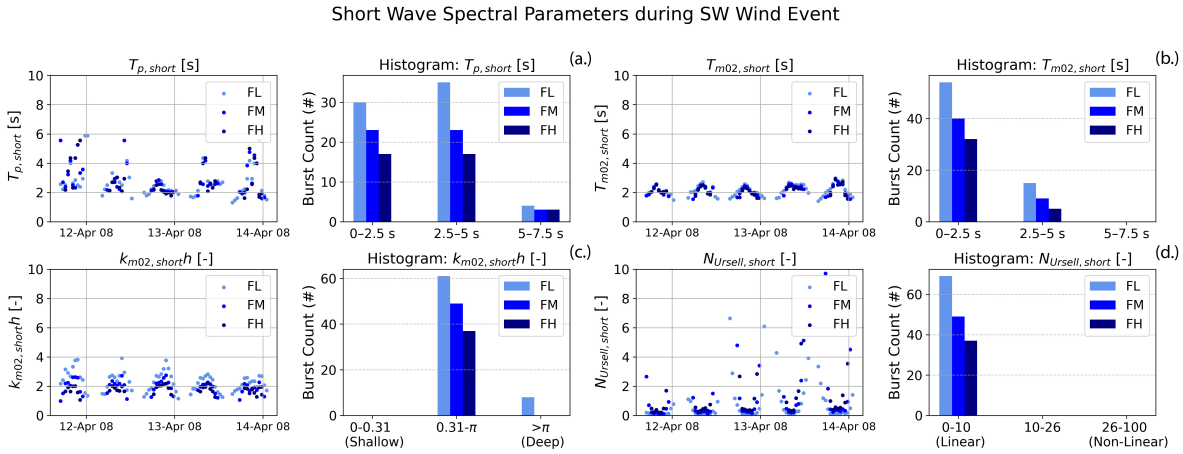

Figure 4.5: Overview of the short wave field during the south west wind event ($f = [0.1 - 1.5]Hz$) Panel (a.): $T_{p,short}$ [s] per burst. Panel (b.) $T_{m02,short}$ per burst. Panel (c.) $k_{m02,short}h$ per burst. Panel (d.) $N_{Ursell,short}$ per burst.

4.4. Long Waves

The obtained wave spectra consistently exhibited peaks of variance below $f < 0.1Hz$, indicating the presence of long waves in the wave field. Figure 4.6 illustrates the same spectral parameters per burst ($T_{p,long}$, $T_{m02,long}$, $k_{m02,long}h$, $N_{Ursell,long}$) for the long wave domain: $f = [0.003 - 0.1]Hz$.
As stated in the methodology, some long waves exceeded the selected block length ($N = 500s$ for $\Delta f = 0.002Hz$), causing spectral leakage into the first bin. Observing the peak periods in panel (a.) it is clear that after the (discarded) first bin, the second bin received most variance ($T_{p,long} = 250s$ for $f = 0.004Hz$). The distribution of peak periods show that spectral leakage affected the first two bins. Ultimately the analysis shows that there were waves longer than 500s in the wave field, however these could not be characterized accurately.

The $T_{m02,long}$ period in panel (b.) provides a more general description of the long wave field with values ranging between $T_{m02,long} = 25s$ and $T_{m02,long} = 150s$. Contrary to the short waves, there appears to be no clear relation between T_{m02} and water depth for the long wave field. These long periods result in smaller $k_{m02,long}h$ values as shown in panel (c.), where all of the observed long waves are classified in shallow water. These results indicate that the long wave induced orbital velocities should reach the bed more effectively, potentially holding a larger influence on sediment suspension at the bed.
Panel (d.) shows the Ursell number of the long wave field. Contrary to the short waves, a large portion appear to be non-linear in nature. Especially the highest frame (FH) exhibited mostly non-linear long waves, characterized by $N_{ursell,long} > 26$. Despite the highest frame capturing the smallest number of waves due to its shorter inundation period, the frame also captured the most long waves with $T_{m02,long} = 60 - 150s$.

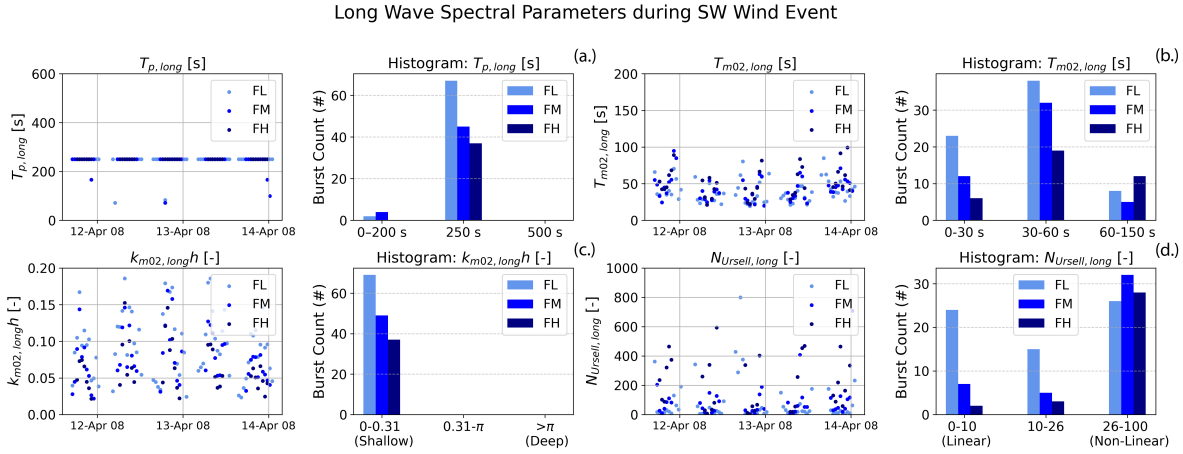

Figure 4.6: Overview of the long wave field during the south west wind event ($f = [0.003 - 0.1]Hz$) Panel (a.): $T_{p,long}$ per burst. Panel (b.) $T_{m02,long}$ per burst. Panel (c.) $k_{m02,long}h$ per burst. Panel (d.) $N_{Ursell,long}$ per burst.

Limits to T_{m02} for a non-Gaussian long wave field

Unlike the short wave field, the long wave surface elevation cannot certainly be considered a Gausian process. Its smaller frequency range contains significantly less components, which furthermore are more non-linear in nature (Holthuijsen, 2007). In light of this, T_{m02} no longer describes the mean zero-crossing period of a burst elevation time series. To still achieve this, a wave-by-wave analysis could be conducted, yet this was not considered within the scope of this research.
Despite these limitations, the use of $T_{m02,long}$ can still generally describe how surface elevation variance is distributed across frequencies in the long wave domain.

4.5. Long and Short Wave Burst Variance

Insufficient block duration and spectral leakage diminish the physical meaning of the obtained long wave spectral parameters. Since an accurate analysis is not certain using these parameters, the assessment was continued considering the total variance. Total burst variance can represent the prevalence of long waves, without having to indicate at what frequencies they are present. Figure 4.7 presents this analysis, considering the magnitude of the total, short and long wave surface elevation burst variance (m_0, $m_{0,short}$, $m_{0,long}$ [m^2] respectively).

Panel (a.) shows the burst variance for the full spectrum at all three measurement frames. Naturally, the results closely follow the significant wave heights shown in figure 4.4 with more energetic waves in tides T3, T4 and T5 whilst tides T1 and T2 are relatively calm. The spike in variance during ebb of tide T4 constitutes the most energetic period during the selected south-west wind event.

Short waves make up most of the variance, however there is a large peak in long wave variance during ebb of tide T4 (see yellow highlight in figure 4.7). This isolated long wave event is independent of the short waves, suggesting that the two are not correlated.

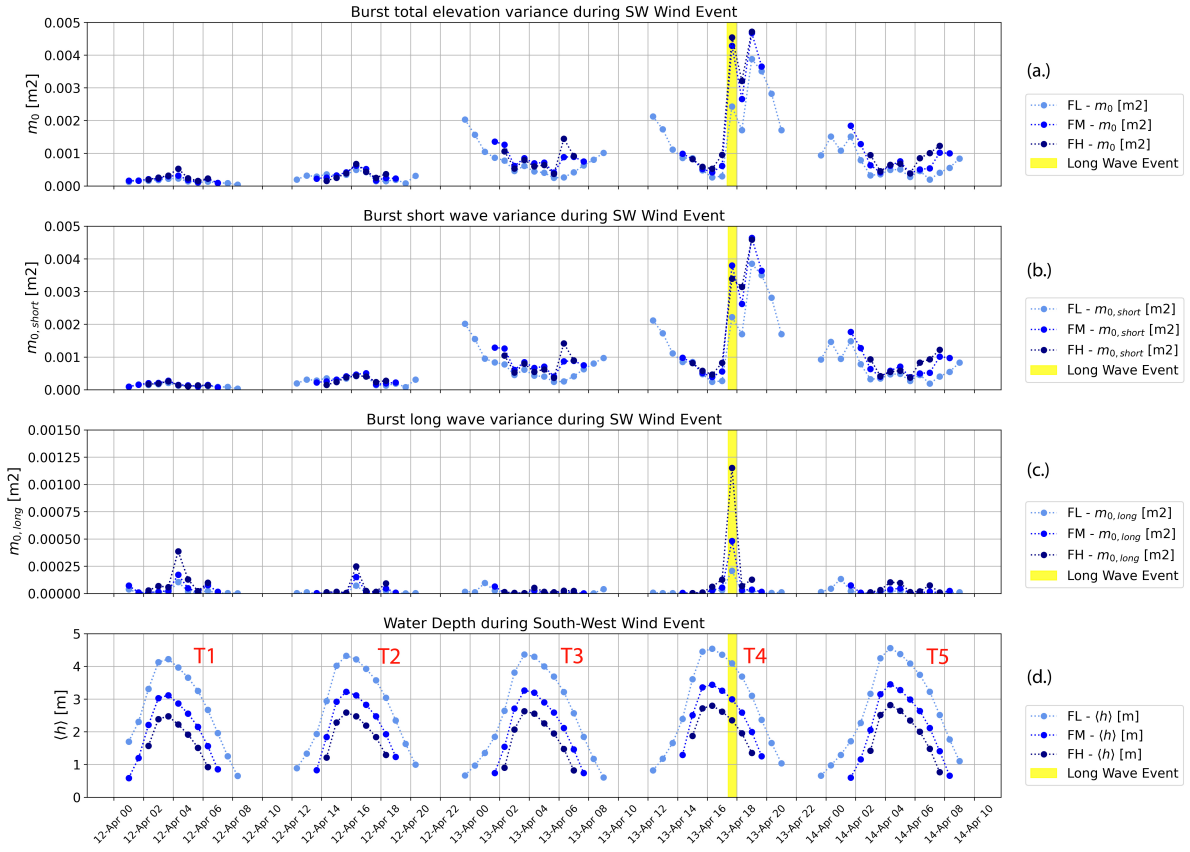

Figure 4.7: Magnitudes of burst elevation spectral variance during the south-west wind event. Panel (a.) Total variance per burst m_0 [m^2]. Panel (b.) Short wave variance per burst $m_{0,short}$ [m^2]. Panel (c.) Long wave variance per burst $m_{0,long}$ [m^2]. Panel (d.) Mean water depth [m].

To understand the relative contribution of each frequency band more clearly, their ratios have been visualised in figure 4.8. Here the short and long wave elevation variance ($m_{0,short}$ and $m_{0,long}$) has been plotted in relation to that within the total spectrum (m_0).

The wave spectra are clearly dominated by local short waves, making up at least 80% of the total variance across most of the five tides. The calmer tides T1 and T2 contained near negligible waves, which is reflected by the lower ratios of short wave variance.

Across all five tides a peak in long wave variance is seen during high water. This is especially pronounced just after slack tide of T4 where long wave variance is otherwise clearly surpassed by its short wave counterpart. During this energetic tide, the long wave variance amounts to 10% of the spectrum

total during high water and is seen to grow towards the shore. At the high measurement frame (FH), the long waves explain nearly 25% of the total surface elevation variance. This burst is again highlighted in yellow across the figure, and is of interest for further analysis.

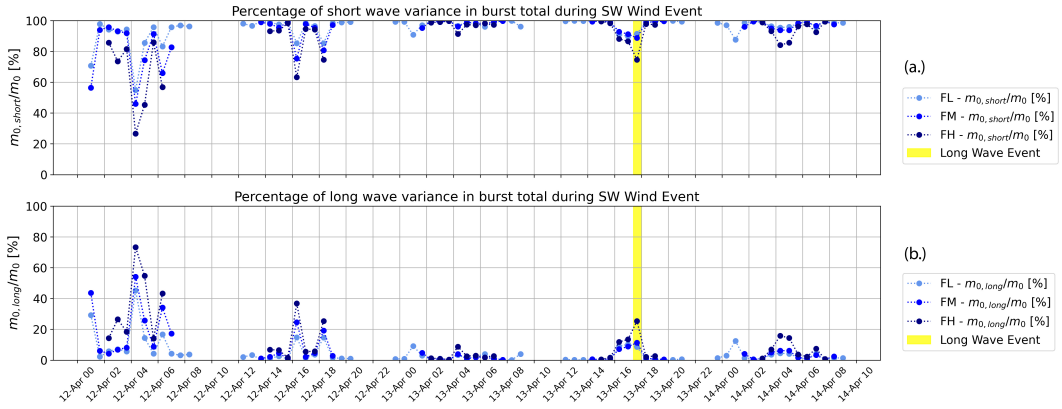

Figure 4.8: Relative contributions to burst elevation spectral variance during the south-west wind event. Panel (a.) Percentage of short wave variance in burst total $m_{0,short}/m_0$ [%]. Panel (b.) Percentage of long wave variance in burst total $m_{0,long}/m_0$ [%].

Figure 4.9 presents the 20 minute surface elevation time series $\eta(t)$ at each measurement frame during the long wave event. Across all frames there was a clear long wave oscillation. Initially the wave appears to exhibit a period near $T \approx 300s$, however later in the burst this stretches out and is less consistent. The amplitude of the long wave oscillation grows significantly between measurement frames. Starting at the low frame at $a \approx 0.1m$, it doubles to $a \approx 0.2m$ at the high frame. This follows the growth in long wave variance shown in figures 4.7 and 4.8.
The short wave oscillations maintain a relatively constant amplitude along the cross-shore, however a slight increase can again be observed towards the higher frames. There appears to be no clear phase difference between the long and short waves. The short wave field appears to travel on the long wave envelope, without any strong interactions between the two. This again suggests other long wave forms than infra-gravity waves.

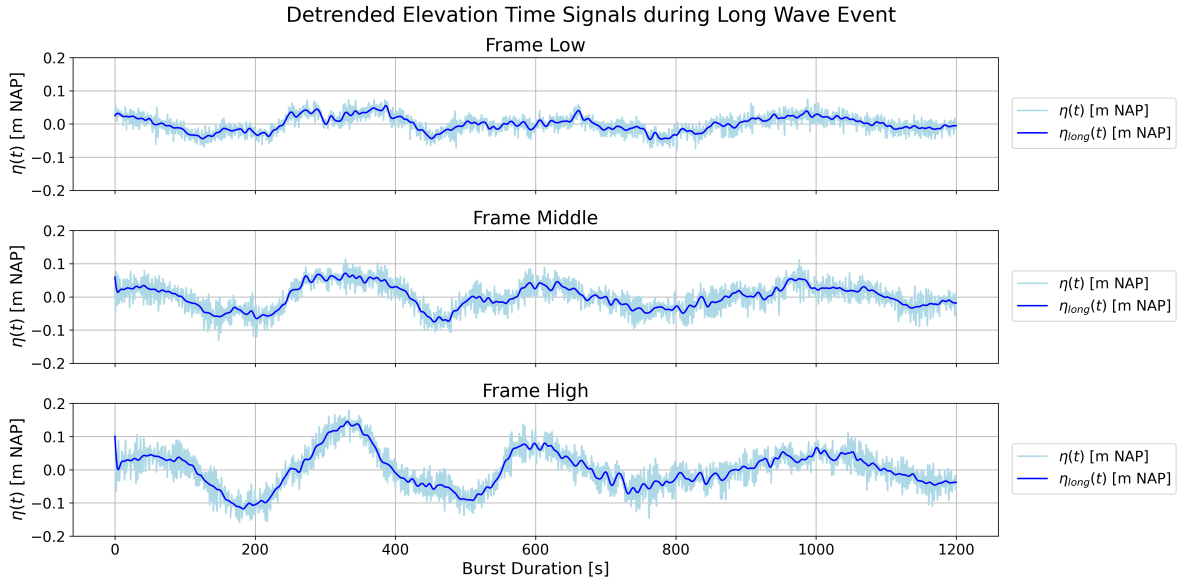

Figure 4.9: Elevation burst time series per measurement frame during the identified long wave event at ebb of tide T4 (13/04/2025 17:40:00). Signals have had their mean removed and have been parabolically detrended.

4.6. Short Wave Transformations under Varying Water Depths, Tidal Currents and Wind Climate

As seen in the variance assessment, local short waves tend to dominate the wave field, explaining the largest portion of surface elevation variance. Therefore it is important to understand how this frequency band transforms over the cross shore under influence of wind and tides.

The transformation of the short wave field under tidal influence is shown in figure 4.10 for the lowest measurement frame (FL). This was selected due to its longest inundation period, hence providing the largest range of observations. Here the development of significant wave height $H_{m0,short}$and mean spectral period $T_{m02,short}$ have been plotted for varying water depths and tidal currents (Flood, Slack, Ebb) during the five selected tides. Slack tides were identified considering the root-mean-squared 2D near bed velocity (without removing the mean current), and selecting all bursts between the flood and ebb peaks for which $u_{tide} \leq 0.2m/s$.

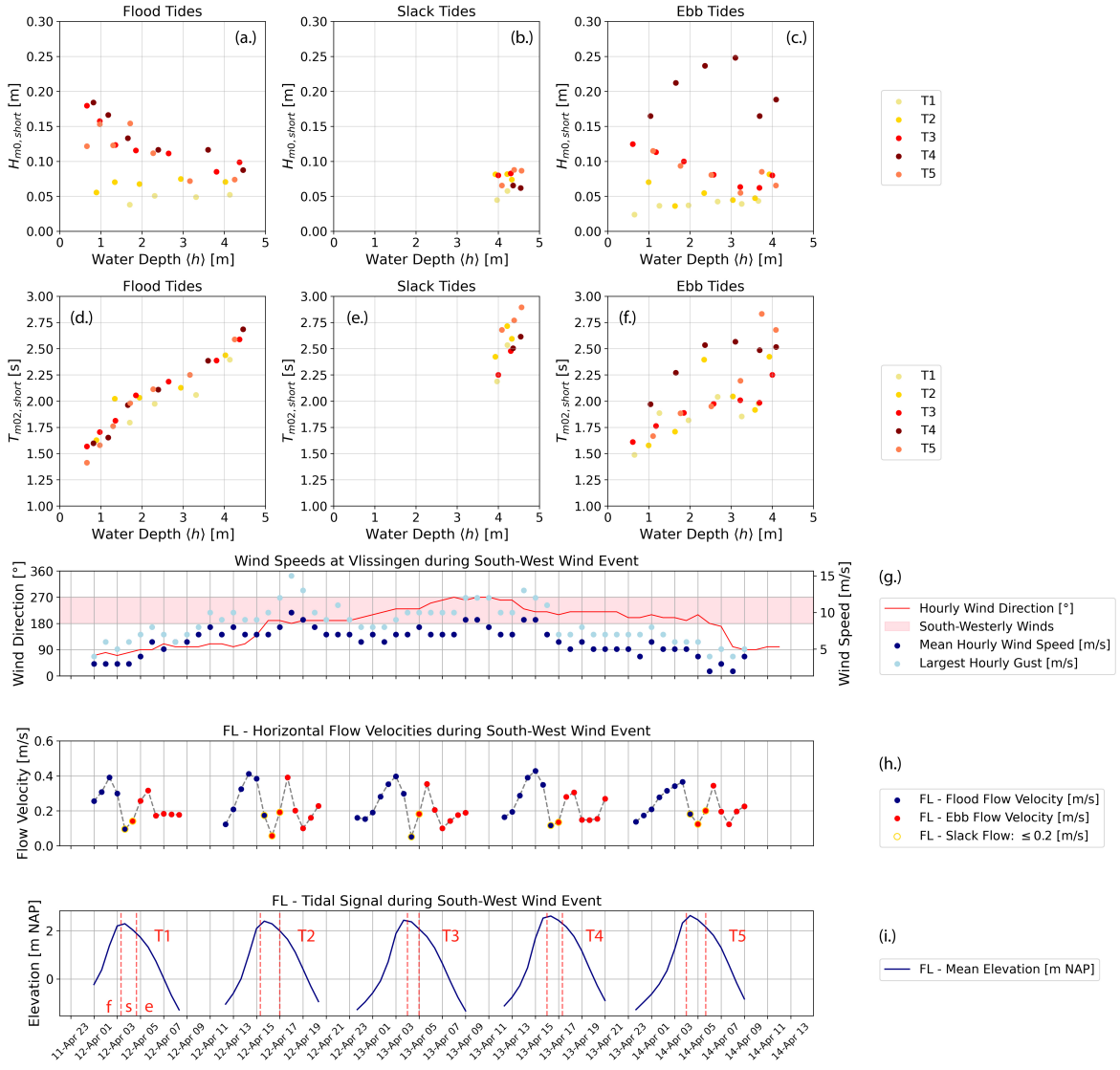

Figure 4.10: Short wave significant wave heights and mean spectral periods per water depth during flood, slack and ebb tides at frame FL. Panel (a, b, c): Significant wave height $H_{m0,short}$ [m] over water depth $\langle h \rangle$ [m] for five tides. Panel (d, e, f): Mean spectral period $T_{m02,short}$ [s] over water depth $\langle h \rangle$ [m] for five tides. Panel (g.): Wind speeds and direction from KNMI weather station in Vlissingen during SW wind event. Panel (h.): Horizontal flow velocities (2D burst u_{rms}) $[m/s]$ considering flood and ebb currents. Panel (i.): Mean elevation [m NAP] for 5 tides during south-west wind event

Short Wave Significant Wave Height

Examining significant wave heights first, a number of regimes can be observed. For calm tides T1 and T2, the near negligible wave heights of $H_{m0,short} \approx 0.05m$ were constant with depth. Tides T3, T4 and T5 show an unexpected negative relation between wave height and depth during flood. During ebb this was continued for tides T3 and T5, whilst T4 showed a mostly positive relation with growing wave heights for larger depths. Slack tides were characterized by small wave heights during large water depths across all 5 tides.
Considering panel (g.) of figure 4.10, south-westerly winds are seen during tides T3, T4 and T5 which explain the increased wave heights. The distinct wave height transformation during ebb of tide T4 cannot clearly be attributed to changes in wind speed. During tide T4 the wind speed remains relatively constant with $U_{wind} = 5m/s$, however the direction does appear to align more truly to the south west. This could explain the observed amplification.

The effect of tidal currents on wave height appears minimal, with comparable ranges of $H_{m0,short}$ between flood and ebb tides. The potential shoaling of waves under the ebb current is not observed, as wave heights are not seen to increase during ebb (except for T4). Looking at panel (h.), flood currents often reached a peak of $u_{flood} = 0.4m/s$, whilst ebb currents were slightly smaller. Both flood and ebb currents peaked at mid-tide and were smallest during flow reversal. At low tide both currents tended to flatten out, showing similar characteristics as found by Le Hir et al. (2000) on a range of tidal flats.
To properly assess the influence of tidal currents on wave transformations (such as shoaling), it would be critical to determine the magnitude of current in the wave direction and compare this to the group velocity c_g. A directional analysis is strongly recommended, yet fell outside the scope of this thesis.

Short Wave Mean Zero Down-Crossing Period

The mean spectral period $T_{m02,short}$ has a positive relation with water depth, showing larger wave periods for larger water depths during flood and ebb tides. High water slack tides exhibit the largest periods during the greatest water depths. This is contrary to linear wave theory, where wave period is preserved under changing water depths considering constant forcing.
However, in the case of mildly sloping tidal flats, water depth can exert large changes in available fetch. In turn this determines how large local wind waves can become, thus changing the incoming forcing (for a constant wind speed). Therefore, it is correct to see larger wave periods at larger water depths due to the increased fetch. Contrary to this, the observed short wave significant wave heights did not grow with water depth (and thus fetch). The only tide which saw both $H_{m0,short}$ and $T_{m02,short}$ grow with water depth (and thus fetch) was the ebb of tide T4.

The effect of tidal currents again appears minimal, with similar trends across flood and ebb tides for T_{m02} over depth. During ebb tides the relation between depth and T_{m02} is slightly more noisy, yet there are no physical processes to which this can be attributed.
The same analysis in figure 4.10 was conducted for measurement frames FM and FH. Their results are shown in Appendices A.1 and A.2. Generally there was little difference in response between cross shore locations. However there was a slight increase in wave heights across water depths for more onshore measurement frames. This growth was likely due to the shoaling of waves as they propagate onshore, as well as the increased fetch allowing winds to generate larger waves.

4.7. Observed Effect of Water Depth on Short Wave Heights

The observed relation between short wave heights and water depth is contrary to previous studies. As shown in figure 4.4, significant wave heights tended to decrease for larger water depths at high tide. Meanwhile as shown by Le Hir et al. (2000) on a mildly sloping mudflat in Brouage and by de Vet (2020) on the Zuidgors tidal flat in the Western Scheldt, larger water depths are able to facilitate larger wave heights on tidal flats.
Plotting the root mean squared wave heights H_{rms} [m] per water depth h [m] for each measurement frame, figure 4.11 is obtained. For all three locations, there is little variation in H_{rms} across water depth. Comparing the obtained figures to that of Le Hir et al. (2000), it appears that water depth exerts little control on wave height. This suggests that the observed wind forcing was trivial and thus unable to generate depth limited waves at the GvB tidal flat.

The identified limit of $H_{rms} = 0.15h$ by Le Hir et al. (2000) has been plotted in red. Considering their formulation based upon wave friction factor and bed slope as shown in equation 4.1, a local limit was derived for each location on the tidal flat. The slope at each measurement frame was determined by considering 50 meters of the cross-shore transect seaward and landward from the frame (100 meters total).

$$\left(\frac{H}{h}\right)_{lim} = \frac{15\pi}{4}\frac{\beta}{f_w} \tag{4.1}$$

These are plotted in maroon and indicate weaker attenuation by bottom friction at the GvB mudflat compared to the Brouage site. The weaker depth dependent attenuation factor further confirms the modesty of the wind conditions. In theory the GvB site should allow larger wave heights for a given water depth compared to Brouage.
Comparing the depth limits between measurement frames, it can also be observed that the higher frame (FH) is limited by stronger wave attenuation. This can be attributed to the milder slope compared to the low (FL) and middle (FM) frame locations.

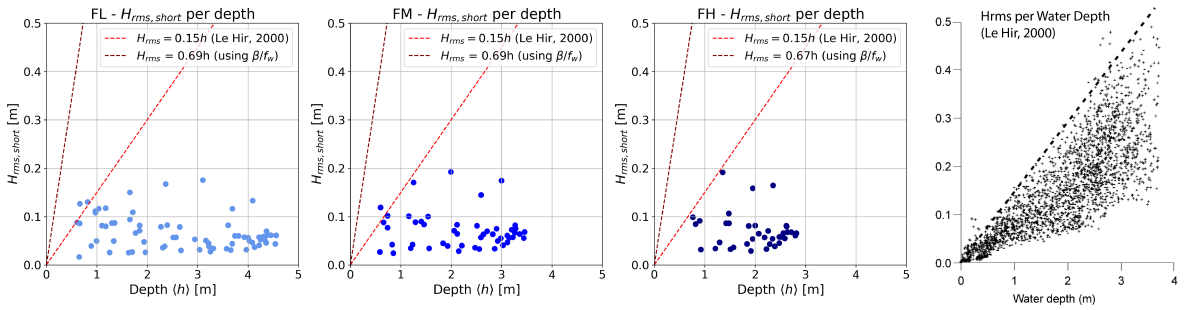

Figure 4.11: Left: Short Wave Root mean squared wave heights ($H_{rms,short} = H_{m0,short}/\sqrt{2}$) per water depth for each measurement frame (FL, FM, FH). Wave height attenuation criteria (in red) were determined with equation 2.11 per Le Hir et al. (2000). Right: H_{rms} per water depth at the Brouage mudflat (Le Hir et al., 2000).

4.8. Observed Effect of Wind Forcing and Fetch on Short Waves

During ebb of tide T4, significantly larger short wave heights were observed that coincided with a large long wave event. Interestingly, this was the only tide that exhibited the expected positive relation between short wave heights and water depths. Short wave heights were largest at high tide and decreased with the falling water level.
This sudden change in short wave height regime could not clearly be attributed to changes in observed wind speeds; these remained constant at $u_{wind} \approx 5$ $[m/s]$. Therefore a more detailed assessment was conducted to determine the influence of wind climate on the resulting wave field. Figure 4.12 plots the root-mean-squared short wave heights $H_{rms,short}$ $[m]$ against wind speed for each measurement frame, where panel (a.) classifies data points by wind direction and panel (b.) by water depth.

Wind direction is seen to influence the incoming wave field. Short wave heights are largest for winds that are most truly from the south-west (225°). Considering the orientation of the GvB tidal flat, waves are expected to enter the flat most effectively at this angle.
Ultimately the impact of wind direction can be attributed to fetch length. As more favourable wind directions will generate waves that can develop across a longer fetch. According to Le Hir et al. (2000), wave heights approximately increase by the square root of the fetch length for a fixed wind speed. The influence of fetch on short wave heights can also be inferred from figure 4.11. Wave heights are generally seen to grow slightly between the low and high measurement frames across all wind speeds. Apart from potential shoaling, this trend indicates that increased fetch length may have allowed for waves to grow more under the same wind conditions.

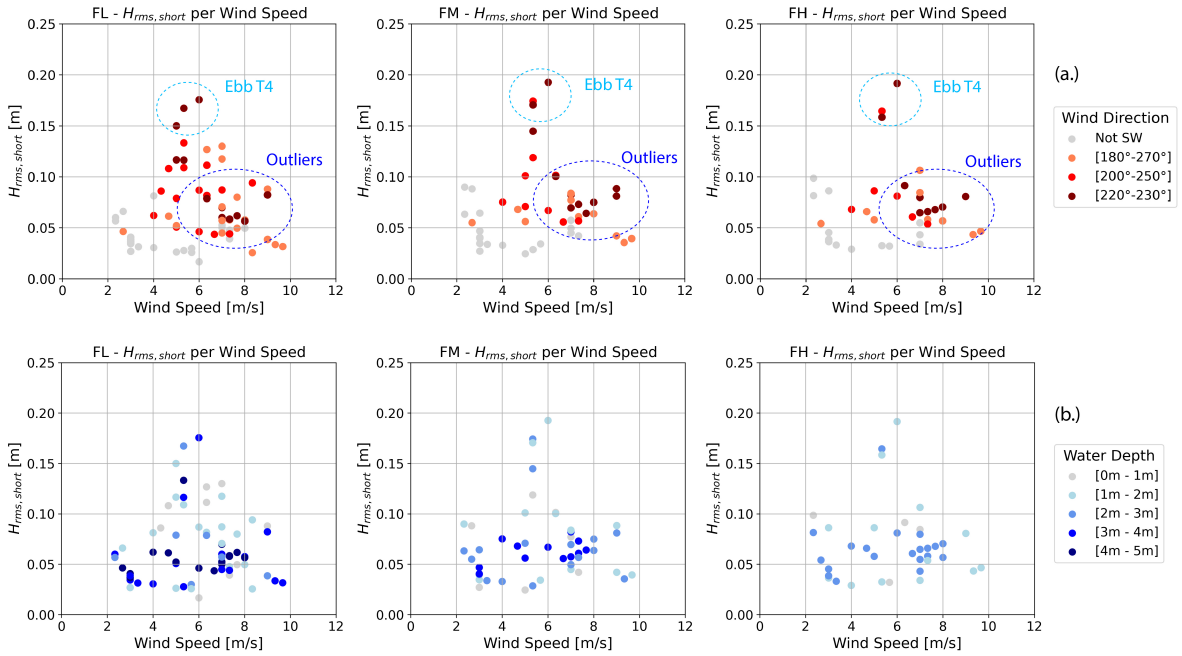

Figure 4.12: Root mean squared wave height [m] per wind speed [m/s] during the south west wind event for each measurement frame. Panel (a.): Data points coloured by wind direction [deg]. Darker red indicates a more true south-west wind direction (closer to 225). Panel (b.): Data points coloured by water depth [m]. Darker blue describes deeper water.

Interpreting Outliers

The relation between wind speed, fetch and short wave heights is not unexpected. However a number of outliers can be detected, where increased wind speeds in a favourable south-west direction did not generate larger short waves. Viewing these outliers in panel (a.) and comparing them to the same data points in panel (b.), it is hard to confirm an influence of the water depth. For frame FL, the outliers appear to occur for larger water depths, yet when viewing frame FH, these same outliers remain for much smaller depths. This is in line with the analysis of figure 4.11, where water depths exerted little control on wave heights.

Apart from the bursts during ebb of T4 which reach $H_{rms} = 0.15m - 0.20m$, the scatter plots are widely spread with no strong correlation between wind speed, direction and wave heights. This again suggests that the field campaign did not capture significant enough wind forcing to generate waves.

5

Wave Induced Near Bed Velocities and Bed Shear Stresses

Chapter 5 presents the results of sub-question 2: *How do the different spectral components present in the wave field contribute to the near bed orbital velocities and bed shear stresses, and how do these suspend sediments?*. Following the aforementioned method, wave driven near bed velocities are investigated to understand how waves stir the bed. The influence of short and long wave velocities are considered, matching the conducted approach for elevation variance. Then to quantify the forcing by waves on the tidal flat, the wave induced bed shear stress is presented during the south-west wind event. Finally the SSC response is compared to the computed wave induced bed shear stresses.

5.1. Horizontal Wave Driven Root Mean Squared Velocity

The horizontal root mean squared bed velocity is shown in figure 5.1. The cross-shore (u) and along-shore (v) velocities were parabolically detrended and had their mean removed. The 2D wave u_{rms} was then determined by considering the same frequency range as for the surface elevation spectra.

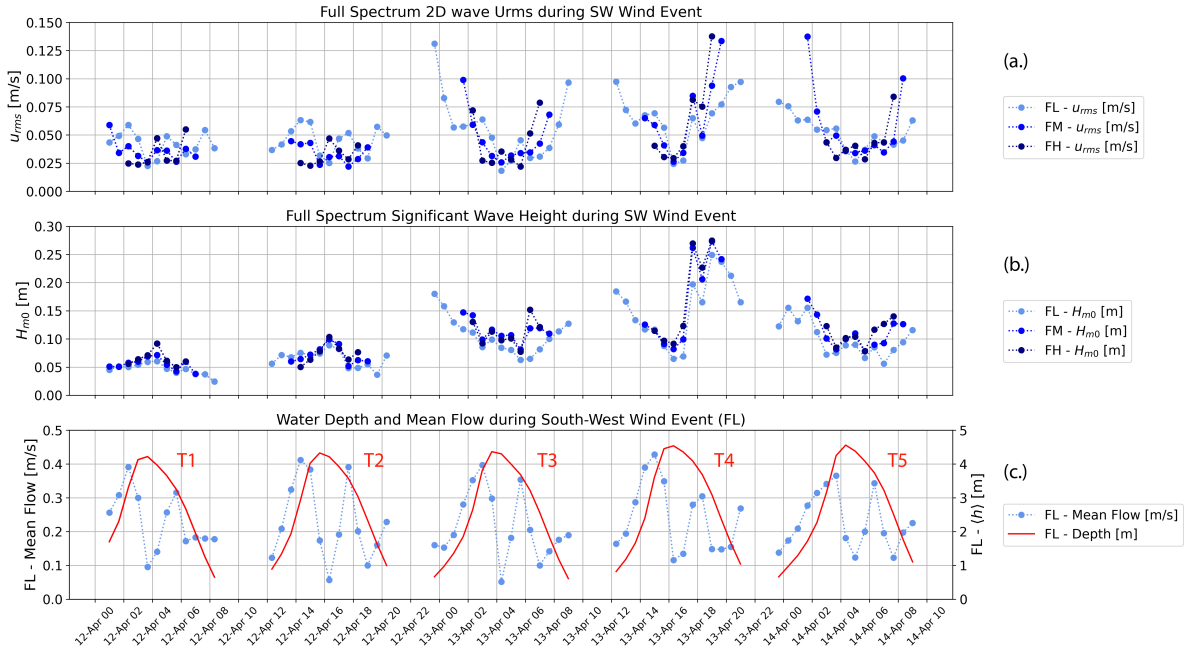

Figure 5.1: Panel (a.): Horizontal wave driven root mean squared velocity u_{rms} $[m/s]$. Panel (b.): Significant wave height H_{m0} $[m]$. Panel (c.): Mean horizontal flow u_{mean} $[m/s]$ and mean elevation $[m]$ at frame FL.

Panel (a.) shows the development of the 2D wave u_{rms}, considering the $f = [0.003 - 1.5]Hz$ frequency range. As expected tides T1 and T2 are relatively calm with no clear trend during the tidal signal. Meanwhile tides T3, T4 and T5 exhibit larger velocities that are clearly largest at the beginning of flood and end of ebb. The larger velocities during smaller water depths illustrate that wave orbital velocities were able to reach the bed more effectively.
Although water depth appears to exert a larger influence on the measured wave orbital velocities, the effect of wave height can be observed during ebb in tide T4. Here the peak in significant wave height H_{m0} is translated into a peak in u_{rms} that is otherwise not seen during the less energetic tides.

5.2. 2D Wave Velocity Variance: Short and Long Wave Assessment

Following the approach of sub-question 1, long and short wave contributions to total variance were determined. Now for 2D wave velocities instead of surface elevation. Using the same frequency bands as for the elevation variance density spectra, the velocity time series were divided using low and high pass filters. Long wave velocities were considered for $f = [0.003 - 0.1]\ Hz$, whereas short wave velocities were defined as $f = [0.1 - 1.5]\ Hz$. The results are illustrated in figure 5.2. Panel (a.) plots the magnitude of the full 2D wave u_{rms} signal $[m/s]$. Panels (b.) and (c.) show the magnitude of the short and long 2D wave u_{rms} respectively. Finally panel (d.) gives an overview of the mean flow u_{mean} $[m/s]$ and water depth $\langle h \rangle$ $[m]$ at the lowest measurement frame (FL).

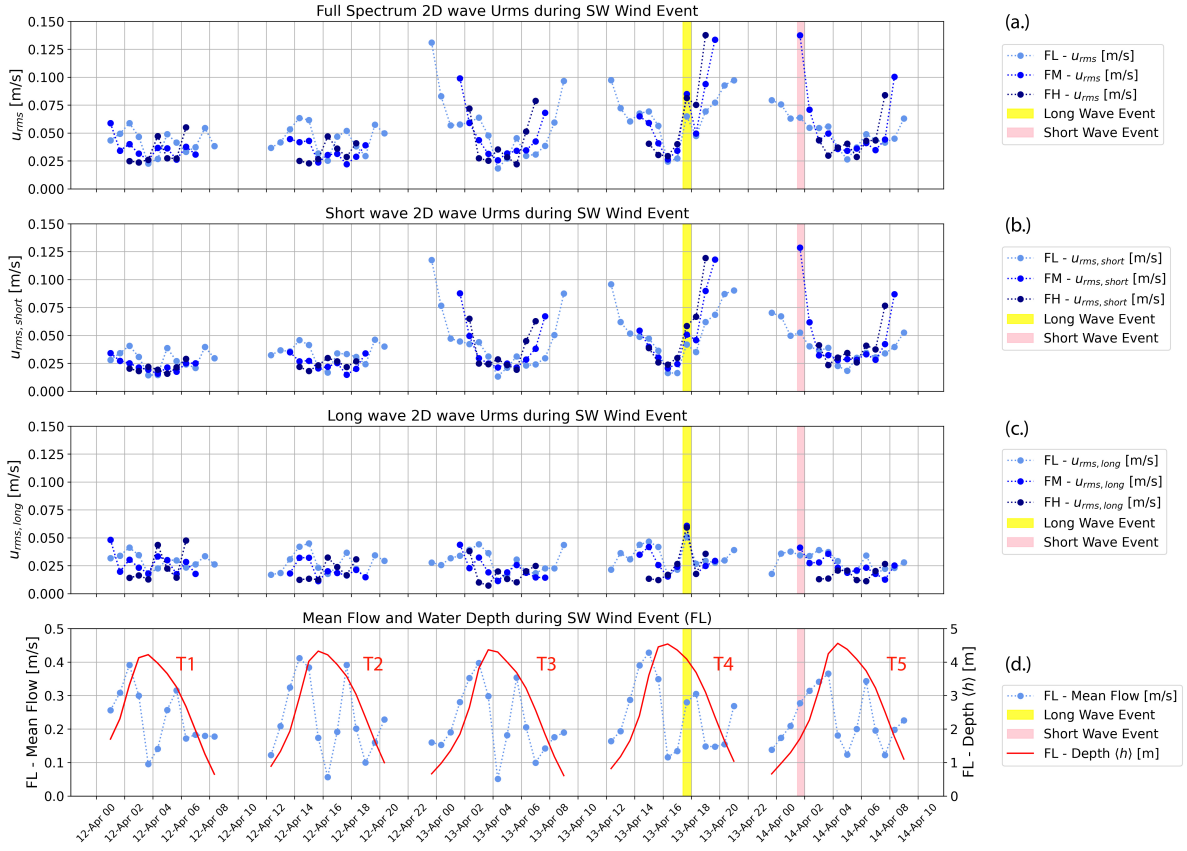

Figure 5.2: Magnitudes of full, short and long 2D wave u_{rms}. Panel (a.): Full spectrum 2D wave u_{rms} $[m/s]$. Panel (b.): Short wave 2D $u_{rms,short}$ $[m/s]$. Panel (c.): Long wave 2D $u_{rms,long}$ $[m/s]$. Panel (d.) Mean horizontal flow u_{mean} $[m/s]$ and mean elevation $[m]$ at frame FL.

During tides with negligible waves (T1 and T2), low magnitude turbulent motions remain in the velocity field which respond slightly to the variations in mean flow. Trivial waves lead to near negligible near bed velocities, therefore the analysis is concentrated on energetic tides T3, T4 and T5. The observed

2D wave velocities are mostly comprised of short waves, as shown by the similar signals in panels (a.) and (b.). These exhibited magnitudes ranging between $u_{rms,short} = 2.5 - 12.5$ [cm/s].
Long wave 2D velocities are consistently smaller in magnitude, ranging between $u_{rms,long} = 1 - 5$ [cm/s]. Interestingly, the previously identified long wave event (yellow) coincides with a peak in long wave 2D u_{rms}. During the highlighted long wave event at ebb of tide T4, the long wave component exhibited a large spike reaching $u_{rms,long} = 6$ [cm/s].

To better visualise the relative contribution of short and long waves to the 2D wave velocity field, the variance ratios are plotted in figure 4.8. Panels (a.) and (b.) plot the ratios of explained 2D wave velocity variance by short and long waves respectively.
During the three energetic tides (T3, T4, T5), short waves make up most of the velocity field. Despite this, long waves are seen to explain a significant portion of the total 2D velocity variance during high tide. At high tide they explained up to 60% of the velocity variance, compared to 10% of the elevation variance. This strongly suggests that long wave orbital velocities are more able to reach the bed, as expected considering the $k_{m02}h$ values for each frequency band.
This result is however not driven by a stark increase in long waves during high tide, instead it is due to the lack of short waves reaching the bed. Long wave variance is highest when total variance is lowest. An exception to this pattern is again the long wave event during ebb of tide T4. Here a peak is observed in variance explained by long waves across all three measurement frames.

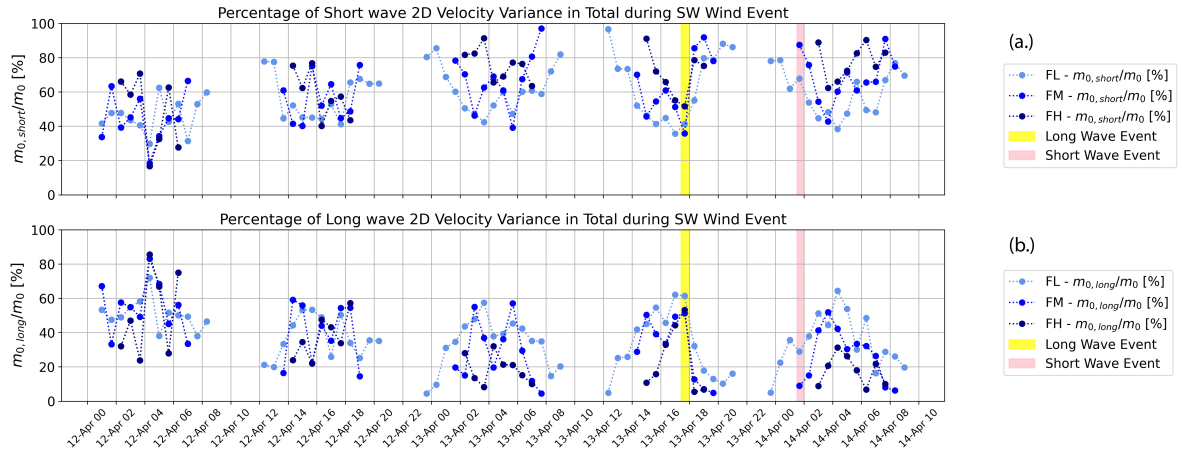

Figure 5.3: Short and Long wave contributions to 2D velocity variance during south west wind event. Panel (a.): Percentage of short wave 2D velocity variance in burst total [%]. Panel (b.): Percentage of long wave 2D velocity variance in burst total [%].

Cross-Shore Velocities during the Long Wave Event

As for surface elevation, figure 5.4 displays the cross-shore velocity time series at each measurement frame during the long wave event. The effect of the alongshore velocity (v [m/s]) was examined, however this contained a smaller long wave component. Thus it could be confirmed that the long waves during the burst were travelling (mostly) in cross-shore direction.
Examining the time series, a similar period of $T \approx 300s$ is initially seen as for elevation in figure 4.9. This clearly has the largest magnitude ($a \approx 0.2m/s$), and likely contributed most to the increased long wave variance. As for elevation, this wave is not repeated further along the time series where shorter periods can be observed.
Interestingly, the long wave oscillations barely grow between the cross-shore measurement frames. This was clearly visible for the elevation time series. The large early oscillation even appears to dissipate between the low and high frames, whilst shorter long waves maintain their magnitude more steadily.

Cross-Shore Velocities during the Short Wave Event

To compare contrasting regimes, a short wave event was also investigated. The highlighted burst in pink shows a large peak in short wave velocity variance at the middle frame during flood of tide T5. Due

to the low water depth, no burst was measured at the high measurement frame. The associated time series are shown in figure 5.5. Here it can be seen that the short wave oscillations clearly dominate their long wave counterparts. The magnitude of short wave oscillations far exceeds those in the long wave event, nearly doubling to $a \approx 0.4m/s$. Between the low and middle frames a large difference in magnitude can be observed. While the middle frame experience significant short wave velocities, these are barely present at the lower measurement frame. This could be attributed to differences in water depth, as short waves will struggle to reach the bed at the larger depth present at frame FL.

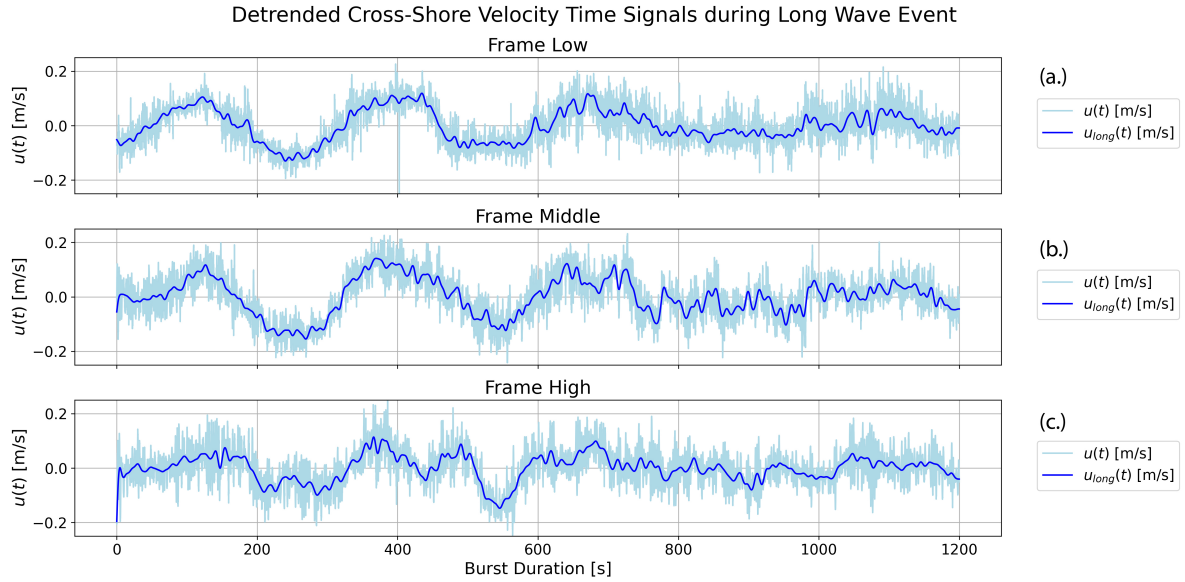

Figure 5.4: Cross-shore velocity $u(t)$ $[m/s]$ burst time series per measurement frame during the identified long wave event at ebb of tide T4 (13/04/2025 17:40:00). Panel (a.): Frame Low. Panel (b.): Frame Middle. Panel (c.): Frame High. Signals have had their mean removed and have been parabolically detrended.

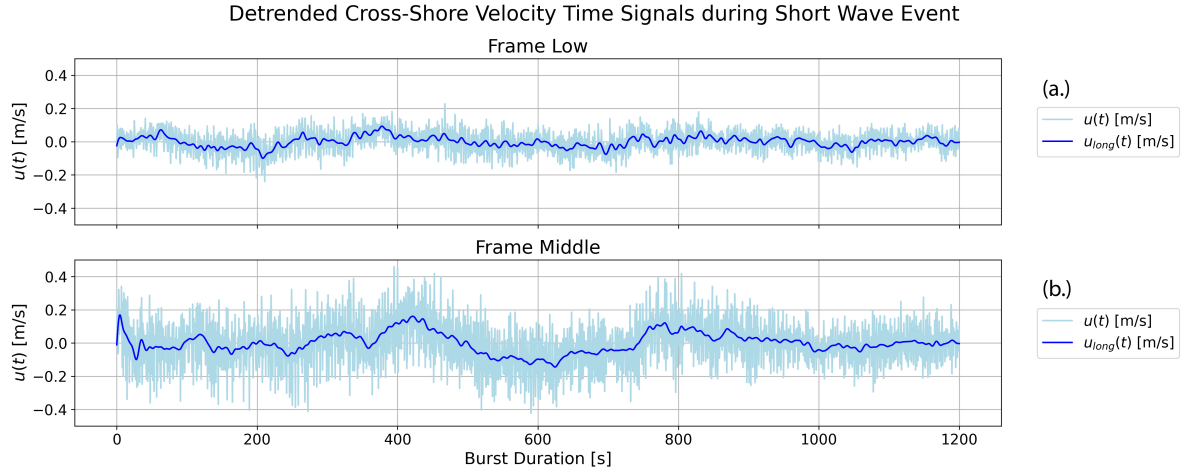

Figure 5.5: Cross-shore velocity $u(t)$ $[m/s]$ burst time series per measurement frame during the identified short wave event at flood of tide T5 (14/04/2025 01:40:00). Panel (a.): Frame Low. Panel (b.): Frame Middle. Signals have had their mean removed and have been parabolically detrended.

5.3. Peak orbital velocity

The peak orbital velocity was determined per burst using linear wave theory, considering the full spectrum significant wave height and mean zero-crossing period as per Q. Zhu et al. (2016). Then, comparing the obtained peak orbital velocities to the full spectrum 2D wave u_{rms}, figure 5.6 is obtained. In

panel (a.) the 2D wave u_{rms} (blues) and peak orbital velocities (reds) appear to follow each other relatively well across the five selected tides. For tides T1 and T2 with negligible waves, both show small velocities with little variation per depth. Then during energetic tides T3, T4 and T5, both velocities exhibit convex profiles with highest velocities during small water depths.

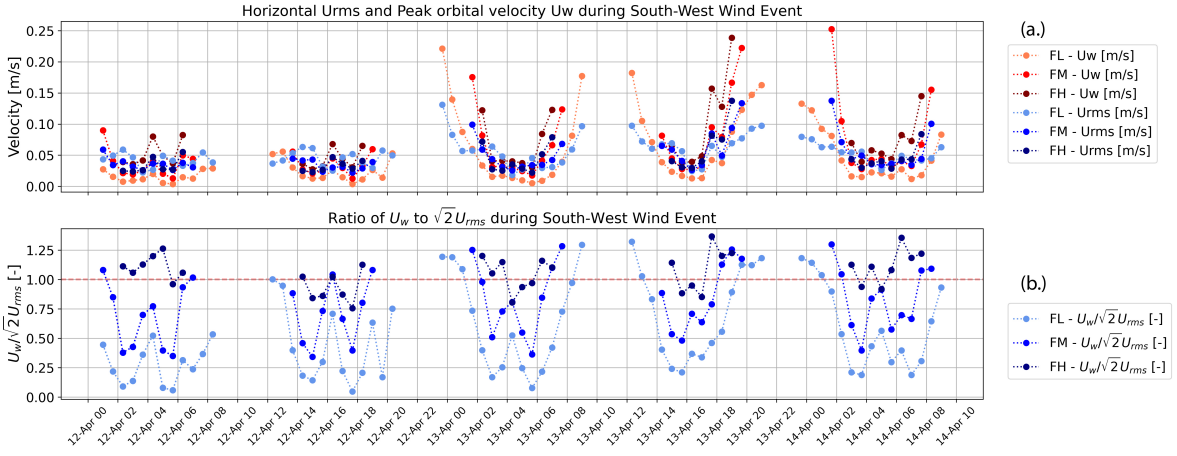

Figure 5.6: Panel (a.): 2D wave driven root mean squared velocity u_{rms} (blues) and peak orbital velocity u_w (reds) during the south west wind event. Panel (b.): Ratio of U_w to $\sqrt{2}U_{rms}$.

As for surface elevations, the peak orbital velocity can be approximated by $U_w = \sqrt{2} * u_{rms}$ (Wiberg & Sherwood, 2008). To test the equivalence between $\sqrt{2} * u_{rms}$ and peak orbital velocity U_w, their ratio was plotted in panel (b.).
Observing the obtained ratios, peak orbital velocities determined with wave spectral parameters (U_w) are often smaller than the equivalent determined with 2D wave u_{rms}. The root-mean-squared velocities appear to scale with the mean flow, with the lowest ratios occurring midway through flood and ebb tides. This suggests that the ADV velocity measurements captured greater flow velocities than those determined via pressure measurements. Furthermore, this effect appears largest at the most offshore frames with largest water depths. At Frame FL the ratio exhibits a wide range of values, whilst at Frame FH it remains more constant.
The largest discrepancies occur whilst velocities are small and waves are barely present. However at the beginning of flood and end of ebb when wave velocities are large, the ratio between U_w and $\sqrt{2} * u_{rms}$ is close to 1. This is a positive outcome, since it suggests that the most impactful waves are described similarly by both sensors.

Limits to a spectral approach for U_w and τ_w

Peak orbital velocities U_w were determined using a characteristic wave, which is then used to determine the average bed shear stress τ_w by said characteristic wave. Preferably, the method would consider the wave driven bed shear stress for short and long wave frequency bands individually. This was however not done, since the interaction between the short and long wave field leads to complex patterns of wave driven bed shear stress. Similar to the non-linear interactions between tidal and wave driven bed shear stress, the components cannot be added linearly (Soulsby, 1997).
Instead it was chosen to adopt a simplified approach, and consider a characteristic wave representing the full wave field. By acknowledging the variations in long and short wave variance for surface elevation and 2D near bed velocities, the full spectrum wave driven bed shear stress can be interpreted with greater context. To properly ground the findings from this simplified approach, it would be advised to further investigate the role of long and short wave bed shear stresses in detail following a non-linear approach.

5.4. Wave Reynolds number and Wave Friction Factor

Using the formulation by Soulsby (1997), the wave friction factor f_w [-] was determined considering the hydraulic bed regime. The small characteristic waves (low H_{m0}, short T_{m02}) with large water depths lead to wave Reynolds numbers that never exceed the 10^5 laminar flow boundary. Figure 5.7 illustrates this result, showing that the bed regime is classified as laminar during the entire south-west wind event. In reality the flow will naturally not be laminar at the bed of the tidal flat, however this does indicate that inertial forces never significantly culminated above viscous forces. Thus a relatively smooth flow was present in the wave boundary layer.

Under the ”laminar” regime, the wave friction factor is not dependent on relative roughness (r), and is instead fully related to the wave Reynolds number: $f_w = 2\sqrt{Re_w}$. These conditions are rare for exposed coastlines, however they have been identified previously on tidal flats with very small waves (Green, 2011).
Under the laminar regime, a larger dependency on wave period is introduced to the wave shear stress formulation ($\tau_w \propto T^{2/5}$). This enlarges the negative relation between wave period and bed shear, causing longer waves to induce even smaller bed shear stresses. This can be explained by considering the development time of the wave boundary layer. Where longer wave periods facilitate the growth of a thicker boundary layer. This reduces magnitude of the velocity gradients within the layer, driving smaller bed shear stresses (Bosboom & Stive, 2023).

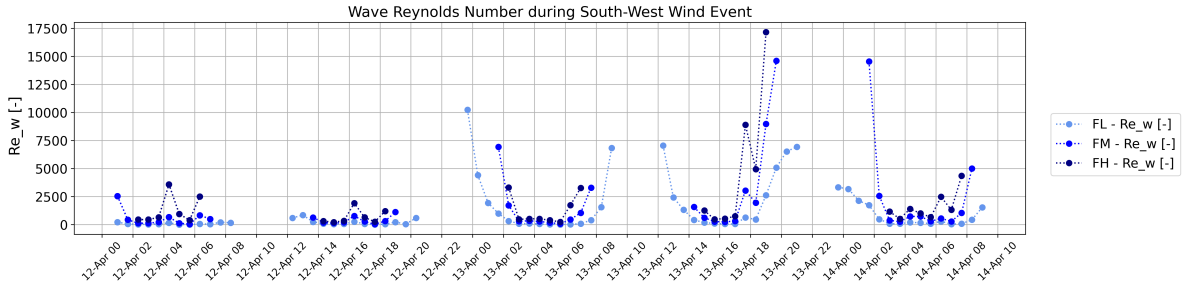

Figure 5.7: Wave Reynolds number computed per burst for 5 tides during the south-west wind event. With all values underneath the 10^5 boundary, a laminar regime can be considered present at the bed.

5.5. Wave driven bed shear stress

With the hydraulic regime and wave friction factor determined, it was possible to compute the burst average wave bed shear stress. This was done considering the full wave spectrum during the south west wind event. Figure 5.8 shows the burst average SSC $\langle SSC \rangle$ $[g/L]$ in panel (a.) and the development of wave driven bed shear τ_w $[Pa]$ in panel (b.). Full spectrum peak orbital velocity U_w $[m/s]$ and significant wave heights H_{m0} $[m]$ are given in panels (c.) and (d.) respectively. Finally panel (e.) provides an overview of the water depths $[m]$ at each measurement frame.

Due to the quadratic dependency on peak orbital velocity, the wave bed shear stress follows this closely. Small deviations in the signals can be observed due to the differences in wave friction factor and wave Reynolds number.
The wave driven bed shear stress is highest for energetic tides T3, T4 and T5. During these tides the bed shear stress increases for shallower water depths, reaching $\tau_w \approx 0.25Pa$. Meanwhile high tides exhibited consistently small shear stresses during the largest water depths. These never exceeded $\tau_w \approx 0.05Pa$, coinciding with the shear stresses of tides T1 and T2 which had negligible waves. This demonstrates how large water depths inhibit waves from generating bed shear stresses.

This relationship between wave heights, water depth and wave bed shear stress is strongly confirmed when comparing tides T4 and T5. During the ebb of tide T4 a large increase in wave height is detected. However this only results in a small spike in wave bed shear stress. During flood of tide T5, there are much smaller waves, yet the water depth is significantly smaller. This leads to a much greater increase in wave bed shear stress.
The observed response confirms that waves were significantly more effective at forcing the bed during

smaller water depths. As a result, higher locations on the tidal flat generally experienced larger wave bed shear stresses.

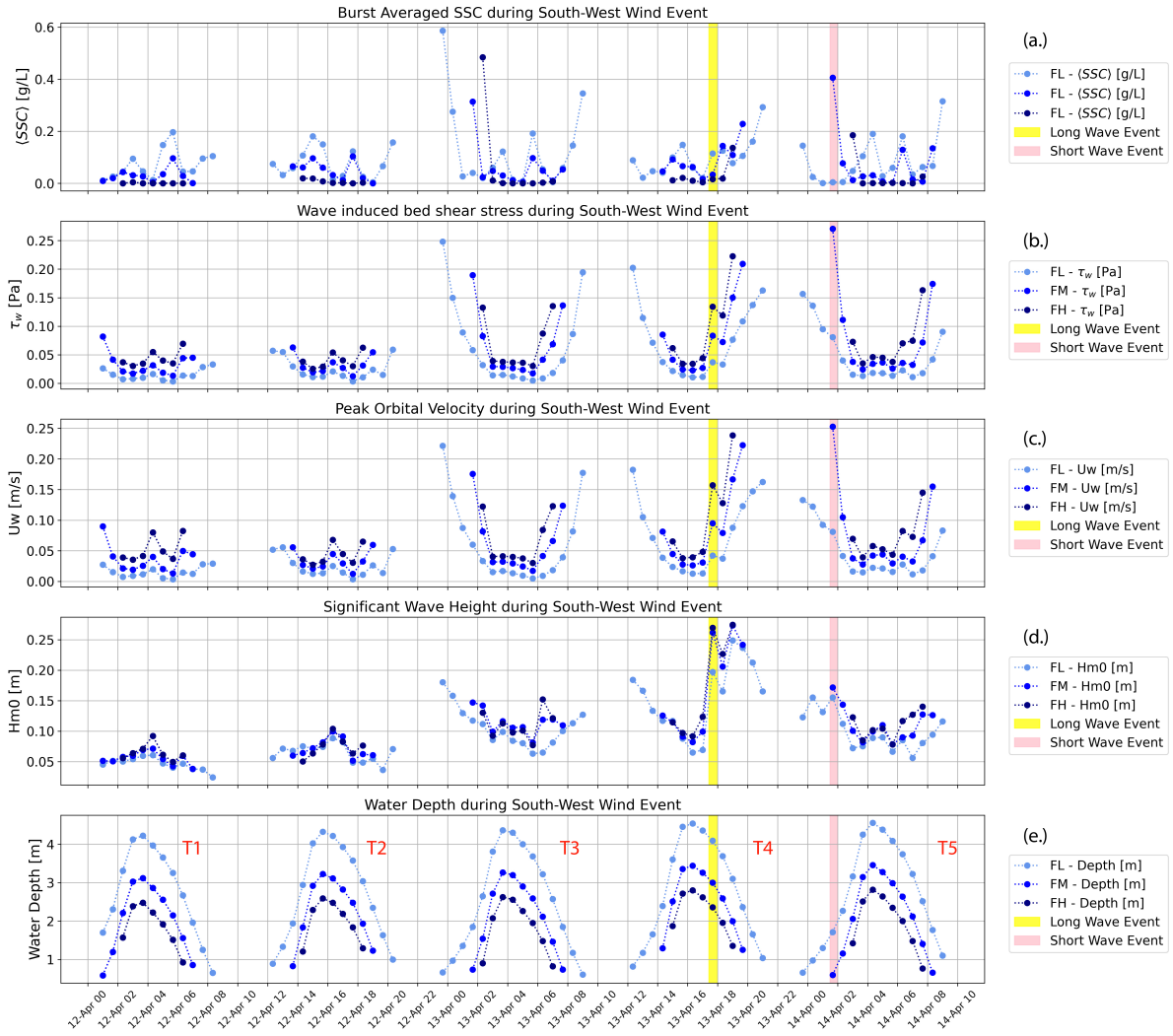

Figure 5.8: Wave induced bed shear stresses, peak orbital velocities and wave heights during the south west wind event. Panel (a.): Burst averaged SSC signal $\langle SSC \rangle$ $[g/L]$. Panel (b.): Wave induced bed shear stress τ_w $[Pa]$. Panel (c.): Peak wave orbital velocity U_w $[m/s]$. Panel (d.): Significant Wave height H_{m0} $[m]$. Panel (e.): Water depth $\langle h \rangle$ $[m]$

5.6. Observed relation between SSC and wave driven bed shear stress

To determine the degree to which waves actually suspended sediments across the tidal flat, a comparison was made between the determined wave bed shear stress and the mean SSC values per burst at each measurement frame. This is presented in figure 5.9, considering all data points per frame during the south-west wind event. The long wave and short wave events are highlighted in yellow and pink respectively. Their SSC time series are presented in section 5.7.

Viewing the results, there is generally no strong correlation between wave bed shear stress and the measured SSC signals. At the lowest frame (FL), observed SSC was seen to take a wide range of values for similar low shear stresses. Inversely, the high measurement frame consistently measured near zero sediment concentrations at a range of wave bed shear stresses. The middle frame is characterized by a stronger correlation, however SSC still varies at low shear stresses.

As shown in figure 5.8, the high frame (FH) experienced larger wave driven bed shear stresses at each

stage of the five tides. However these larger wave driven shear stresses did not lead to the suspension of sediments at the bed.
Meanwhile the lower measurement frame experienced consistently smaller bed shear stresses by waves, yet it generally had a larger SSC signal than the middle and high frame. Furthermore, the large spread of SSC measurements at FL does not appear to be driven by changes in wave induced shear stresses. This again indicates that the wave induced bed shear stress did not drive significant suspension of sediments. Instead the variation of SSC at the low frame could be due to the presence of a turbid fringe. This phenomenon is often identified at the lower edge of tidal flats, and travels up and down the lower portion of the flat in shallow waters due to tidal and wave forcing (Green & Coco, 2014).

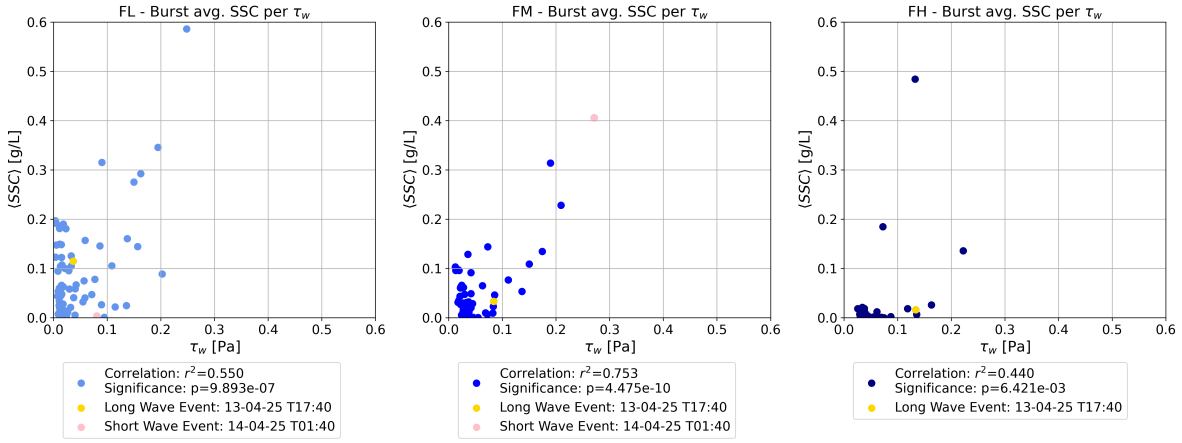

Figure 5.9: Burst averaged SSC signal in $[g/L]$ plotted against computed wave bed shear stresses $[Pa]$ for each measurement frame (FL, FM, FH) during the south-west wind event. The long and short wave events are plotted in yellow and pink respectively.

5.7. SSC response during Long and Short Wave Events

Returning to the spectral approach figures 5.10 and 5.11 examine the effect of short and long wave velocities on suspended sediment concentration. By plotting the long and short wave velocities with the full SSC signal, an attempt is made to assess whether SSC responded at the long/short wave timescale.

SSC Response during Long Wave Event

As shown in the burst averaged assessment, wave driven bed shear stresses were small during the long wave event: $\tau_w = 0.04Pa$. These exhibited a relatively small mean suspended sediment concentration $\langle SSC \rangle = 0.11g/L$. Overall the influence of the long wave event therefore appears small.
Figure 5.10 plots the complete SSC time series and long wave cross-shore velocity (u_{long}) during the long wave event at each measurement frame. Overall the SSC signal is largest at the low measurement frame, with concentrations starting at $0.1g/L$ and increasing to $0.2g/L$. As reflected in $\langle SSC \rangle$, the high frame often detects zero SSC.
Long wave velocities are largest at the low frame, decreasing slightly in onshore direction. The largest velocity oscillation ($T \approx 300s$) at the start of the time series appears to drive no response in SSC. Shorter waves do however appear to generate a matching fluctuation in SSC at a time scale of $T \approx 20s$. This is especially pronounced at the low frame.

SSC Response during Short Wave Event

The short wave event took place at the middle frame, where large wave driven bed shear stresses ($\tau_w = 0.28Pa$) led to relatively large mean SSC ($\langle SSC \rangle = 0.41g/L$). Meanwhile the same burst exhibited minimal sediment concentrations ($\langle SSC \rangle = 0.01g/L$) and shear stresses ($\tau_w = 0.08Pa$) at the low frame.

Zooming in on this short wave event, figure 5.11 plots the short wave cross-shore velocities u_{short} and complete SSC time series. The short wave event occurred for very small water depths during flood of tide T5. Considering the stark difference in SSC signal, it appears that a turbid fringe likely just entered the middle frame location. At this small water depth ($\langle h \rangle = 0.6m$), small waves effectively suspend sediments, and keep already suspended sediments in suspension. Meanwhile at the low frame, the large water depth inhibits the small wave orbital velocities from reaching the bed. This is confirmed by the smaller magnitude of the short wave velocities. Considering the signal of mean SSC in figure 5.8, it is likely that the turbid fringe passed the low frame at an earlier burst. However now the sediments have been advected further onshore or have already settled.
When comparing the short wave oscillations to those in the SSC time series, it is hard to visually identify whether the two respond at the same frequency. For this, a co-spectral analysis would be effective. This would also confirm the relation between the long wave cross shore velocities and SSC in figure 5.10.

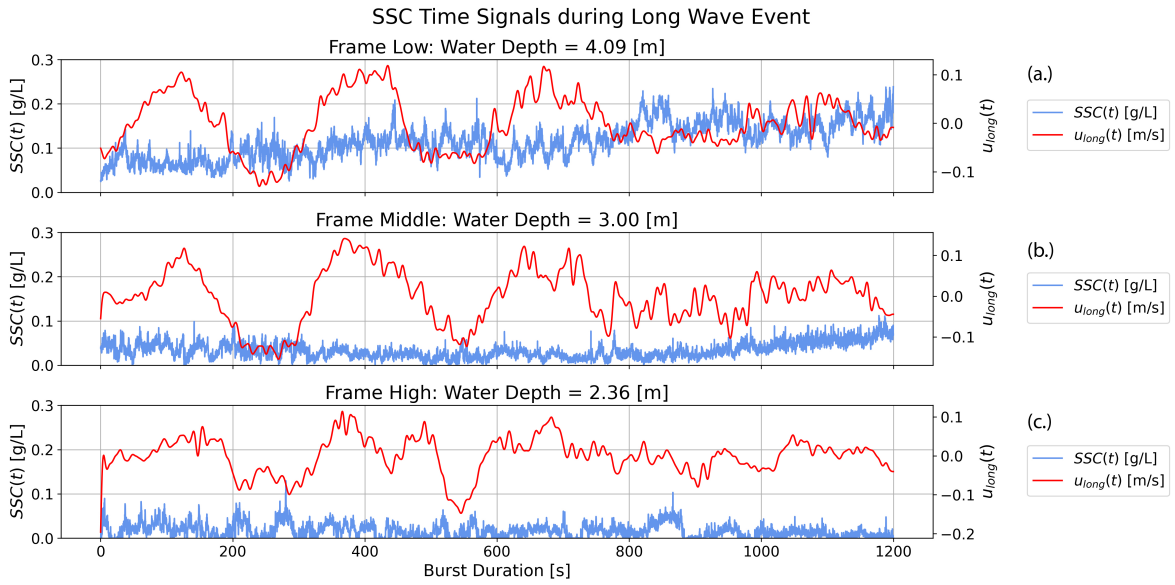

Figure 5.10: Complete SSC $[g/L]$ time series and long wave cross-shore velocities u_{long} during the identified long wave event. Panels a, b, c show both time series at the low, middle and high measurement frames respectively.

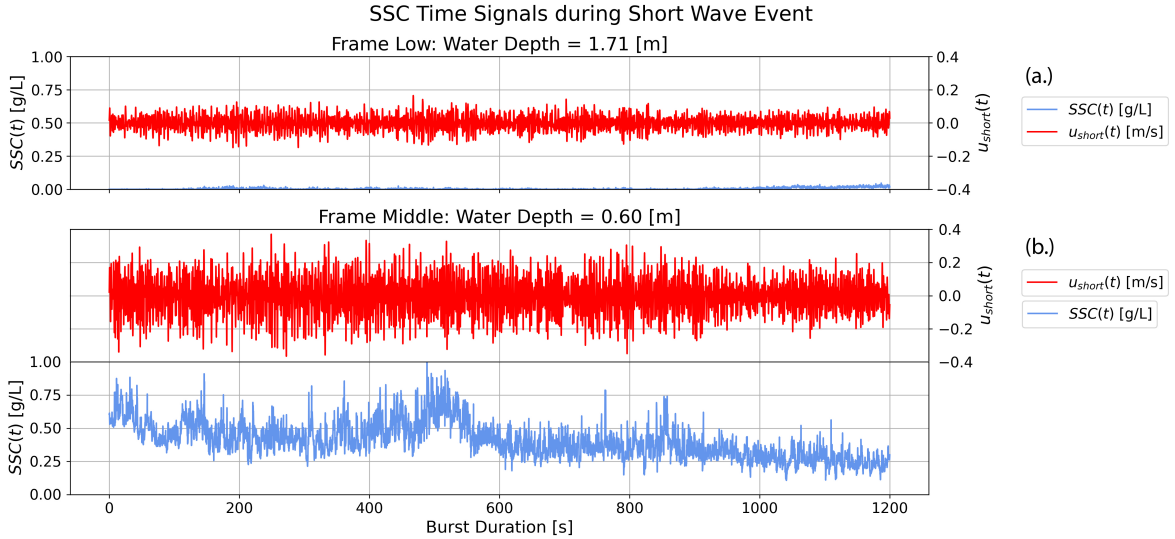

Figure 5.11: Complete SSC $[g/L]$ time series and long wave cross-shore velocities u_{long} $[m/s]$ during the identified short wave event. Panels a, b show both time series at the low and middle measurement frames respectively.

6

Discussion

Chapter six discusses the obtained results from sub questions 1 and 2 in detail. The chapter starts by reviewing the observed wave transformations under tidal influence, as well as the identified SSC response in light of near bed velocities and bed shear stresses. These are framed against previous studies to obtain a critical interpretation of the observed relations. Secondly the applied method is reviewed, considering the strengths and weaknesses of a spectral approach as well as the field campaign. Finally the findings are presented in a broader context. The role of observed wave dynamics on present morphology at the GvB tidal flat is investigated. Then potential measurement locations and future research are identified to further the understanding of wave driven morphodynamics on tidal flats in the Western Scheldt estuary. Figure 6.1 presents a schematic overview of chapter six, where the aforementioned topics have been classified into three categories: 1. Zooming In, 2. Approach Assessment and 3. Zooming Out.

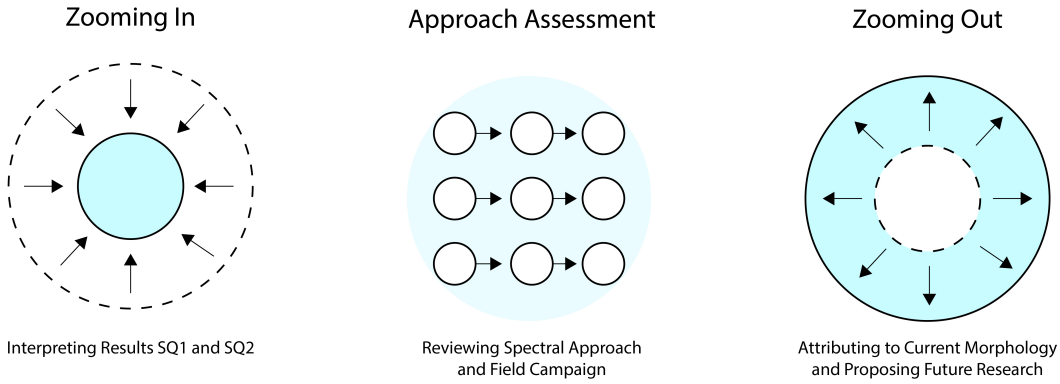

Figure 6.1: Schematic overview of chapter 6. The presented discussion can be classified into three general themes.

6.1. Zooming In - Understanding Wave Transformations and Wave Driven SSC

Using the results presented in chapters 4 and 5, answers are sought for the constructed sub questions. Considering the explorative nature of this report, many results have been interpreted as presented in chapters 4 and 5. However the following section dives deeper into the following topics: 1. The observed depth control on short wave mean period; 2. Understanding short and long wave transformations; 3. Wave driven sediment suspension and diagnosing a turbid fringe.

6.1.1. Investigating the depth control on mean period

For both flood and ebb tides, short wave mean zero down-crossing period $T_{m02,short}$ was seen to increase with depth. As shown in figure 4.10, wave periods were largest during high tide and decreased with falling water levels. Meanwhile wave period is expected to remain constant over depth for constant forcing according to linear wave theory.

Impact of Increased Fetch at Larger Water Depths
As fetch increases with depth, the wind has a larger distance to force the surface. This in theory generates larger wave periods and wave heights Holthuijsen (2007). The increase in $T_{m02,short}$ with depth follows this theory. However wave heights $H_{m0,short}$ contradicted it as they did not respond to larger water depths (and thus fetch). Therefore the effect of fetch on the wave field is to be questioned. To properly investigate the effect of fetch variations on mean period and wave heights, empirical formula could be utilized to determine the theoretical development of each parameter. If wave periods are more sensitive to fetch than wave heights, this may be explain the observed transformations of the short wave field with depth.

Impact of Attenuation Factor $S_w(f)$
The increase of short wave mean period with depth could also suggest that smaller waves are unable to reach the bed when water levels rise. This phenomenon was previously identified by Green (2011), who also found wave periods ($T_{m01} = 1 - 1.8s$) increasing with water depth ($\bar{h} = 0.25 - 1.25m$). Green, who used near bed velocity measurements to determine spectral parameters, attributed the increase in T_{m01} to the attenuation of small wave orbital velocities at greater depths. He identified that attenuation of orbital velocities according to linear wave theory explained all of the observed changes in T_{m01} for multiple tides. However there were also periods during which the change in T_{m01} could not be explained by attenuation alone. These scenarios were justified by changes in the surface elevation spectra, however these were not described in detail.

This study utilised pressure measurements and constructed elevation variance density spectra using an attenuation factor $S_w(f)$. The factor considered the attenuation of wave induced pressure with depth, following linear wave theory just like Green (2011). Therefore the obtained spectra should be corrected for depth driven attenuation, and not exhibit the same changes in mean period with depth.
However, the structure of the attenuation factor is critical to ensure proper restoration of local wave variance. If high frequencies are not tapered properly, T_{m02} will be too small due to noise. Meanwhile excessive filtering of high frequencies can result in T_{m02} that are too large.
Attenuation is naturally larger for greater depths, therefore the amplification of the attenuation factor increases to compensate. If the factor is not constructed properly, depth dependent modulation of the mean period will occur as m_2 is skewed due to incorrect processing of higher frequencies.
The modulation of mean period with depth has a knock-on effect for the wave driven bed shear stress. Following the laminar bed formulation, wave induced bed shear stress is more strongly dependent on wave period. This would lead to an underestimation of τ_w at larger water depths, since it is negatively related to mean period.

In light of this, it would be critical to confirm the effect of attenuation factor $S_w(f)$ on mean period. In a study by Van Der Lugt et al. (2024), the frequency range of $S_w(f)$ influenced the obtained spectral wave heights and periods. In their analysis, considering 0.3Hz more led to a decrease of H_{m0} by 1% and increased T_{m02} by 1.2%.
Conducting a similar sensitivity analysis would help interpret the effect of $S_w(f)$ on mean spectral period over depth. With this knowledge it would be possible to select an optimal attenuation factor which doesn't skew high frequencies whilst obtaining physically correct wave parameters.

6.1.2. Long and short waves on the GvB tidal flat

This research strived to use a spectral approach for better understanding of wave dynamics in relation to tidal flat morphodynamics. By examining distinct long and short wave frequency bands, greater detail could be obtained compared to a monochromatic approach. Significant peaks in long wave variance were consistently identified in the obtained surface elevation spectra. These gave rise to the long wave frequency band which was defined between $f = [0.003 - 0.1]Hz$.

Long Wave Elevation Variance
The long and short waves were characterised in figures 4.5 and 4.6. Unfortunately this analysis confirmed that the measurement period $T_{burst} = 20min$ was insufficient to capture the longest waves, with spectral leakage occurring in the first frequency bin.
With the long wave spectral parameters damaged due to leakage, the assessment was continued considering total burst variance. As shown in figure 4.8, the elevation variance spectra were dominated by local short waves. These typically made up at least 80% of the total variance in each burst. During energetic tides, long wave variance exhibited small peaks during high tide reaching 10% of the total variance. The peak was most pronounced during ebb of tide T4, coinciding with the most energetic burst. Here long waves explained more than 20% of the total variance at frame FH. During these high tides, a small increase in long wave variance could be observed as waves travelled towards the shore.

S. Zhu et al. (2024) also identified a steady increase in long wave variance as waves propagated towards the shore. Their campaign on the muddy Dafeng tidal flat in the Yellow Sea identified long waves defined as $f < 0.05Hz$. Their variance steadily increased towards the shore under all tidal phases. This was attributed to the gradual release of long waves across the tidal flat. Compared to the suddenly breaking short waves, long waves maintained their form and shoaled during propagation until they released from the wave group. The peak in long wave variance during high tide was not identified by S. Zhu et al. (2024). Instead the largest increase was seen during ebb tides, where long waves explained nearly 10% of the variance.
With only three energetic tides (T3, T4, T5), no strong comparison can be made between the observed long waves and those identified by S. Zhu et al. (2024). Furthermore, large differences in bed morphology will deeply affect the transformation of long and short waves. The GvB site is relatively bare with little bed forms. Meanwhile the Dafeng flat was characterised by fluid mud and a salt marsh at the most cross shore frame.

Long Wave Velocity Variance
To investigate how long and short waves stirred the bed, velocity variance was considered in the same manner as surface elevation. Immediately it could be seen that long waves explained significantly larger fractions of the velocity variance compared to the surface elevation. For example, the energetic ebb of tide T4 had long waves explain 20% of the elevation variance. Meanwhile long waves contributed to 60% of the velocity variance during the same burst.
The results suggest that long wave orbital velocities reached the bed more effectively, which is to be expected considering long waves were classified in shallow water (figure 4.6). Short waves were classed in intermediate water, which is reflected by their smaller portion of velocity variance.
Long wave velocity variance peaked during high tide and decreased with falling water levels. Furthermore, the long wave contribution was consistently larger at the lower flat compared to the higher measurement frames. These patterns could be interpreted by considering the attenuation of short wave orbital velocities at larger water depths. The remaining long wave velocities will therefore explain a larger portion of what remains.
Despite long waves explaining 60% of velocity variance during high tide, the magnitude of 2D wave u_{rms} is smallest during these periods. The largest near bed velocities were measured at low water depths when the dominant short waves reached the bed. These in turn generated the largest wave bed shear stresses across the tidal flat. Long waves are therefore not suspected to drive the most sediment suspension. However long waves hold a greater potential to suspend sediment during large water depths compared to short waves.

Interpreting tide T4
The energetic event during the ebb of tide T4 exemplifies this potential, where both wave heights and bed shear stresses peaked during large water depths ($H_{m0} = 0.27m$ and $\tau_w = 0.13Pa$ at frame FH). As reflected by the peaks in elevation and velocity variance, the wave event can be attributed to a spike in long waves.
This event consistently stood out compared to the other energetic tides (T3 and T5), as it occurred during relatively large water depths. Lacking any repetition across tides, the long waves were likely generated outside the local wave field. Wind was also not the driver, since the previous analysis indicated wind speeds were mild ($u_{wind} = 5m/s$). Despite the lack of proof, vessel waves could explain the event considering the GvB tidal flat borders a busy shipping route. If correct, this could highlight the impact of large container vessels on tidal flat morphology.

6.1.3. Exploring the SSC response and diagnosing a turbid fringe

Generally SSC is seen to respond to changes in bed shear stress, where larger velocities excite the bed and entrain particles in the water column (Green & Coco, 2014). Waves were seen to drive the largest peak orbital velocities (U_w) during the smallest water depths. This made wave driven bed shear stresses peak at the beginning of flood and end of ebb (figure 5.8).
This observation is in line with the model derived by Le Hir et al. (2000), who explains that wave induced bed shear stress is maximum at the seaward zone of wave saturation. The latter being defined as the cross shore location where an incoming wave (H_i) becomes depth limited $(H_i/h_s)_{lim}$. For depths smaller than the saturation limit (h_s), wave induced bed shear stress decreases linearly with depth.
Considering the observed waves were small enough to never be depth limited (figure 4.11), the obtained shear stress signals in figure 5.8 always lie within this maximum limit. This explains why the wave driven bed shear stress never started to decrease at the smallest water depths. Furthermore, bursts were not considered for water depths smaller than $h \approx 0.6m$ to protect data quality. If smaller water depths were assessed, this depth limited regime may have been present.
Wave orbital velocities and bed shear stresses were seen to increase between the low and high measurement frames. The largest wave driven bed shear stresses were consistently observed at the most shoreward measurement frame (FH). This is commonly explained by the larger fetch which is available at more shoreward positions, thus allowing waves to grow more under the same wind speeds (Green & Coco, 2014). The smaller water depths at frame FH would also allow orbital velocities to reach the bed more effectively, driving the increase in τ_w. Finally the shoaling of waves is another likely reason, however this would require the calculation of a shoaling coefficient to confirm its effect.
Green (2011) found that SSC was highest during low tide, attributing this to low fetch but small water depth conditions during which wave orbital velocities easily reached the bed. The same response was expected on the GvB tidalflat, since both U_w and τ_w were seen to peak during low water depths.
Observing 4.4 the burst averaged SSC signal somewhat adheres to this theory, where for energetic tides (T3, T4, T5) the SSC is seen to grow while water depths decrease.

Diagnosing a turbid fringe

Plotting burst averaged SSC per wave bed shear stress tells a different story. Figure 5.9 shows how SSC varies independently of shear stress at the low frame, whilst the bed at the high frame is clearly unresponsive to any changes in shear stress. This break in relation between shear stress (or peak wave orbital velocity) and SSC was attributed to the presence of a turbid fringe by Green et al. (1997). Turbid fringes are characterized by unusually large SSC values which are found by the shallow edge of water. Green et al. (1997) speculated that the turbid fringe was maintained by the oscillation of the tidal flow, whilst waves kept the sediment in suspension at shallow water depths. These mechanisms have also been identified in a range of papers reviewed by Green and Coco (2014).
The large spread of mean SSC for small bed shear stresses at FL strongly suggests the manifestation of a turbid fringe. From this perspective, the modulation of SSC with depth was not due to the increased wave shear stress, but the water depth itself. Frame FM exhibited a similar yet slightly smaller range of SSC values for small bed shear stresses. This suggests that the turbid fringe was advected up and down across the two measurement frames with the tidal flow.
The turbid fringe was not identified at the high measurement frame (FH), since mean SSC was consistently near zero. Despite the largest wave induced bed shear stresses, this location measured the smallest concentrations. In theory the patterns of wave orbital velocities and bed shear stresses would suggest frame FH to detect the highest SSC. However the analysis did not consider the magnitudes of these variables, therefore they may have been insufficient to induce a response.
To properly determine the influence of waves on sediment suspension and transport, it is critical to determine whether the observed bed shear stresses exceed the bed strength. The Partheniades equation is an example of this approach, as the erosion formulation considers a critical shear stress which is inherent to the bed properties (Green & Coco, 2014).
The erodibility of the bed is extremely relevant when considering tidal flat morphodynamics. Due to its high variability across tidal flats, the same forcing can have vastly different effects depending on the location. In a study by Q. Zhu et al. (2019), bed stability was found to decrease in offshore direction on the Kapellebank mudflat. If the same distribution was present on the GvB site, it would help explain the lack of SSC response under larger bed shear stresses at frame FH.

6.2. Approach Assessment - Evaluating the Spectral Analysis and Field Campaign

The following section reflects on the applied method, specifically reviewing the added understanding of a spectral approach. Then the field campaign and data processing is discussed in more detail, considering the strengths and weaknesses as well as limitations of the analysis.

6.2.1. Spectral analysis in review

This study strived to answer the following question: *"Can a spectral approach provide a better interpretation of wave driven sediment dynamics on muddy tidal flats?"* In doing so, a spectral approach was conducted to uncover how waves across various frequencies developed on the GvB tidal flat. In particular, the approach intended to highlight the distinct yet interacting long and short wave fields. In doing so it was possible to identify the prevalence of long waves on the tidal flat, and compare their transformations to those of the short waves.
The short wave field could be considered very linear, with small Ursell numbers suggesting that linear wave theory can provide a valid description of their transformations. Short waves were also found to dominate the elevation variance spectra, making up most of the incoming wave field.
Long waves on the other hand were significantly less prevalent, yet did define some bursts. The long wave characterisation was limited due to spectral leakage. This occurred due to the presence of long waves which exceeded the burst period of $T_{burst} = 20min$. Despite this limitation, elevation and velocity variance granted an understanding of long and short wave contributions to the total wave field.

The analysis of long wave elevation and velocity variance illustrates the high capacity of long wave orbital velocities to reach the bed. Sadly there were few bursts in which this effect could be observed since waves were small. Therefore under mild conditions, a monochromatic approach should generally be reliable to interpret wave driven morphodynamics.
Despite this, the bursts during ebb of tide T4 did gain greater detail through the spectral approach. The variance assessment revealed that these bursts exhibited large wave heights and near bed velocities due to incoming long waves, not short waves. This would likely not have been identified if a monochromatic approach was applied. Therefore a case can be made for investigating long and short wave bands on tidal flats.
To fully grasp the potential of the spectral approach it would be of interest to examine the SSC response during the long wave event. Furthermore, the approach could be extended to examine oscillations of SSC at long wave timescales. Similar to a co-spectral analysis, this can identify how long waves potentially drive sediment suspension across the tidal flat.
In the case of the GvB dataset, the observed waves were generally too small for it to be effective. However the approach is expected to hold greater value for more energetic field measurements, such as the 2016 measurements in Zuidgors by de Vet (2020).

6.2.2. Field campaign Evaluation

The conducted field campaign gathered pressure, velocity and SSC measurements using a range of sensors. The use of ADV probes in tandem with STMS sensors is commonly used to monitor waves, currents and sediment on tidal flats. Despite this, the approach is not immune to errors and also has limitations that hinder analysis. In the the spirit of Downing (2006), the following section describes the good, the bad and the ugly of the field measurement campaign.

The Good
The field campaign gathered a month of high frequency pressure, velocity and SSC measurements at three cross shore locations. The deployment of the frames can be considered successful due to the large number of bursts which passed the data quality requirements as described in chapter 3.
Furthermore, the frames were deployed at the intended elevations, ensuring near bed measurements were obtained. The ADV x-axes were closely aligned, ensuring directional spreading of waves would not effect the frames differently. Finally the sensors did not display any significant displacements or tilt as per the GPS measurements.

The obtained data generally appeared trustworthy when applying checks and comparing to other sources. This was observed when comparing the obtained elevation signals to measured tides at the Borsele

station of Rijkswaterstaat (figure 4.3). Furthermore, the elevation time series of each frame collapsed nicely into a single series of parabolas.
Another good aspect of the field campaign was the use of three measurement frames instead of two. Some studies opt for a low and high measurement frame. However the use of a middle frame proved valuable in this study, as it provided more spatial detail. This in turn effectively captured a turbid fringe which oscillated between the two frames. Using only a low and high frame would have limited the analysis.

The Bad
The strict quality control ensured that burst measurements were trustworthy, however this did limit the range of considered values. By only using bursts which contained zero NaN values, large quantities of data were not considered. This specifically impacts the measurements during small water depths, as sensors may briefly emerge during these conditions. Instead of rejecting these bursts entirely, it may be beneficial to consider those with small gaps. This would restore measurements taken at low tide, enabling a more complete assessment.

The second bad aspect of the field campaign is related to the STMS sensor calibration. As described in chapter 3, a wet calibration was performed using a single sediment sample from the middle of the GvB tidal flat.
Firstly it would have been more accurate to calibrate each sensor with a local sediment sample. Considering the heterogeneity of bed sediments on tidal flats, calibrating all locations with a single sample may have induced errors.
Secondly the wet calibration assumes that all sediment is kept in a homogenous suspension. The electric agitator did keep the suspension in consistent motion, however it may have not been strong enough to suspend heavier sediments. Despite the GvB flat exhibiting relatively fine sediments, there will likely have been a sandy fraction which sank to the bottom of the calibration tank. This would have skewed the calibration curves, leading to incorrect concentration estimates.
Despite this, the overall trend of the SSC signal will be accurate, which was most important for this study. The magnitude will however need to be considered carefully. There is a high change that this does not reflect the actual concentrations which were present on the tidal flat.

The third and final bad aspect was observed when comparing 2D wave u_{rms} to peak orbital velocity U_w. The first was derived from ADV velocity bursts whilst the latter was based upon wave spectral parameters from pressure measurements. Figure 5.6 illustrates the relation between the two velocities across each measurement frame.
The ratio is close to 1 for small water depths with larger waves and velocities. However it decreases significantly at high tide, making the two variables hard to use interchangeably. The study by Wiberg and Sherwood (2008) illustrates the effect of pressure versus velocity measurements in great depth, which was not considered during this study.

The Ugly
Worse than the bad aspects, the following points describe ugly attributes of the field campaign. These greatly hindered the research potential, or damaged the accuracy of obtained results.

The most obvious ugly aspect of the field campaign has been mentioned numerous times, namely the lack of significant south-west winds. Figure 4.1 illustrates how rare south-west winds were during the month-long campaign. Although the most energetic event was selected, the winds were still unable to generate large waves across the tidal flat.

The second ugly aspect was caused by spectral leakage in the long wave frequency range. Waves longer than the set burst period $T_{burst} = 20min$ created non-physical peaks in the first bins. Despite excluding the first frequency bin from the analysis, variance was still found to spike in the second. Overall this effect damaged the physical representation of the long wave spectral parameters. Without these it was not possible to certainly state the observed periods of the long wave field. This made it tricky to classify them.

Finally, the last ugly aspect is marine growth. As discussed by Downing (2006), marine growth on STMS sensors can greatly disturb SSC signals. Able to take place in less than a month, the obstruction by barnacles induces erroneous measurements. Some small barnacles were identified on the STMS sensors during retrieval, therefore this may have had an adverse affect on the signal quality.

6.3. Zooming Out - Current Morphology and Future Measurements

This section places the obtained results in the broader context of the Western Scheldt estuary. The relations found between waves, velocities, and SSC are discussed in light of the current morphology of the Galgeput van Bath (GvB) tidal flat. Despite the limited dataset, an effort is made to interpret how waves are influencing the GvB tidal flat and whether they play a significant role compared to tidal and sedimentary processes. Finally, an outlook is provided highlighting potential datasets and future measurement locations that could improve the understanding of wave-driven morphodynamics on muddy tidal flats in the Western Scheldt.

6.3.1. The Role of Wave-Driven Morphodynamics on the GvB Tidal Flat

Most tidal flats in the Western Scheldt are tidally dominated. They are characterized by convex-up bed profiles that have gradually built up over the past decades (de Vet, 2020; Maan et al., 2018). The continuous accretion has led to the formation of relatively steep lower edges, which act as transition zones to the subtidal channels. Convex-up profiles and long-term accretionary trends are both indicators of tidal dominance according to Friedrichs (2011).

The morphology of the GvB tidal flat follows this pattern. Its overall profile is convex-up, with a relatively flat upper section that transitions into a steeper slope near the seaward boundary. This configuration suggests that the upper flat is mainly tidally accretive, while the lower section experiences enhanced hydrodynamic forcing, likely due to increased wave exposure during high-water conditions.

The measured wave conditions during the observation period were relatively mild and likely insufficient to induce erosion. However, the long-term influence of waves cannot be ruled out. The mean wind rose for Vlissingen indicates that south-westerly winds are dominant, especially during the winter months. These conditions are known to generate higher local wave energy across the Western Scheldt, particularly during storm events. The calm wave climate observed in this dataset therefore likely represents a low-energy state of the system.
The effect of long waves is hard to determine based off of this measurement campaign alone. As no significant SSC response was identified at the time scale of long wave velocities, their impact on erosion cannot be attributed confidently.

6.3.2. Future Research and Fruitful Measurement Locations

The present measurements were conducted during relatively calm meteorological conditions, with low wind speeds that limited local wave generation. The resulting wave climate was therefore much less energetic than during the storm event reported by de Vet (2020), where winds of $u_{wind} = 20$ m/s produced significant wave heights up to $H_{m0} = 0.6$ m at the nearby Zuidgors tidal flat. Those conditions were associated with measurable bed erosion, demonstrating the potential of strong wind events to mobilize and suspend fine sediments.

Future research should aim to capture such energetic conditions. Here a spectral approach may give greater understanding of the energetic waves, and highlight the effect of any long waves in the spectrum. Long-term deployments covering multiple seasons would help distinguish between calm, accretive periods and storm-driven erosive phases.
Considering more exposed tidal flats, as well as those close to the busy navigation channel may benefit from a spectral approach. These may receive infra-gravity waves or frequent vessel waves that could contribute significantly to the tidal flat morphodynamics over time.

7

Conclusion

This study aimed to determine whether a spectral approach can provide a better understanding of wave and sediment dynamics on muddy tidal flats. Using 1 month of field measurements (pressure, 3D velocities and SSC) taken on the GvB tidal flat in the Western Scheldt, long ($f = [0.003 - 0.1]Hz$) and short ($f = [0.1 - 1.5]Hz$) waves were characterized by considering surface elevation and near bed velocities. Reviewing these in light of observed SSC measurements, it was possible to link wave spectral components to sediment suspension. The conclusions presented in this chapter answer the main research question and sub-questions. Finally the main limitations and recommendations are presented for future research.

Can a spectral approach provide a better interpretation of wave driven sediment dynamics on muddy tidal flats?

A spectral approach is in state of providing a better understanding of wave and sediment dynamics compared to a monochromatic approach. By considering distinct long and short frequency bands, it is possible to describe transformations and forcing which are unique to specific frequencies. By separating long and short frequency bands the analysis revealed that (1) short waves dominate elevation variance and therefore control most of the surface energy, while (2) long waves, although less energetic in elevation, contribute a large fraction of near bed velocity variance. The latter was attributed to the larger attenuation of short wave rather than long wave orbital velocities at larger water depths.
By observing peaks in long wave elevation variance that were not matched by the short wave domain, their generation was identified to be outside of the local wave field. This information aids the understanding of the wave climate on tidal flats, highlighting that infra-gravity waves are perhaps less prevalent. Instead vessel waves or seiches may be more common.
Spectral decomposition also allowed identification of an energetic long wave event that effectively drove larger wave orbital velocities at the bed. Considering the SSC time series alongside the observed long wave velocities, there appeared to be matching oscillations which could suggest the suspension of sediments at long wave frequencies. This would likely have been misinterpreted or overlooked in a monochromatic analysis.

How do wave transformations take place across spectral components in the wave field on a muddy tidal flat under varying water levels, tidal currents and wind forcing?

Highly linear ($N_{Ursell,short} \approx 1$) short waves were identified considering a frequency band of $f = [0.1 - 1.5]Hz$. In contrast to Le Hir et al. (2000) and de Vet (2020), measured short wave heights showed little dependence on water depth across the three frames. The incoming short wave heights were minor $H_{m0,short} < 0.3m$ and were thus barely limited by the commonly used depth-limited attenuation factor.
Instead, short wave development was seen to be more sensitive to fetch and shoaling. Root-mean-squared short wave heights increased slightly shoreward, consistent with greater fetch and shoaling. The largest $H_{rms,short}$ were consistently observed at the most south-west wind directions, being most perpendicular to the tidal flat. This highlighted the strong influence of wind direction on available fetch.

Short wave mean zero down-crossing period $T_{m02,short}$ increased with depth, which origin remains undetermined. Larger fetch is speculated to be caused by the applied attenuation factor $S_w(f)$. Improper tapering of high frequencies is suspected to induce a depth dependent modulation of mean period. This requires further investigation.
Non-linear ($N_{Ursell,long} > 26$) long waves were consistently identified in the wave field, and classified considering $f = [0.003 - 0.1]Hz$. These generally explained a small portion of the total surface elevation variance ($m_{0,long}/m_0 \leq 10\%$). However while short waves dissipated more quickly across the flat, long waves reached the upper flat with more energy.

How do the different spectral components present in the wave field contribute to the near bed orbital velocities and bed shear stresses, and how do these suspend sediments?

Short waves reaching the bed at low water depths produced the largest near bed orbital velocities and highest wave driven bed shear stresses. Meanwhile long waves were effective at explaining velocity variance at larger depths ($m_{0,long}/m_0 \approx 60\%$), yet rarely produced large bed orbital velocities.
Observed SSC increased at low depths, initially indicating a forcing by wave driven bed shear stresses. However when comparing SSC to τ_w, poor correlation was observed. At the low and middle frames, SSC fluctuates in a wide range for small shear stresses. Meanwhile SSC is near zero for all bed shear stresses at the high frame. This is indicative of a turbid fringe, which travels across the flat within shallow water across frames FL and FM. The consistent lack of SSC response at FH contradicts the observed trend in τ_w which was often largest at FH.
Although long wave orbital velocities were generally small, there did appear to be some SSC response at the long wave timescales when these dominated the velocity field. This however resulted in a mean SSC of $\langle SSC \rangle = 0.11g/L$, that was obscured during the presence of a turbid fringe $\langle SSC \rangle = 0.41g/L$.
Generally the bed appeared strong enough to withstand the observed shear stresses. Instead waves exerted the largest influence on SSC through resuspension within the turbid fringe as it travelled between the low and middle measurement frames.

Core Limitations and Future Recommendations
Two main limitations obstructed the research objective. Firstly the lack of significant south-west winds limited the range of observed wave conditions. Secondly the burst length (20 min) produced spectral leakage that damaged long wave parametrisation. Under more energetic conditions, it would be fruitful to assess whether long wave peaks consistently drive large enough velocities to modulate SSC at the timescale of the long waves.
Sufficient measurement period is critical to obtain accurate results of the long wave field. Furthermore the use of three measurement frames can also be recommended, as it provides better spatial context regarding phenomena such as turbid fringes which would not be detected as well when using only a low and high measurement frame.
The value of a spectral approach is strongly dependent on the measured wave climate. In the case of tidal flats, local wind driven waves dominate the spectrum which makes a monochromatic approach satisfactory in many situations. However, it does fail to capture the influence of long waves, which can be prevalent in the form of seiches and vessel waves. Considering the stakeholders and bathymetry of the Western Scheldt, these could both receive more attention.
Finally, exposed tidal flats may experience swell and infra-gravity waves like many coastlines. In which case a spectral approach would be of great value to understanding cross-shore variations in wave and sediment dynamics.

References

Amos, C. L. (1995). Chapter 10 siliciclastic tidal flats. In G. Perillo (Ed.), *Geomorphology and sedimentology of estuaries* (pp. 273–306, Vol. 53). Elsevier. https://doi.org/10.1016/S0070-4571(05)80030-5

Bosboom, J., & Stive, M. (2023, January 1). *Coastal Dynamics*. TU Delft OPEN Publishing. https://doi.org/10.5074/T.2021.001

Bowen, A. J. (1980). *Simple Models of Nearshore Sedimentation, Beach Profiles and Longshore Bars* (No. 80–10). https://doi.org/10.4095/102213

Callaghan, D., Bouma, T., Klaassen, P., Van Der Wal, D., Stive, M., & Herman, P. (2010). Hydrodynamic forcing on salt-marsh development: Distinguishing the relative importance of waves and tidal flows. *Estuarine, Coastal and Shelf Science*, *89*(1), 73–88. https://doi.org/10.1016/j.ecss.2010.05.013

Colina Alonso, A. (2024). *Sand-Mud Morphodynamics*. https://doi.org/10.4233/UUID:8BD55CE1-ADC7-486D-9BFA-7AA7B929BBE3

de Bakker, A. T. M., Brinkkemper, J. A., Steen, F., Tissier, M. F. S., & Ruessink, B. G. (2016). Cross□shore sand transport by infragravity waves as a function of beach steepness. *Journal of Geophysical Research*.

de Bakker, A. T. M., Tissier, M. F. S., & Ruessink, B. G. (2015). Beach steepness effects on nonlinear infragravity□wave interactions: A numerical study. *Journal of Geophysical Research: Oceans*, *121*(1), 554–570. https://doi.org/10.1002/2015JC011268

de Vet, P. (2020). *Intertidal Flats in Engineered Estuaries: On the Hydrodynamics, Morphodynamics, and Implications for Ecology and System Management*. https://doi.org/10.4233/UUID:2B392951-3781-4AED-B093-547C70CC581D

Downing, J. (2006). Twenty-five years with OBS sensors: The good, the bad, and the ugly. *Continental Shelf Research*, *26*(17–18), 2299–2318. https://doi.org/10.1016/j.csr.2006.07.018

Elias, E. P. L., Van Der Spek, A. J. F., Wang, Z. B., Cleveringa, J., Jeuken, C. J. L., Taal, M., & Van Der Werf, J. J. (2023). Large-scale morphological changes and sediment budget of the Western Scheldt estuary 1955–2020: The impact of large-scale sediment management. *Netherlands Journal of Geosciences*, *102*, e12. https://doi.org/10.1017/njg.2023.11

Feng, J., Grandjean, T. J., Van De Koppel, J., & Van Der Wal, D. (2025). A spatiotemporal framework to assess the bio-geomorphic interplay of saltmarsh vegetation and tidal emergence (Western Scheldt estuary). *International Journal of Applied Earth Observation and Geoinformation*, *136*, 104337. https://doi.org/10.1016/j.jag.2024.104337

Friedrichs, C. (2011). Tidal Flat Morphodynamics. In *Treatise on Estuarine and Coastal Science* (pp. 137–170). Elsevier. https://doi.org/10.1016/B978-0-12-374711-2.00307-7

Gatto, V. M., Van Prooijen, B. C., & Wang, Z. B. (2017). Net sediment transport in tidal basins: Quantifying the tidal barotropic mechanisms in a unified framework. *Ocean Dynamics*, *67*(11), 1385–1406. https://doi.org/10.1007/s10236-017-1099-3

Green, M. O. (2011). Very small waves and associated sediment resuspension on an estuarine intertidal flat. *Estuarine, Coastal and Shelf Science*, *93*(4), 449–459. https://doi.org/10.1016/j.ecss.2011.05.021

Green, M. O., Black, K. P., & Amos, C. L. (1997). Control of estuarine sediment dynamics by interactions between currents and waves at several scales. *Marine Geology*, *144*(1–3), 97–116. https://doi.org/10.1016/S0025-3227(97)00065-0

Green, M. O., & Coco, G. (2014). Review of wave-driven sediment resuspension and transport in estuaries: WAVE-DRIVEN SEDIMENT TRANSPORT. *Reviews of Geophysics*, *52*(1), 77–117. https://doi.org/10.1002/2013RG000437

Guillou, N., & Chapalain, G. (2024). Characterizing Seiches Oscillations in a Macro-Tidal Estuary. *Coasts*, *4*(1), 108–126. https://doi.org/10.3390/coasts4010007

Hanssen, J. L. J., Van Prooijen, B. C., & Van Maren, D. S. (2024). The shape of fringing tidal flats in engineered estuaries. *Frontiers in Marine Science*, *11*, 1354716. https://doi.org/10.3389/fmars.2024.1354716

Herman, P. M., Middelburg, J. J., & Heip, C. H. (2001). Benthic community structure and sediment processes on an intertidal flat: Results from the ECOFLAT project. *Continental Shelf Research*, *21*(18–19), 2055–2071. https://doi.org/10.1016/S0278-4343(01)00042-5

Holthuijsen, L. H. (2007). *Waves in Oceanic and Coastal Waters*. Cambridge University Press.

Le Hir, P., Roberts, W., Cazaillet, O., Christie, M., Bassoullet, P., & Bacher, C. (2000). Characterization of intertidal flat hydrodynamics. *Continental Shelf Research*, *20*(12–13), 1433–1459.

Leuven, J. R. F. W., Verhoeve, S. L., Van Dijk, W. M., Selaković, S., & Kleinhans, M. G. (2018). Empirical Assessment Tool for Bathymetry, Flow Velocity and Salinity in Estuaries Based on Tidal Amplitude and Remotely-Sensed Imagery. *Remote Sensing*, *10*(12), 1915. https://doi.org/10.3390/rs10121915

Maan, D. C., Van Prooijen, B. C., Zhu, Q., & Wang, Z. B. (2018). Morphodynamic Feedback Loops Control Stable Fringing Flats. *Journal of Geophysical Research: Earth Surface*, *123*(11), 2993–3012. https://doi.org/10.1029/2018JF004659

Mu, T., & Wilcove, D. S. (2020). Upper tidal flats are disproportionately important for the conservation of migratory shorebirds. *Proceedings of the Royal Society B: Biological Sciences*, *287*(1928), 20200278. https://doi.org/10.1098/rspb.2020.0278

Nortek AS. (2018). *Comprehensive manual: Velocimeters* [N3015-030]. https://www.nortekgroup.com/assets/software/N3015-030-Comprehensive-Manual-Velocimeters_1118.pdf

Rapaglia, J., Zaggia, L., Parnell, K., Lorenzetti, G., & Vafeidis, A. T. (2015). Ship-wake induced sediment remobilization: Effects and proposed management strategies for the Venice Lagoon. *Ocean & Coastal Management*, *110*, 1–11. https://doi.org/10.1016/j.ocecoaman.2015.03.002

Rijkswaterstaat. (2025). Waterinfo [Accessed: 2025-10-04]. https://waterinfo.rws.nl/

Schoellhamer, D. H. (1996). Anthropogenic Sediment Resuspension Mechanisms in a Shallow Microtidal Estuary. *Estuarine, Coastal and Shelf Science*, *43*(5), 533–548. https://doi.org/10.1006/ecss.1996.0086

Seapoint Sensors, Inc. (2013, July). *Seapoint turbidity meter: User manual* [stm_um]. https://www.seapoint.com/pdf/stm_um.pdf

Seo, J. Y., Choi, B.-J., Choi, S. M., Ryu, J., & Ha, H. K. (2024). Contribution of coastal seiches to sediment transport in a microtidal semi-enclosed bay. *Frontiers in Marine Science*, *11*, 1392435. https://doi.org/10.3389/fmars.2024.1392435

Soulsby, R. (1997). *Dynamics of marine sands*. Emerald Publishing Limited. https://books.google.nl/books?id=4N1M5lWIyAoC

Soulsby, R., Hamm, L., Klopman, G., Myrhaug, D., Simons, R., & Thomas, G. (1993). Wave-current interaction within and outside the bottom boundary layer. *Coastal Engineering*, *21*(1–3), 41–69. https://doi.org/10.1016/0378-3839(93)90045-A

Swinkels, C. M., Jeuken, C. M. C. J. L., Wang, Z. B., & Nicholls, R. J. (2009). Presence of Connecting Channels in the Western Scheldt Estuary. *Journal of Coastal Research*, *253*, 627–640. https://doi.org/10.2112/06-0719.1

Tas, S. A. J., Maren, D. S. V., & Reniers, A. J. H. M. (2020). Observations of Cross-Shore Chenier Dynamics in Demak, Indonesia. *Journal of Marine Science and Engineering*, *8*(12), 972. https://doi.org/10.3390/jmse8120972

Van Der Lugt, M. A., Bosma, J. W., De Schipper, M. A., Price, T. D., Van Maarseveen, M. C. G., Van Der Gaag, P., Ruessink, G., Reniers, A. J. H. M., & Aarninkhof, S. G. J. (2024). Measurements of morphodynamics of a sheltered beach along the Dutch Wadden Sea. *Earth System Science Data*, *16*(2), 903–918. https://doi.org/10.5194/essd-16-903-2024

Van Dijk, W. M., Hiatt, M. R., Van Der Werf, J. J., & Kleinhans, M. G. (2019). Effects of Shoal Margin Collapses on the Morphodynamics of a Sandy Estuary. *Journal of Geophysical Research: Earth Surface*, *124*(1), 195–215. https://doi.org/10.1029/2018JF004763

van Ledden, M. (2003). Sand-mud segregation in estuaries and tidal basins.

van Rijn, L. C. (1993). *Principles of sediment transport in rivers, estuaries and coastal seas* (vi). Aqua Publications.

Wang, C., & Temmerman, S. (2013). Does biogeomorphic feedback lead to abrupt shifts between alternative landscape states?: An empirical study on intertidal flats and marshes. *Journal of Geophysical Research: Earth Surface*, *118*(1), 229–240. https://doi.org/10.1029/2012JF002474

Wiberg, P. L., & Sherwood, C. R. (2008). Calculating wave-generated bottom orbital velocities from surface-wave parameters. *Computers & Geosciences*, *34*(10), 1243–1262. https://doi.org/10.1016/j.cageo.2008.02.010

Zhu, Q., Van Prooijen, B., Maan, D., Wang, Z., Yao, P., Daggers, T., & Yang, S. (2019). The heterogeneity of mudflat erodibility. *Geomorphology*, *345*, 106834. https://doi.org/10.1016/j.geomorph.2019.106834

Zhu, Q., Van Prooijen, B., Wang, Z., Ma, Y., & Yang, S. (2016). Bed shear stress estimation on an open intertidal flat using in situ measurements. *Estuarine, Coastal and Shelf Science*, *182*, 190–201. https://doi.org/10.1016/j.ecss.2016.08.028

Zhu, S., Wei, W., Zhu, Q., Wan, K., Xing, F., Yan, W., Gao, J., & Wang, Y. P. (2024). Wave attenuation and transformation across a highly turbid muddy tidal flat-salt marsh system. *Applied Ocean Research*, *147*, 103980. https://doi.org/10.1016/j.apor.2024.103980

A

Additional Results

Appendix A presents additional results that are complementary to chapters 4 and 5.

Sections A.1 and A.2 present observed wave transformations at measurement frames FM and FH under influence of changing water depths, tidal current as well as wind climate. The figures follow the same structure as shown in figure 4.10, showing the relation between $H_{m0,short}$ and $T_{m02,short}$ over depth for flood, slack and ebb tides. Furthermore the mean horizontal flow and wind conditions are given. These provide context as to the effect of tidal currents and wind conditions on wave dynamics across the tidal flat. Generally both the FM and FH measurement frames captured a similar response as the low location (FL). However there was a slight increase in wave heights across all depths for more onshore measurement frames.

A.1. Wave Transformations at Frame FM

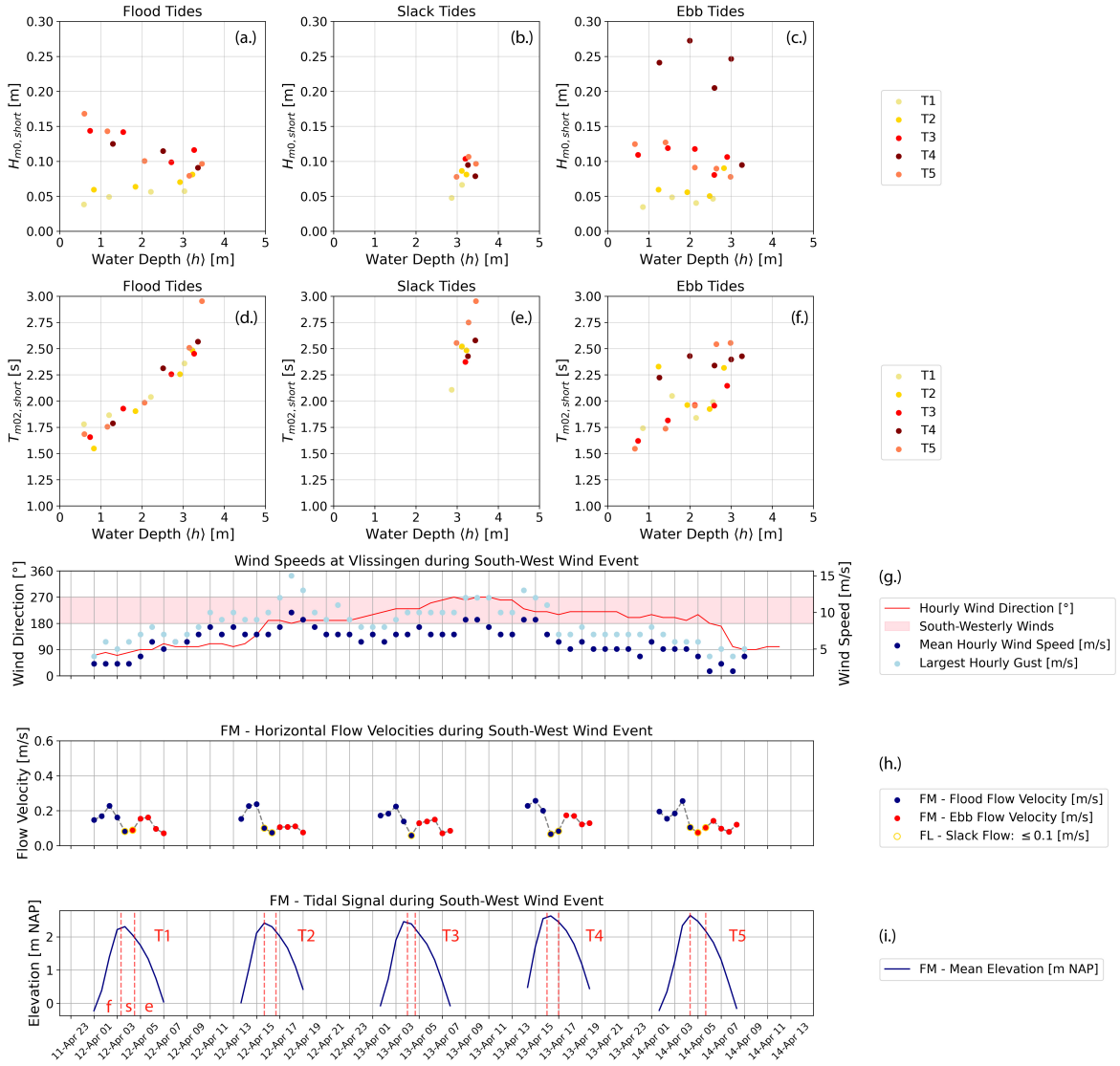

Figure A.1: Significant wave heights and mean spectral periods per water depth during flood, slack and ebb tides at frame FM. Panel (a, b, c): Significant wave height H_{m0} [m] over water depth d [m] for five tides. Panel (d, e, f): Mean spectral period T_{m02} [s] over water depth d [m] for five tides. Panel (g.): Wind speeds and direction from KNMI weather station in Vlissingen during SW wind event. Panel (h.): Horizontal flow velocities (2D burst u_{rms}) $[m/s]$ considering flood and ebb currents. Panel (i.): Mean elevation [m NAP] for 5 tides during south-west wind event

A.2. Wave Transformations at Frame FH

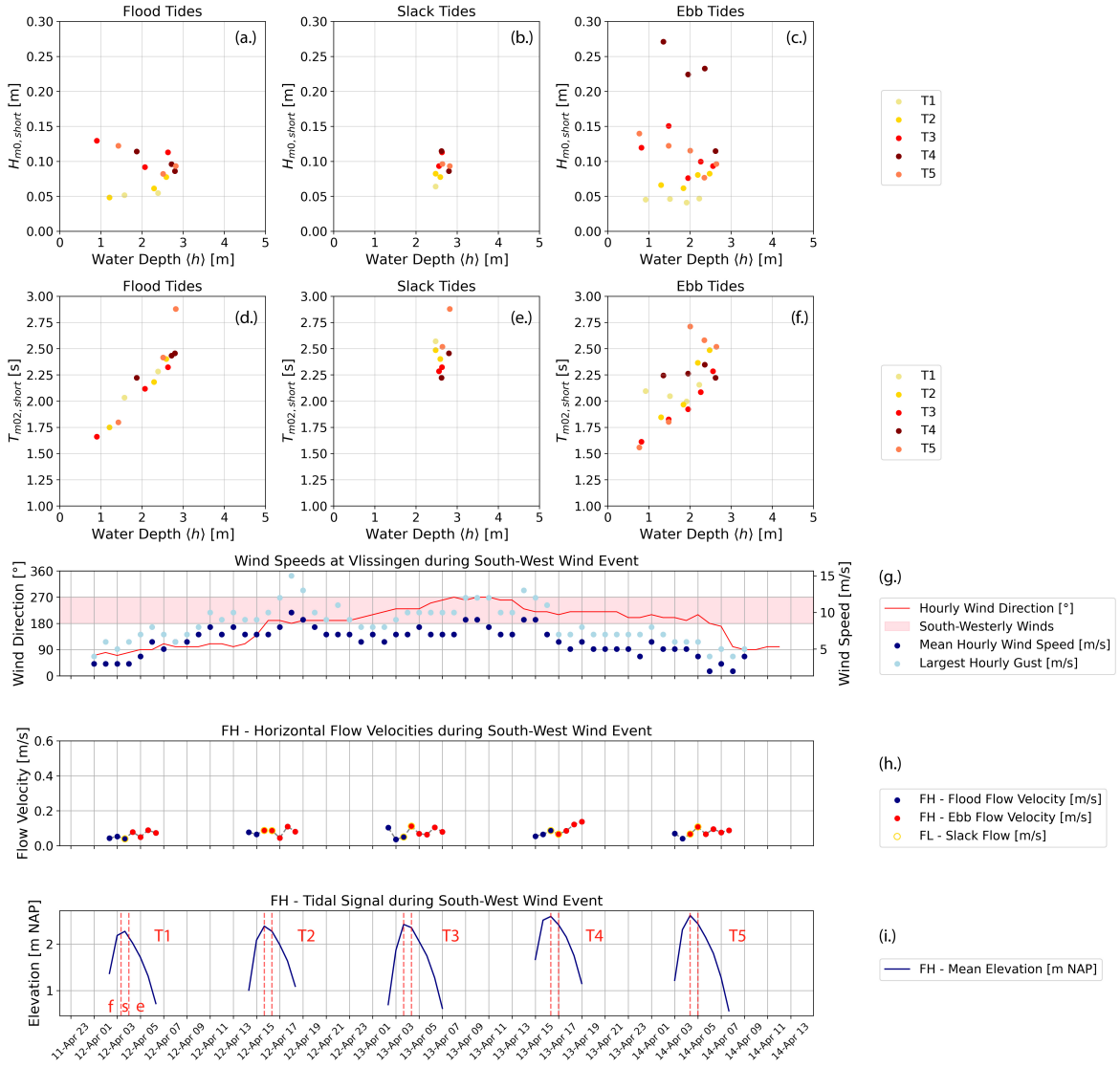

Figure A.2: Significant wave heights and mean spectral periods per water depth during flood, slack and ebb tides at frame FH. Panel (a, b, c): Significant wave height H_{m0} [m] over water depth d [m] for five tides. Panel (d, e, f): Mean spectral period T_{m02} [s] over water depth d [m] for five tides. Panel (g.): Wind speeds and direction from KNMI weather station in Vlissingen during SW wind event. Panel (h.): Horizontal flow velocities (2D burst u_{rms}) $[m/s]$ considering flood and ebb currents. Panel (i.): Mean elevation [m NAP] for 5 tides during south-west wind event